Technische Universität München
Fakultät für Physik

Master's Thesis

Study of the Tensor Structure of the Higgs Boson Coupling to Gluons in the $pp \rightarrow H \rightarrow ZZ^* \rightarrow 4\ell$ Process with the ATLAS Experiment

Maxim Sinner

13. September 2018

Max-Planck-Institut für Physik
(Werner-Heisenberg-Institut)

Examiner	PD Dr. O. Kortner
Co-Examiner	Prof. Dr. L. Oberauer
Supervisor	Dr. S. Kortner

Abstract

The tensor structure of the effective coupling between the Higgs boson and gluons was studied in the $pp \rightarrow H \rightarrow ZZ^* \rightarrow 4\ell$ process with dedicated Monte Carlo simulations. In the gluon–gluon fusion production mode of the Higgs boson, angular correlations of final state jets in the process $gg \rightarrow H + 2j$ have been used to probe small $\mathcal{CP}$-odd admixtures to the Higgs–gluon coupling. The sensitivity to the sign of the anomalous coupling parameter was studied using simulated proton–proton collisions data in the ATLAS detector at the LHC for integrated luminosities of 36.1 fb^{-1} and 120 fb^{-1} at a centre-of-mass energy of 13 TeV and for integrated luminosities of 300 fb^{-1} and 3000 fb^{-1} at a centre-of-mass energy of 14 TeV. As opposed to the production rate information, the shape of the differential distribution of the angular distance between the two final state jets allows for the exclusion of the wrong-sign hypothesis in the currently allowed parameter range with almost 1σ significance, with more than 1σ and with more than 4σ for integrated luminosities of 120 fb^{-1}, 300 fb^{-1} and 3000 fb^{-1}, respectively.

Contents

1 Introduction

One of the most important achievements of high-energy particle physics is the theory describing the fundamental interaction of the elementary particles in a highly elegant and successful manner. The *Standard Model* of particle physics [1–4], which was introduced in the latter half of the 20^{th} century and finalised in the 1970s, was not only able to predict the existence of many, eventually experimentally detected elementary particles, but also remains unrivalled in the level of precision to which it has been successfully tested. With the announcement of the independent discovery of the *Higgs boson* in July 2012 by ATLAS[1] and CMS[2] Collaborations [5, 6] at the *Large Hadron Collider* (LHC) [7] at CERN[3] a milestone was reached, as this particle completes the list of observed particles, which are predicted by the Standard Model.

After subsequent years of property measurements of the newly discovered Higgs boson—an excitation of the so-called *Higgs field*, which provides elementary particles with their respective masses via the *Higgs mechanism* [8–13]—all predicted Higgs boson production and decay modes have been observed, underlining the power and success of the LHC and the research programme at CERN. At the same time, many unsolved physics questions, e. g. the baryon asymmetry in the universe or the existence of Dark Matter, hint at the Standard Model not being the complete theory, but only a low-energy approximation of a greater, more general theory. Hence, searches for physics beyond the Standard Model looking for signs of irregularities between Standard Model predictions and experimental observations are under way, exploring the properties of the Higgs boson. Many theories assume an extended Higgs sector, leading to single or multiple Higgs bosons with properties deviating from Standard Model predictions, e. g. the behaviour under charge conjugation and parity transformation $\mathcal{CP}$. While the Standard Model Higgs boson is predicted to be a $\mathcal{CP}$-even scalar particle and current measurements strongly disfavour different spin and $\mathcal{CP}$-configurations [14, 15], the possibility of a Higgs boson state that is a superposition of $\mathcal{CP}$-even and $\mathcal{CP}$-odd states remains a promising option [16]. An admixture of a $\mathcal{CP}$-odd part to the $\mathcal{CP}$-even state of

[1] A Toroidal LHC ApparatuS
[2] Compact Muon Solenoid
[3] Conseil Européen pour la Recherche Nucléaire

the Higgs boson would be a source for $\mathcal{CP}$-violation. Such admixtures can be measured by looking for anomalous contributions in the Higgs boson couplings.
The study presented in this thesis examines the coupling between the Higgs boson and a pair of gluons in events from the gluon–gluon fusion process, the most dominant Higgs boson production mode at the LHC. The sensitivity to anomalous $\mathcal{CP}$-odd contributions in the tensor structure of the Higgs boson coupling to gluons is studied in the $gg \to H$ process using data from dedicated Monte Carlo simulations with Higgs boson decays into a pair of Z bosons that subsequently each decay into a pair of electrons or muons. Due to a high signal-to-background ratio and a clear signature, this decay channel provides an excellent sensitivity to the Higgs boson signal. The $gg \to H$ interaction vertex is assumed to be point-like in an effective field theory approach using the Higgs characterisation model [17] and the infinite top quark mass limit.
Previous analyses of the tensor coupling structure of the Higgs boson to gluons [18] show a sensitivity to an absolute deviation from the Standard Model prediction, but are not able to distinguish the sign of the anomalous coupling parameter. In order to study the $\mathcal{CP}$-sensitivity, new sign-sensitive observables are considered in this work. An observable providing such discrimination capabilities is the azimuthal angle difference of final state jets in the $gg \to H + 2j$ production process. Shape information of the distribution of this observable is used to investigate the sensitivities reachable in different high-luminosity scenarios.

In Chapter 2 the LHC and particularly the ATLAS detector together with its sub-detectors are presented. In Chapter 3 a brief theory introduction to the Standard Model and Higgs boson physics at the LHC is given including current Higgs boson measurements. The $H \to ZZ^* \to 4\ell$ analysis channel is introduced in Chapter 4. Finally, in Chapter 5 the results of the sensitivity study are presented, considering centre-of-mass energies of 13 TeV and 14 TeV and integrated luminosities of 120 fb^{-1}, 300 fb^{-1} and 3000 fb^{-1} in accordance to the expected values for the LHC Run 2, Run 3 and HL-LHC project. Chapter 6 summarises and concludes the work of this thesis.

2

The ATLAS experiment at the LHC

Mankind's endeavour in deepening the understanding of nature and the way it works has involved breaking down matter to its fundamental building blocks for thousands of years. The progress to unimaginably small scales demands high-energy particle collisions. The LHC is a particle accelerator with the highest collision energy at the moment, enabling thousands of scientist all around the globe to do precision measurements and to search for new physics phenomena at the TeV energy scale.

2.1 The Large Hadron Collider

The LHC [7] is operated by the European Organisation for Nuclear Research (CERN) near Geneva and is a synchrotron particle accelerator situated about 100 m under the Franco-Swiss border. The two-ring-superconducting-hadron accelerator and collider is placed in a circular tunnel with a circumference of 26.7 km, which was the former host of the Large Electron Positron Collider (LEP). At highest performance proton beams collide with a centre-of-mass energy of $\sqrt{s} = 13$ TeV and an instantaneous luminosity of up to $\mathcal{L} = 2.06 \cdot 10^{34}\,\mathrm{cm}^{-2}\,\mathrm{s}^{-1}$ [19, 20].

Before being injected into the LHC, the proton beams undergo several pre-acceleration stages: The source of the protons are hydrogen atoms that are stripped off their electrons via an electric field. The protons are then accelerated up to an energy of 50 MeV in the Linear accelerator 2 (Linac 2). The second accelerator in the chain is the Proton Synchrotron Booster (PSB) from where the protons enter the Proton Synchrotron (PS) with an energy of 1.4 GeV. After reaching an energy of 25 GeV the protons are transferred to the Super Proton Synchrotron (SPS), which accelerates them up to 450 GeV, from where they eventually are injected into the two beam pipes of the LHC [21]. A schematic drawing of the LHC and the pre-accelerator system is shown in Figure 2.1.

The proton beams are held on track by 1232 superconducting dipole magnets, which operate

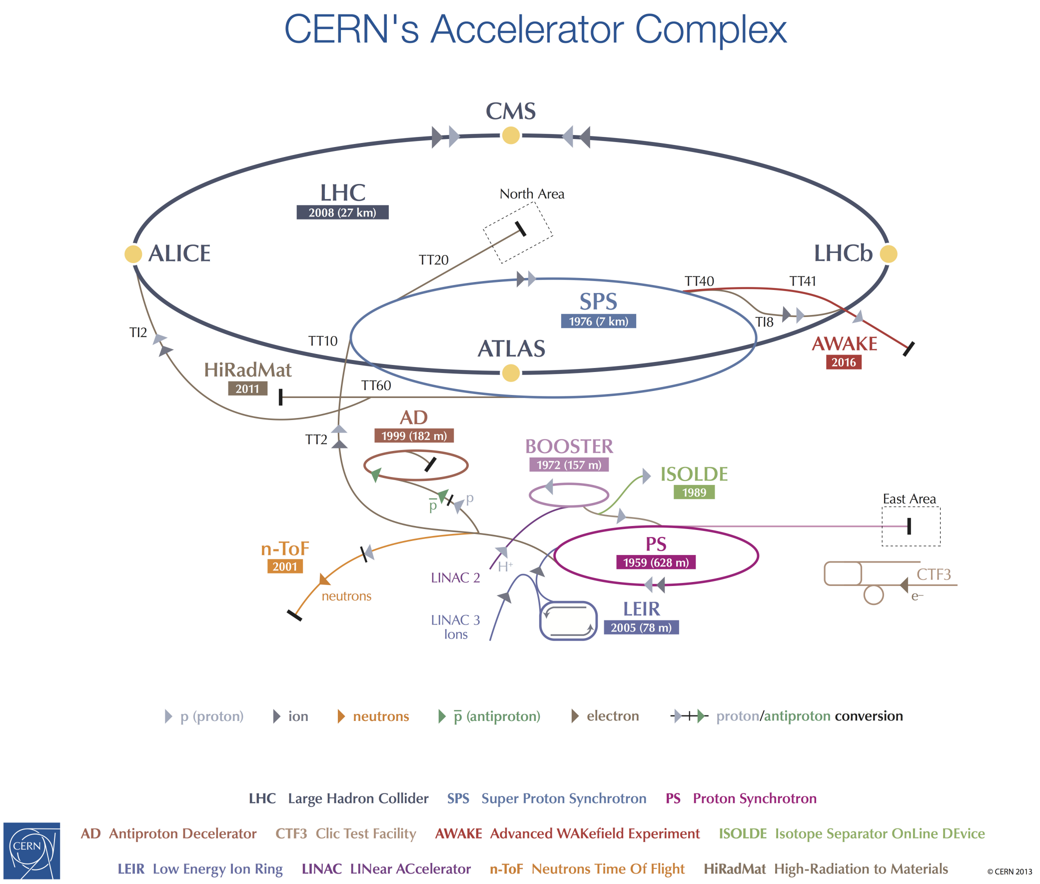

Figure 2.1: CERN's accelerator complex showing the LHC ring with the four main experiments ALICE, ATLAS, CMS and LHCb, the pre-accelerator system as well as smaller experiments and facilities [22].

at a temperature of 1.9 K and generate a magnetic field with a field strength of 8.33 T.
A proton beam is made up of a maximum of 2556 evenly spread bunches, each consisting of $1.15 \cdot 10^{11}$ protons [19]. The proton bunches collide in one of four interaction points, which are the locations of the four main experiments at the LHC.
Situated at opposite sides of the accelerator ring are the two 'general-purpose' experiments ATLAS and CMS. They cover a broad spectrum of particle physics research, including searches for Dark Matter, Supersymmetry, extra dimensions and precision tests of the Standard Model. However, the search for the Higgs boson was one of the main goals of both experiments. The announcement of the discovery by both collaborations on 4th July 2012 of a particle

consistent with the Higgs boson is one of the greatest successes of the LHC. To this day further investigations of the Higgs boson are being keenly performed.

Luminosity Often used to characterise the performance of a particle accelerator is the integrated luminosity $L = \int \mathrm{d}t\, \mathcal{L}$, which is the integral of the instantaneous luminosity with respect to time. The instantaneous luminosity $\mathcal{L}$ is the proportionality factor between the number of events of a given process occurring per second $\mathrm{d}N/\mathrm{d}t$ and the cross-section of the process σ:

$$\frac{\mathrm{d}N}{\mathrm{d}t} = \mathcal{L} \cdot \sigma \ .$$

Assuming two beams with equally Gaussian shaped bunch distributions, the instantaneous luminosity can be written as

$$\mathcal{L} = n_{\mathrm{b}} \frac{N^2 f_{\mathrm{ref}} \gamma_{\mathrm{r}}}{4\pi\beta^* \sqrt{\varepsilon_{\mathrm{x}}\varepsilon_{\mathrm{y}}}} S \ ,$$

where n_{b} is the number of bunch collisions per revolution, N the bunch intensity, i. e. the number of protons per bunch, f_{rev} the revolution frequency, γ_{r} the relativistic factor, β^* the value of the beta function at the interaction point, ε_{x} (ε_{y}) the normalised emittance in the horizontal (vertical) plane and S the geometric reduction factor due to the beam crossing angle at the interaction point [23].

Figure 2.2 shows the growth of the integrated luminosity of the year 2018 in comparison to past years. This year's average peak luminosity during the last steps of the intensity ramp-up was close to $2.1 \cdot 10^{34}\ \mathrm{cm}^{-2}\ \mathrm{s}^{-1}$, surpassing the record peak luminosity of 2017. The first operating phase of the LHC—referred to as Run 1—in the years 2011–2012 ended with a total integrated luminosity of almost $30\ \mathrm{fb}^{-1}$ [24], while for the end of Run 2 a total integrated luminosity of $120\ \mathrm{fb}^{-1}$ is expected. The planned integrated luminosity for the year 2018 is $60\ \mathrm{fb}^{-1}$ [25].

2.2 The ATLAS detector

The ATLAS experiment [27] is a general-purpose detector with full azimuthal coverage and nearly a 4π coverage in solid angle. It has a cylindrical shape around the proton beam axis. Its main goals are precision measurements of the Standard Model and the search for new physics phenomena beyond the Standard Model (BSM) in hadron collisions provided by the LHC.

The detector has a length of 44 m, a diameter of 25 m and weighs around 7000 tons. It consists of an inner part called the Inner Detector (ID), a calorimeter system around it and the Muon Spectrometer (MS). The magnet system consists of a superconducting solenoid generating a 2 T magnetic field in the ID and three large superconducting toroid magnets in the MS. Figure 2.3 shows a cutaway view of the detector and its main components.

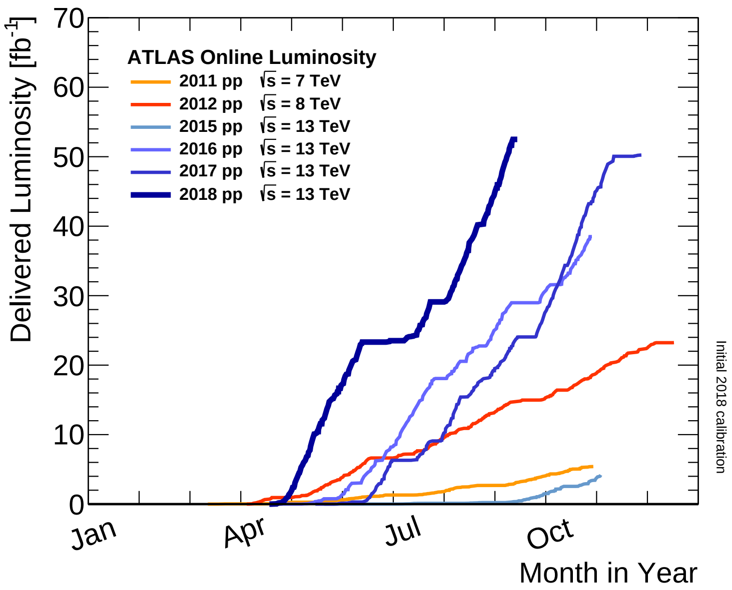

Figure 2.2: Integrated luminosity for the years 2011–2012 ($\sqrt{s} = 7$ TeV and $\sqrt{s} = 8$ TeV, respectively) and 2015–2018 ($\sqrt{s} = 13$ TeV) versus day delivered to ATLAS during stable beams and for high-energy proton–proton collisions [26].

ATLAS uses a right-handed coordinate system with its origin in the interaction point. As depicted in Figure 2.4(a), the z-axis is aligned tangentially to the LHC ring while the y-axis points vertically upwards and the x-axis points to the centre of the ring. Figure 2.4(b) shows the azimuthal angle ϕ defined in the transverse x-y-plane with respect to the positive x-axis and the polar angle θ is measured from the positive z-axis.

A commonly used variable that describes the kinematic condition of a particle is the rapidity y, which is defined as

$$y = \frac{1}{2} \ln \left(\frac{E + p_z}{E - p_z} \right),$$

where E is the energy of the particle and p_z the z-component of its momentum. The rapidity difference of two particles is invariant with respect to Lorentz boosts along the z-axis. A more convenient but equally useful quantity is the pseudo-rapidity η, which only uses the angle θ of a detected particle relative to the beam axis:

$$\eta = -\ln \left(\tan \left(\frac{\theta}{2} \right) \right).$$

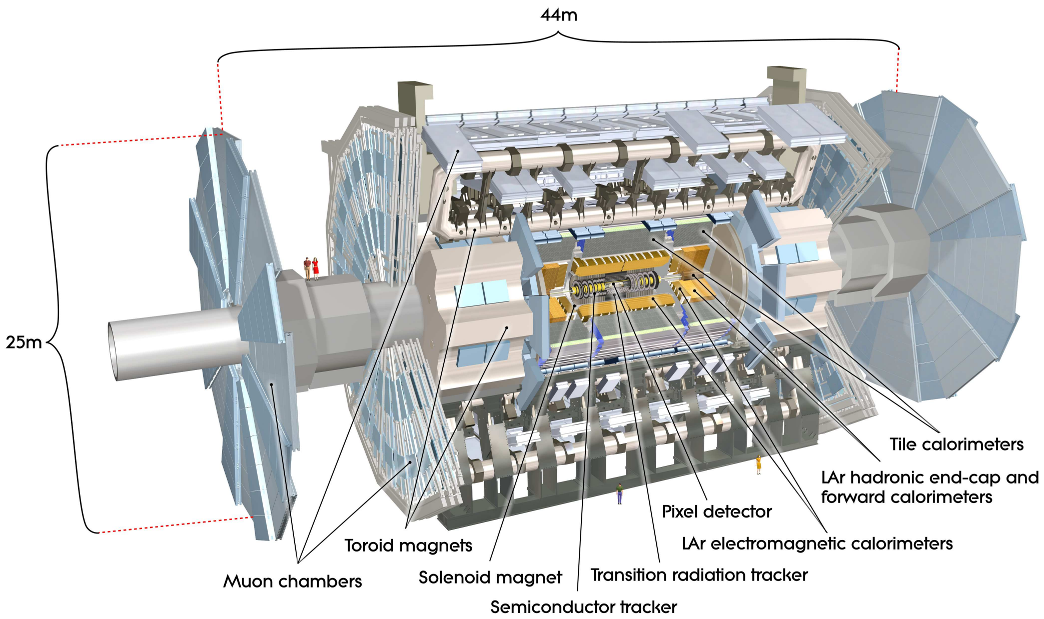

Figure 2.3: A cutaway view of the ATLAS detector showing its size and the main components such as the Inner Detector, the calorimeter system, the Muon Spectrometer and the solenoid and toroidal magnets [28].

For large particle momenta, i. e. particles moving with the speed of light or being nearly massless, $|\vec{p}| \approx E$ and the rapidity coincides with the pseudo-rapidity $y \approx \eta$ [29]. The following sections give a brief overview of the main parts of the ATLAS detector and their participation in the detection of particles. More details can be found in reference [27].

2.2.1 The Inner Detector

Charged particles created in a proton–proton collision are detected by the ID, whose main tasks are precise momentum measurements, pattern recognition and the reconstructions of the interaction point and decay vertices of secondary particles for pseudo-rapidities up to $|\eta| = 2.5$. It also performs an electron identification within the pseudo-rapidity range $|\eta| < 2.0$ and energies between 0.5 GeV and 150 GeV. The ID is enclosed by thin solenoid magnets, which generate a magnetic field with a field strength of 2 T, bending the trajectories, so-called tracks, of charged particles. A cutaway view of the ID is shown in Figure 2.5.

From the beam pipe outwards, the decay products of particles created at proton–proton collisions traverse three independent sub-detectors, beginning with the Pixel Tracker detec-

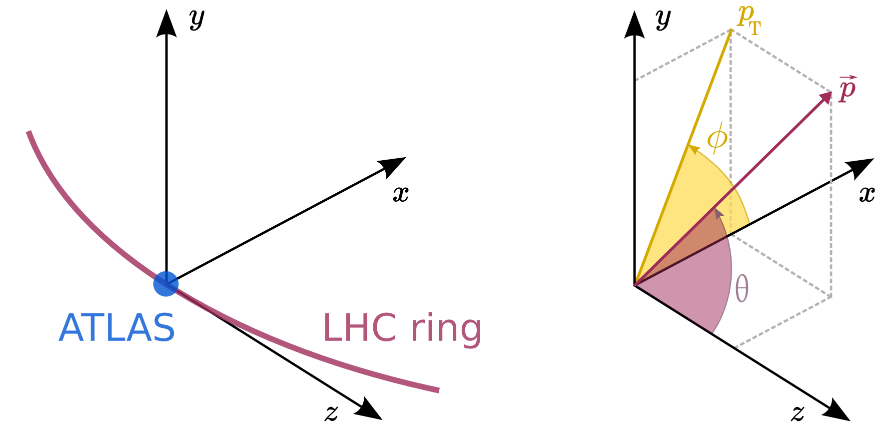

(a) (b)

Figure 2.4: In (a) the right-handed coordinate system used by the ATLAS experiment with the z-axis being tangential to the circular beam track, the y-axis pointing vertically upwards and the x-axis pointing to the centre of the beam ring and in (b) the common usage of polar coordinates with respect to a particles momentum $\vec{p}$ is shown.

tor. Then they pass the Semiconductor Tracker (SCT) and eventually reach the Transition Radiation Tracker (TRT).

Figure 2.6 shows a generic track of a charged particle traversing the ID, beginning with traversing three layers of concentric pixel sensors in the barrel region 50.5, 88.5 and 122.5 mm around the beam axis. Not depicted are the end-cap regions, where also three disks of pixel sensors are placed perpendicular to the beam axis on each side of the ID. The Pixel Tracker consists of 1744 pixel sensors, each 250 µm thick and equipped with 46 080 read-out channels, making precise primary and secondary vertex measurements possible. The intrinsic accuracies are 10 µm in the transverse plane and 115 µm in the longitudinal direction.

Challenges arising from increasing luminosities provided by the LHC motivated the installation of a fourth pixel detector layer during the 2013–2014 shut-down of the LHC. The Insertable B-Layer (IBL) is now the layer closest to the beam axis and improves the track and vertex reconstruction performance of the ID [31].

The next sub-detector is the SCT. Its layout is designed to guarantee at least four space-point measurements for a charged particle traversing the SCT: Four layers of silicon strip detector modules are arranged in the barrel region and nine disks are placed at each end-cap. 15 912 sensors make up the SCT, each sensor consisting of 768 active strips with a length of 12 cm and a thickness of 285 ± 15 µm. The resolutions are 17 µm in the transverse plane and 580 µm in the z-direction.

The TRT has straw drift tubes aligned parallel to the beam axis as detector elements. The tubes have a diameter of 4 mm, a length of 144 cm in the barrel region and 37 cm in the end-cap

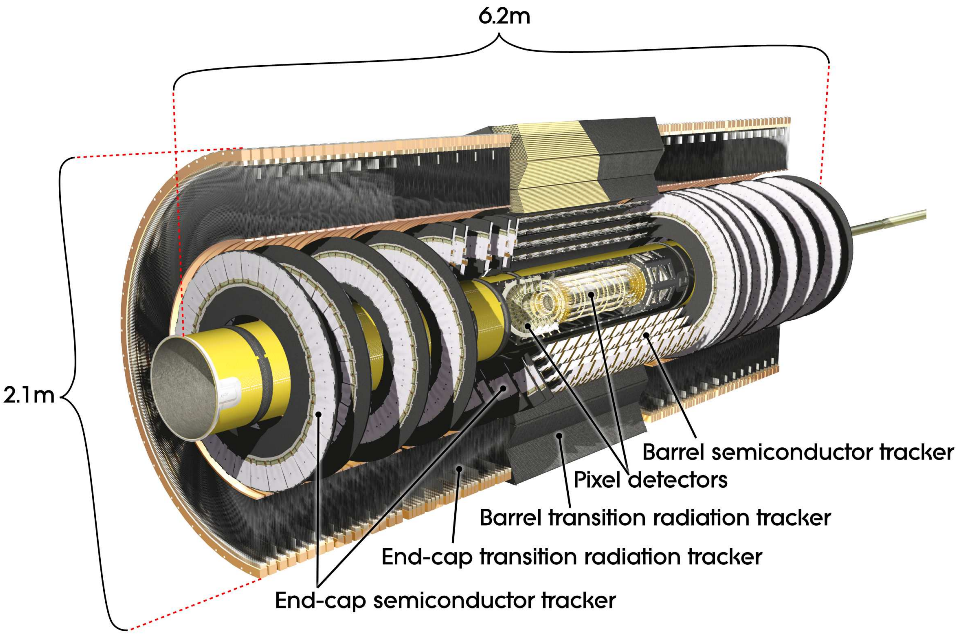

Figure 2.5: A cutaway view of the ATLAS Inner Detector showing its size and components, being the Pixel Tracker, the Semiconductor Tracker and Transition Radiation Tracker in both, barrel and end-cap regions [30].

regions and are filled with a Xe (70 %), CO_2 (27 %), O_2 (3 %) gas mixture. The straws are interleaved with fibres, serving as a transition radiation material. A particle track results on average in 36 hits, what allows for a continuous tracking and enhances pattern recognition, moment resolution and electron identification. The intrinsic measurement accuracy of the TRT is 130 μm per single straw.

2.2.2 The calorimeter system

The calorimeters of the ATLAS detector consist of an electromagnetic calorimeter system (ECal) and a hadronic calorimeter system (HCal). All calorimeters are so-called sampling calorimeters, which means that they are made of active detector layers and layers of absorber material. Figure 2.7 shows a cutaway view of the calorimeter system.

The ECal is a liquid-argon (LAr) sampling calorimeter with lead as the absorber material and liquid argon as the active material. It consists of three regions covering vast pseudo-rapidity ranges: barrel ($|\eta| < 1.475$) and end-caps ($1.375 < |\eta| < 3.2$).
The HCal consists of three parts. The central region has scintillating tiles as active material and steal as absorber material. In the barrel region it covers the pseudo-rapidity range

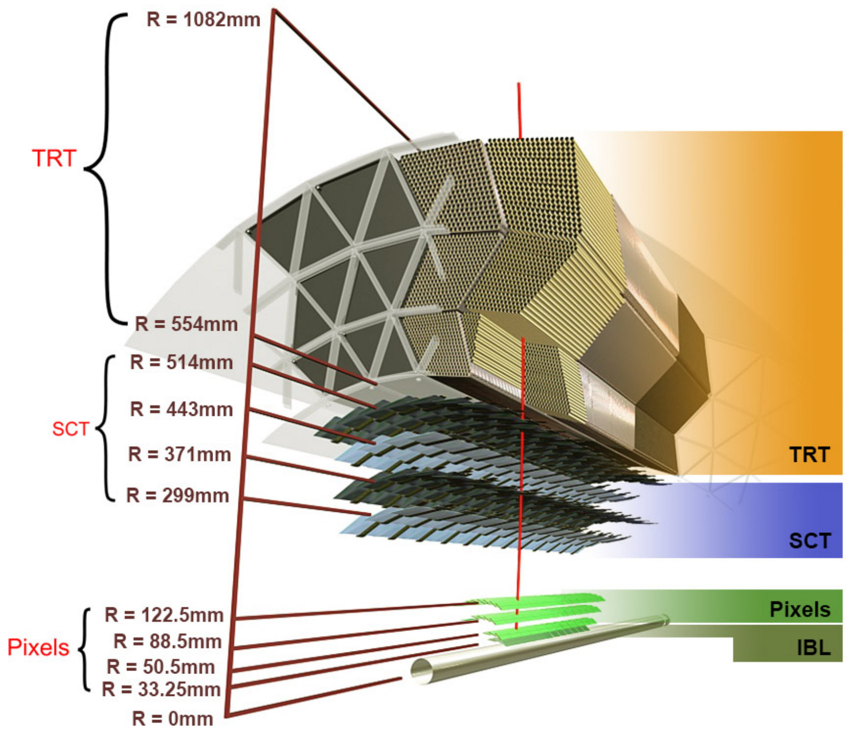

Figure 2.6: The drawing shows the structure of the Inner Detector with the sensors being traversed by a charged particle track in the barrel region. The track traverses successively the beryllium beam-pipe, the Insertable B-Layer, the three cylindrical silicon-pixel layers, the four cylindrical double layers of barrel silicon-microstrip sensors of the Semiconductor Tracker and several straws contained in the Transition Radiation Tracker modules [32].

$|\eta| < 1.0$, and in the extended barrel region the range $0.8 < |\eta| < 1.7$. The hadronic end-cap system utilises LAr as active and copper as absorber material and covers $1.5 < |\eta| < 3.2$. The forward calorimeter (FCal) measures particle tracks close to the beam line by covering pseudo-rapidities between 3.1 and 4.9. As the end-cap system it uses LAr as active, but different absorber materials.
The task of the HCal is the measurement of the energies of the hadron produced in a proton–proton collision. Its data are used for the reconstruction of jets and the measurement of missing transverse momentum, the so-called $E_{\mathrm{T}}^{\mathrm{miss}}$. The latter being precisely possible due to the large pseudo-rapidity coverage and the thickness of the calorimeter system.

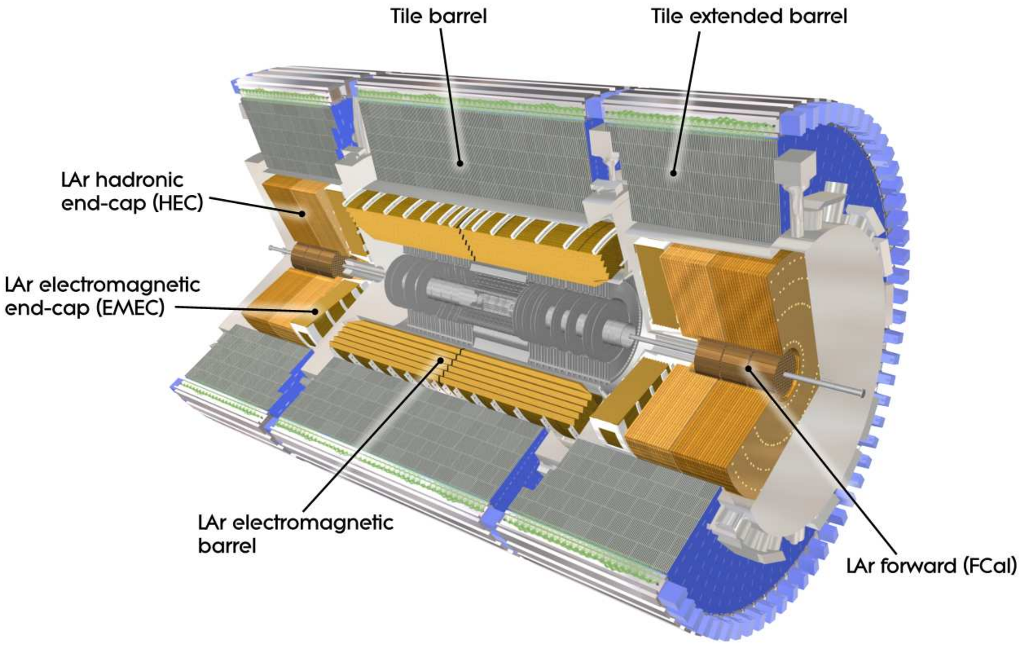

Figure 2.7: Cutaway view of the ATLAS calorimeter system showing the electromagnetic calorimeter in the barrel and end-cap regions, the hadronic calorimeters in the barrel and extended barrel as well as in the end-cap regions. Also the forward calorimeter can be seen close to the beam pipe [27].

2.2.3 The Muon Spectrometer

The main reason for the size of the ATLAS detector is the MS. It is immersed in a strong magnetic field generated by gigantic toroidal magnets, which bends the trajectories of muons to allow for a precise muon momentum measurement. Almost all particles of the SM that emerge from decays of resonances stemming from proton–proton collisions are measured by the ID or the calorimeter system and stopped by the latter. The only exceptions that reach the MS are muons and neutrinos. While the latter leave the detector without interaction, the energy and the trajectories of muons are measured with high accuracy in the MS. A schematic view of the MS is shown in Figure 2.8.

The MS is divided into three regions: the barrel (covering $|\eta| < 1.4$), the end-caps ($1.6 < |\eta| < 2.7$) and the transition ($1.5 < |\eta| < 1.6$) region. The barrel is made up of muon chambers in three layers of concentric cylindrical shells at distances 5, 7.5 and 10 m from the beam axis. Muon chambers in the end-caps are arranged as wheels perpendicular to the beam axis—three on each side.

Two of the four muon chambers that are being used follow a precision tracking purpose. The

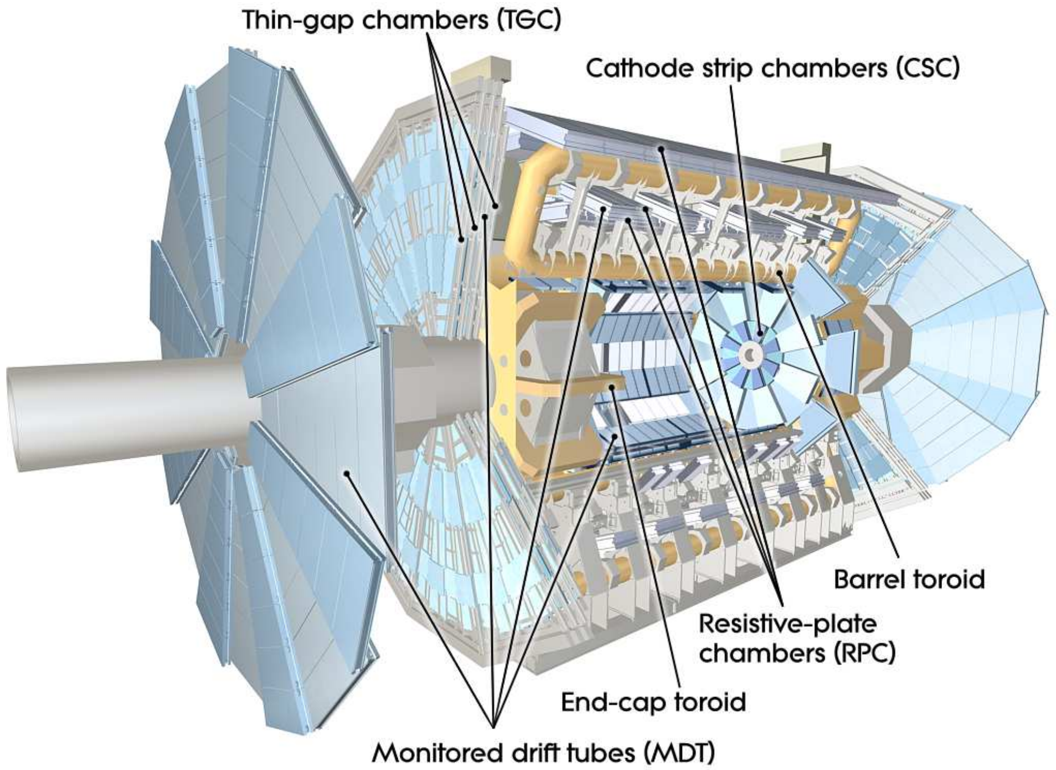

Figure 2.8: A cutaway view of the Muon Spectrometer visualising the arrangement of the components, which are the two tracking chambers (Monitored Drift Tube Chambers and Cathode Strip Chambers) and the two trigger chambers (Resistive Plate Chambers and Thin Gap Chambers). The toroids are shown as well [33].

Muon Drift Tube chambers (MDT) consist of aluminium tubes with a diameter of 30 mm. The anode wires of the tubes are operated at a voltage of 3080 V with respect to the tube walls, which are the cathodes. Argon atoms inside the tubes are ionised by traversing muons. The resulting electrons drift towards the anode wire, producing measurable avalanches. The drift radius can be measured with a precision of 80 µm.

Another type of precision tracking detectors is utilised in regions close to the beam line ($2 < |\eta| < 2.7$) called Cathode Strip Chambers (CSC), which are multi-wire proportional chambers with a cathode strip read-out. They use a gas mixture of $Ar : CO_2 : CF_4$ (30 % : 50 % : 20 %). The CSC is exposed to higher background rates of neutrons and gamma rays [34].

The other two muon chambers are used for triggering (see Section 2.2.4). The Resistive Plate Chambers (RPC) are placed in the barrel region and trigger on muon tracks with $|\eta| < 1.05$

while Thin Gap Chambers (TGC) cover the range $1.05 < |\eta| < 2.4$ in the end-cap regions. Both trigger chambers measure the muon trajectory coordinate in the bending (η) and the coordinate in the non-bending (ϕ) plane. Albeit having a poorer spatial resolution than the tracking chambers, signals for muon triggering and proton bunch collision time are provided in tenth of nanoseconds, making it possible to assign the detected muon to a proton–proton collision in which it has been produced. The RPC and TGC are part of the Level-1 (L1) trigger.

2.2.4 The trigger system

The proton bunches inside the LHC ring have a time-wise separation of about 25 ns, which means that $40 \cdot 10^6$ collisions take place inside the ATLAS Detector every second. As storing this amount of collision data is impossible, the usage of a dedicated trigger system, which filters for relevant events, is essential. The Trigger and Data Acquisition (TDAQ) system of the ATLAS Detector is a highly selective trigger system with a recording rate of 1 kHz from up to 40 MHz of collisions [35].
The drawing in Figure 2.9 shows the TDAQ system and its main trigger stages. The first stage is the hardware-based first-level trigger (L1), which uses mainly custom-made electronics. By taking inputs from the L1 calorimeter and L1 muon triggers, as well as other subsystems, the L1 trigger performs an initial selection of collision events. Selected events together with regions-of-interest (RoI) are buffered in the Read-Out System (ROS) and at the second stage processed by the high-level trigger (HLT). The HLT uses information from the calorimeter system, the ID and precise measurements from the MS. It utilises a two-stage approach. A fast first-pass reconstruction is performed, which rejects a great part of incoming events. The remaining events undergo a slower precision reconstruction procedure. Complementary to reconstructions in respective RoIs, they can also be performed for the full detector. After HLT acceptance, event information is transferred to local storage at the experimental site and exported to the Tier-0 facility at CERN's computing centre for offline reconstruction, using dedicated ATLAS reconstruction software [35].

2.3 Particle reconstruction and identification

The particles emerging from high-energy proton–proton collisions behave differently in the sub-detectors of the ATLAS detector, dependent on their charge, mass or the type of interaction they participate in. Accordingly, the traces they leave in each sub-detector are different. Figure 2.10 provides an illustrative presentation of particle tracks in the ATLAS detector: muon tracks curve in the magnetic field of the ID, traverse the calorimeter system with a small energy loss compatible to a minimum-ionising particle and are eventually traced in the MS. Photons first come into contact with the ATLAS detector in the ECal, where they produce an electromagnetic shower. Charged hadrons are deflected in the ID, interact with the ECal and lose their whole energy in the HCal by producing a shower. Neutral hadrons interact only with the HCal. Electrons have their tracks bent in the ID and are stopped by

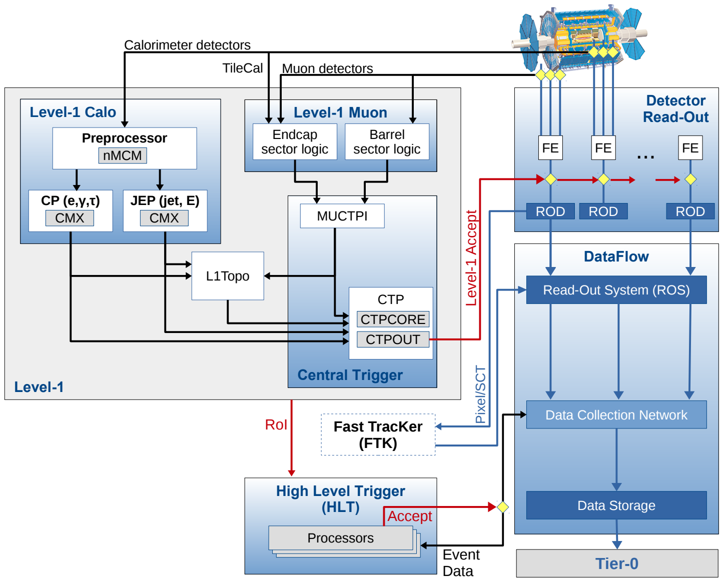

Figure 2.9: The Trigger and Data Acquisition system of the ATLAS detector from Run 2. The role of the Level-1 and the High-Level Trigger in selecting relevant collision events is identifiable [35].

the ECal, where they result in an electromagnetic shower. Neutrinos are the only particles of the SM that leave the ATLAS detector undetected and can only be traced down by means of missing transverse energy and momentum. The following sections discuss reconstruction and identification procedures of physics objects relevant in the $H \rightarrow ZZ^* \rightarrow 4\ell$ decay channel of the Higgs boson.

2.3.1 Track and vertex reconstruction

The reconstruction of trajectories of particles (primary or secondary) stemming from hard scattering processes in proton–proton bunch crossings as well as pinpointing the locations of the corresponding proton–proton collisions and secondary particle decays is crucial in analysing high-energy inelastic interactions between protons. The ID is mainly responsible for the reconstruction and identification of these so-called tracks and vertices. However, one bunch crossing does not yield exactly one high-energy proton–proton collision event, but on

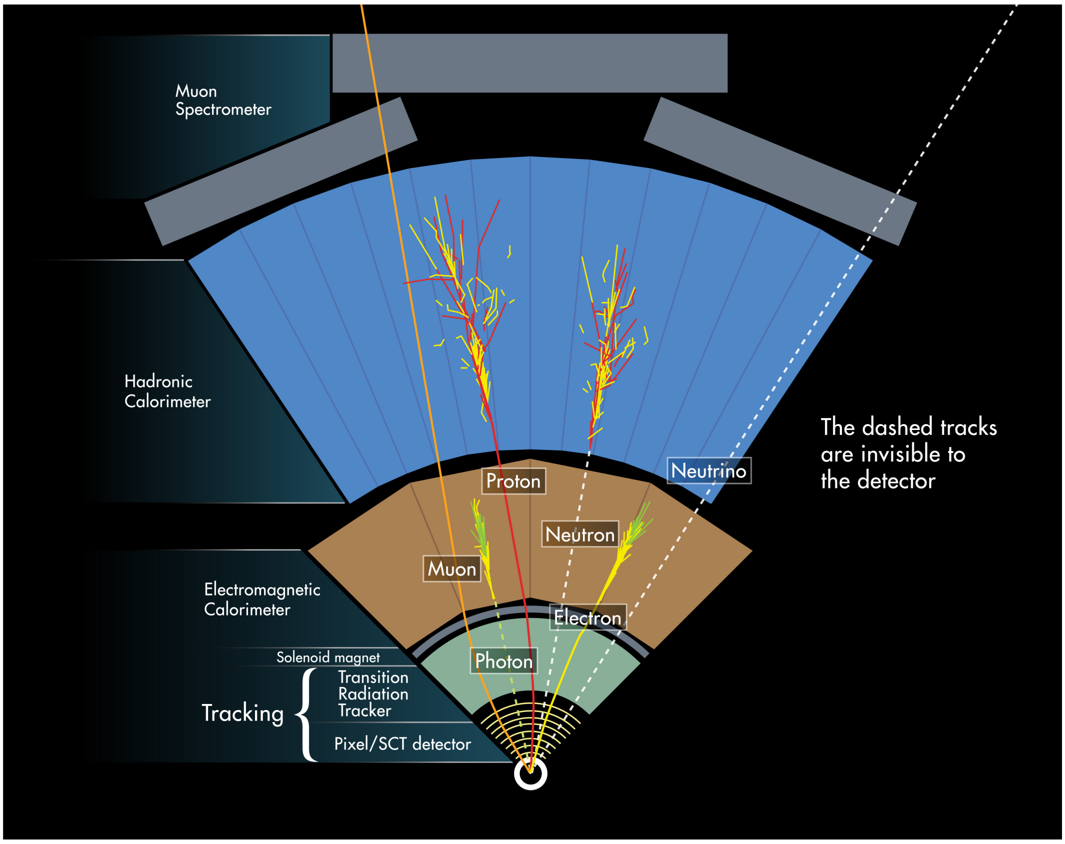

Figure 2.10: An illustration of particle reconstruction and identification at the ATLAS detector. Each type of particle leaves different kinds of traces in the sub-detectors and can be identified by combining the data of the different sub-detectors [36].

average 39 additional collisions, which is the current as of 2018 number of so-called in-time pile-up interactions [26]. Dedicated algorithms use information from all three sub-detectors of the ID to identify the main interaction vertex and the corresponding tracks and strive to minimise effects from high-density environments leading to misidentifications.
A sequence of algorithms is used to reconstruct tracks. Charged particle transitions result in clusters in the Pixel and SCT detectors, from which three-dimensional measurements, so-called space-points, are created. A minimal collection of three space-points constitutes track candidates, which then undergo various track finding criteria incorporating additional space-points. This procedure results in a very high efficiency for reconstructing primary particles and removing tracks created from random space-point collections. Furthermore, robust requirements, such as a minimum of nine hits in the silicon detectors and no holes in the Pixel Tracker, increase track reconstruction quality. Here, a hole means a non-existing but

expected measurement point given a track trajectory [37, 38].
Extrapolations of reconstructed tracks yield vertices as intersection points. A primary vertex finding algorithm associates reconstructed tracks to vertex candidates, followed by a vertex fitting algorithm, which reconstructs the position of the vertex together with a corresponding error. Due to pile-up more than one vertex is reconstructed. The largest sum of squared transverse momenta of corresponding tracks $\sum_{\mathrm{tracks}} p_{\mathrm{T}}^2$ is used to determine the primary vertex [37, 39].

2.3.2 Reconstruction and identification of electrons

Electrons and positrons, collectively referred to as electrons, are identified as clusters of energy depositions completely contained inside the ECal that can be matched to corresponding ID tracks. They allow for precise energy and momentum measurements at the ATLAS detector and therefore constitute important experimental signatures. They are identified with a high efficiency in the central region ($|\eta| < 2.47$) of the ATLAS detector.
The reconstruction procedure involves several steps. A clustering algorithm searches electron cluster 'seeds' as longitudinal towers in the ECal and reconstructs the kinematics of the clusters formed around the seeds. The efficiency of this search lies between 95 % (at $E_{\mathrm{T}} = 7$ GeV) and 99 % (at $E_{\mathrm{T}} = 15$ GeV). A track reconstruction then is performed, which uses pattern recognition and different approaches to handle energy loss due to interactions with detector material, before a track fitting algorithm performs track fitting. Electron specific track fitting loosely matches tracks to the electromagnetic clusters. By matching the track candidate to the cluster seed, the electron reconstruction is completed. With the final calibrated energy cluster and the best track the four-momentum of the electron is computed [40].
For a reconstructed electron candidate there are two possibilities: It is an electron, i. e. the reconstructed object is a signal, or it is hadronic jet or a converted photon, i. e. it is background. A sophisticated identification algorithm uses a multivariate analysis technique to make a decision. The likelihood-based method evaluates the properties of the electron candidate by using several discriminating variables from electron cluster and track measurements related quantities. The identification algorithm defines three reference sets of cuts called 'loose', 'medium' and 'tight' with increasing background rejection with efficiencies of 95 %, 92 % and 87 %, respectively. The $H \to ZZ^* \to 4\ell$ analysis (Chapter 4) uses calibrated 'loose' likelihood quality electrons which are identified with an efficiency of up to 95 %. Figure 2.11(a) shows the electron identification efficiency, which increases with higher transverse energy E_{T} and Figure 2.11(b) the background rejection efficiency decreasing with higher transverse energy.
As the number of reconstructed primary vertices increases with the number of pile-up collisions and some shower shape distributions are dependent on the number of primary vertices, the optimisation of the identification method includes simulations with numerous pile-up collisions [40].
The so-called *tag-and-probe* method [41] is also utilised in order to measure the electron identification efficiency from calibration data in $Z \to e^+e^-$ and $J/\psi \to e^+e^-$ events. Then cor-

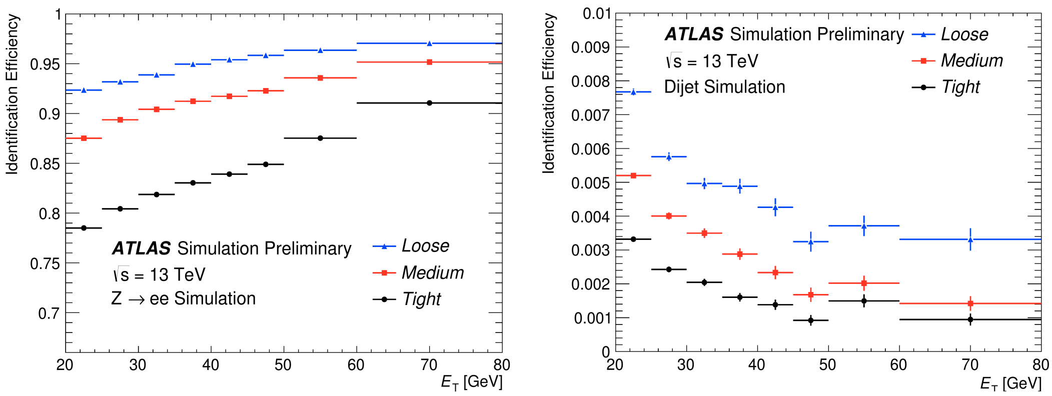

(a) (b)

Figure 2.11: The plots show (a) the identification efficiency of electrons from simulated Z boson decays and (b) the efficiency to identify hadrons as electrons by using simulated dijet events for the three working points 'loose' (triangle), 'medium' (square) and 'tight' (dot) against the transverse energy E_T. Monte Carlo simulations have been used in order to obtain the efficiencies, which are measured with respect to reconstructed electrons [40].

responding scale factors can be applied to MC based detector simulation electron efficiencies in order to reproduce the measured data efficiencies [40].

2.3.3 Reconstruction and identification of muons

The reconstruction of muons takes place independently in the ID as well as in the MS. While the ID performs a regular track reconstruction of the charged particle [42], a precise momentum reconstruction takes place in the MS [34]. A muon is identified as a charged particle track ranging from the ID to the MS. Four types of muons are distinguished in ATLAS:

Combined (CB) After independent track reconstruction in the ID and the MS, the track from the latter is extrapolated and via pattern recognition matched to the one from the ID. The reversed procedure is used as a complementary approach.

Segment-tagged (ST) Muons having a low transverse momentum p_T or traversing the MS in regions with reduced acceptance occasionally cross only one layer of MS chambers. Tracks from the ID that can be associated with at least one local MS track segment after extrapolation are classified as ST muons.

Calorimeter-tagged (CT) In some regions the MS is not instrumented with muon chambers. In this case an ID track that can be matched to an energy deposition in the calorimeter system which is compatible with a minimum-ionising particle—such as the muon—is reconstructed as a muon candidate.

Extrapolated (ME) The range $2.5 < |\eta| < 2.7$ is not covered by the ID. Trajectories reconstructed solely in the MS that are compatible with 'loose' requirements concerning the interaction point are classified as ME muons. The track parameters are defined at the interaction point and e. g. take into account estimated energy losses in the calorimeters.

Overlaps between two types are resolved before providing the muon collection for further analyses. For ID track overlaps, CB muons are preferred to ST and then to CT muons. Overlaps involving ME muons are resolved by taking into account track fit quality and the number of detector hits [34].
The identification process includes the application of quality requirements in order to reject muon candidates coming from background events—mainly decays of pions or kaons. Furthermore, a robust momentum measurement is guaranteed by invoking certain requirements on the number of hits in the ID and MS:

- ≥ 1 Pixel hits in the ID.
- ≥ 5 hits in the SCT.
- ≤ 3 Pixel or SCT holes.
- $\geq 10\,\%$ of original TRT hits are included in the final fit ($0.1 < |\eta| < 1.9$).

Four muon identification selections ('medium', 'loose', 'tight' and 'High-p_{T}') according to different analyses needs are provided. The $H \to ZZ^{*} \to 4\ell$ analysis uses 'loose' muons, which are optimised for Higgs boson analyses in the four-lepton channel: The reconstruction efficiency is maximised, while muon tracks of good quality are provided. Albeit all muon types are used in the 'loose' selection, CT and ST muons are restricted to the $|\eta| < 0.1$ region and in the range $|\eta| < 2.5$ about 97.5 % of the muons are of CB type [34].
The so-called *tag-and-probe* method [41] is used to measure the muon reconstruction and identification efficiency in $Z \to \mu^{+}\mu^{-}$ and $J/\psi \to \mu^{+}\mu^{-}$ decays. Discrepancies between data and simulation are corrected by the application of a scale factor.
With the exception of the central region $|\eta| < 0.1$, efficiencies around 99 % are observed over the full η range. Figure 2.12 shows the efficiency for 'medium' muons from Z boson decay simulations and early 2015 $\sqrt{s} = 13$ TeV data taking, as well as for the 'loose' selection in the region $|\eta| < 0.1$. Here lies the MS acceptance gap, which is filled by calorimeter- and segment-tagged muons in the 'loose' selection, which explains the significant difference in reconstruction efficiency. Throughout the rest of the the detector the efficiencies for 'medium' and 'loose' selections are very similar [34]. The drop in the central region below 70 % is in agreement with predictions from detector simulation [43].

2.3.4 Reconstruction and identification of jets

In high-energy proton–proton collisions many quarks or gluons are produced. Due to confinement they hadronise and produce collimated streams of particles—referred to as jets.

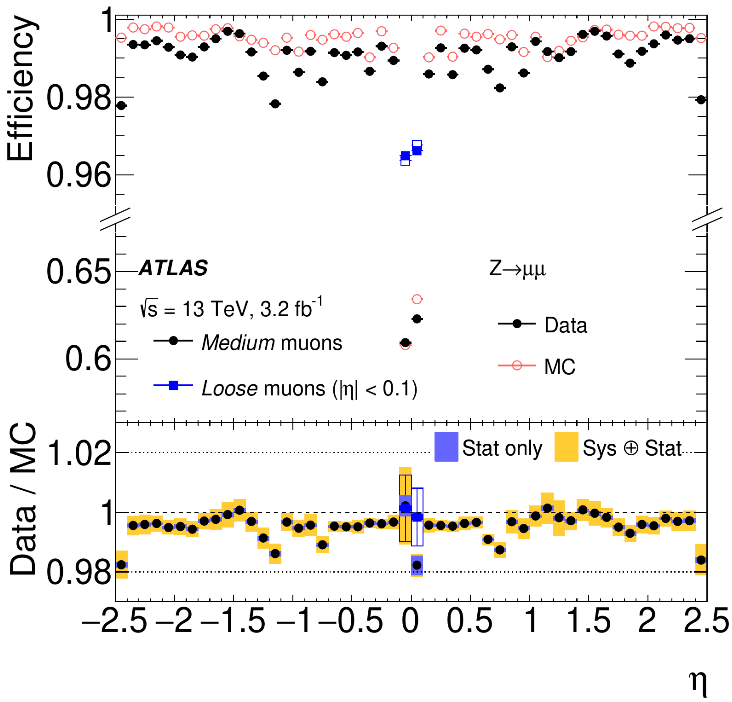

Figure 2.12: The 'medium' muon reconstruction efficiency as a function of the pseudo-rapidity of the muon in the range $|\eta| < 2.5$ from $Z \rightarrow \mu^+\mu^-$ decays (red circles) and 2015 collision data (black dots). In addition, the efficiency for 'loose' muons is shown as blue squares, albeit only for the region $|\eta| < 0.1$, where it significantly differs from the 'medium' selection. An additional panel at the bottom displays the ratio between the expected and observed efficiencies [34].

They can be observed in the ATLAS detector as topologically connected energy depositions in the calorimeters [44]. ATLAS uses the anti-k_t jet reconstruction algorithm [45], which builds a cluster formation from calorimeter cells with a signal-to-noise ratio of at least four within a certain radius, expressed with the distance parameter $R = 0.4$. Alongside the three-dimensional calorimeter topological cluster information, a four-momentum recombination scheme is provided as algorithm input [46].
The jet reconstruction procedure includes the correction of the jet energy by applying several correction factors to account for particles undetected in the calorimeters or not clustered in the jet [44].
Beam induced background or calorimeter noise is handled by applying a set of quality criteria. As in the reconstruction procedure of electrons or muons, the degree of rejection defines 'tight', 'medium' and 'loose' working points, where the latter is used by the $H \rightarrow ZZ^* \rightarrow 4\ell$ analysis. The *tag-and-probe* method is used in order to measure the efficiencies of the jet

quality selections in dijet events and to adjust MC based efficiencies to the values from data measurements [47]. Figure 2.13 shows the efficiency for anti-k_t jets of 'loose' and 'tight' quality selection criteria. It can be seen, that the selection efficiency is close to unity and approximately equal for the 'loose' and 'tight' working points in the jet pseudo-rapidity region $|\eta| \geq 2.5$ (except for one bin). For $|\eta| \leq 2.5$ the 'tight' selection criteria result in a slightly lower efficiency than the 'loose' selection criteria due to a fake jet rejection requirement in the central η region.

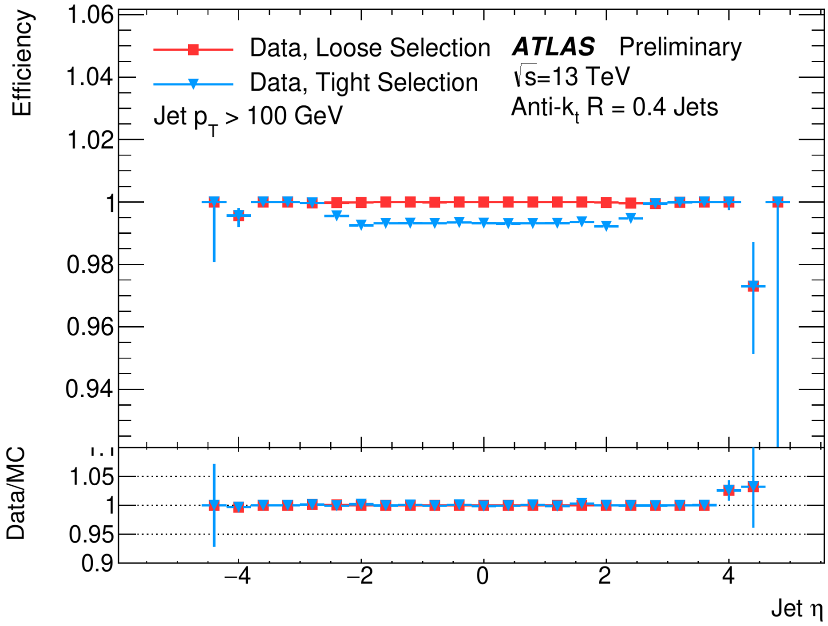

Figure 2.13: Jet quality selection efficiency for jets reconstructed using the anti-k_t algorithm with distance parameter $R = 0.4$ as a function of the pseudo-rapidity η. A cut on the transverse momentum of the jets of $p_T > 100\,\text{GeV}$ has been applied. The 'loose' selection criteria is depicted by squares, whereas triangles are used for the 'tight' working point. The efficiencies were measured with the *tag-and-probe* technique [47].

3
Theoretical foundations

In this and the following chapters a system of units is used in which $\hbar = c = 1$. So mass, momentum and energy all come in units of GeV and length and time are measured in units of GeV^{-1}. If necessary, all factors of $\hbar$ and c can be reconstructed by dimensional analysis [48].

3.1 Elementary particles and interactions

Our present understanding of the constituents of matter and their interactions is described by the Standard Model of particle physics in a remarkably successful manner, supported by experimental results from measurements of highest precision. The SM is a so-called gauge invariant quantum field theory based on the symmetry group $SU(3) \times SU(2) \times U(1)$, where $SU(3)$ is the colour group of the strong interaction and $SU(2) \times U(1)$ the group of the combination of the electromagnetic and the weak interaction, the electroweak interaction [49]. The only fundamental force not described by the SM is gravity, explained in the General Theory of Relativity.

The fundamental particles of the SM are grouped according to their quantum numbers. The SM contains spin–$\frac{1}{2}$ fermions, spin–1 gauge bosons and the spin–0 Higgs boson. Figure 3.1 gives an overview of the SM particles.

The fermions are grouped in left-handed isospin doublets which are the fundamental representations of the $SU(2)$ group. Fermions that take part in the strong interaction are called quarks while fermions that take part only in the electroweak interaction are called leptons. There are three families of quarks and leptons.

The strong interaction is mediated by spin–1 gluons. The weak interaction is mediated by the W^+, W^- and the Z bosons. The mediator of the electromagnetic interaction is the photon. Contrary to the gluons and the photon, the W and Z bosons are massive. In order to introduce masses to the W and Z bosons as well as to the fermions in a gauge invariance preserving way, the $SU(2) \times U(1)$ symmetry is spontaneously broken in the SM. The *Englert–Brout–Higgs mechanism* of electroweak symmetry breaking also leads to an observable massive scalar particle, the so-called *Higgs boson*.

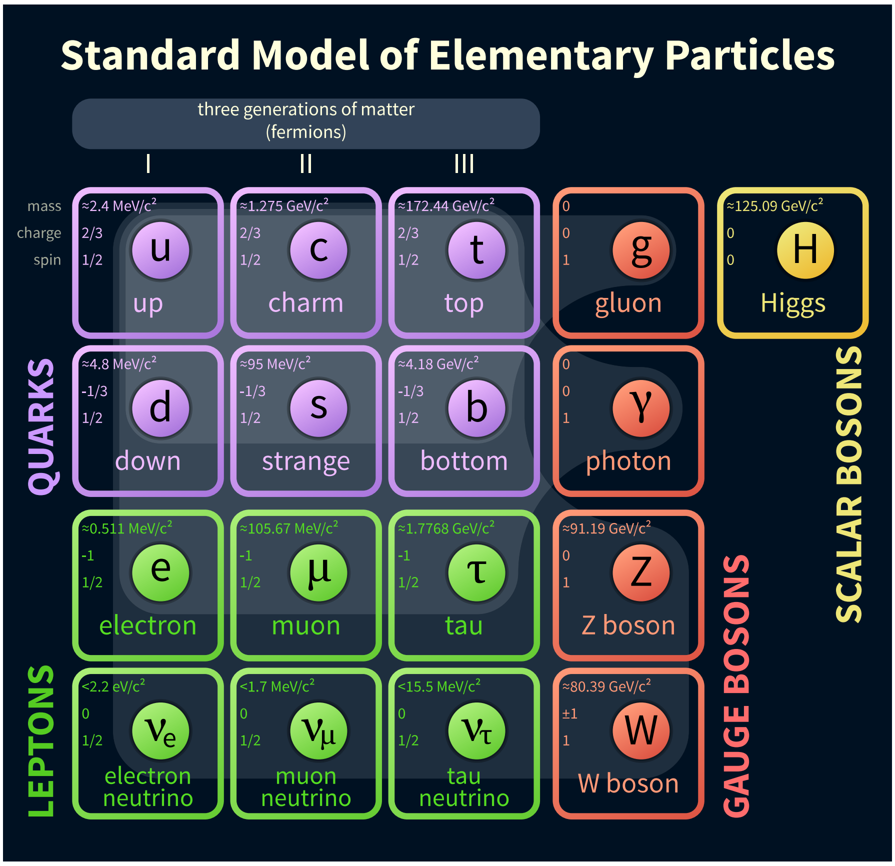

Figure 3.1: The elementary particles of the Standard Model are shown and grouped by their quantum numbers. For each particle the mass, charge (in units of the elementary charge e) and spin are shown. Three columns emphasise the fermion generations and an underlaid grey shade indicates the couplings to the gauge bosons [50].

Quantum Electrodynamics

Developed in the 1940s by Feynman, Schwinger and Tomonaga, Quantum Electrodynamics (QED) is one of the most precisely tested theory in science. It is a quantum field theory with an underlying $U(1)$ symmetry. Starting from the Lagrangian density—commonly just called the *Lagrangian*—of a free charged fermion field ψ

$$\mathscr{L}_0 = \overline{\psi}\left(\mathrm{i}\gamma^{\mu}\partial_{\mu} - m\right)\psi\,,$$

where ψ is the Dirac 4-spinor and $\overline{\psi}$ its adjoint, γ^{μ} the γ-matrices, m the mass of the fermion and $\partial_\mu = \partial/\partial x^\mu$ the 4-derivative, one obtains with the help of the Euler–Lagrange-Equations the *Dirac-Equation* as the equation of motion

$$\left(\mathrm{i}\gamma^\mu \partial_\mu - m\right)\psi = 0 .$$

Let $\alpha(x)$ be a real differentiable function of a space-time point x. The transformation

$$\psi(x) \longmapsto \mathrm{e}^{-\mathrm{i}\alpha(x)}\psi(x) ,$$

is called a local $U(1)$ gauge transformation [48]. The Lagrangian $\mathscr{L}_0$ is not invariant under local $U(1)$ gauge transformations. By introducing an additional coupling between fermions and the vector field $A_\mu(x)$ and minimally substituting the derivative by the so-called *covariant derivative* $D_\mu = \partial_\mu - \mathrm{i}eA_\mu$, local $U(1)$ gauge invariance can be achieved, if A_μ transforms as

$$A_\mu(x) \longmapsto A_\mu(x) + \frac{1}{e}\partial_\mu \alpha(x) .$$

In order to identify the gauge field A_μ with the photon, which couples to the fermions with a coupling strength e, where the charge of an electron is $-e$, one has to make it a dynamical field by adding a term corresponding to its kinetic energy. With the definition of the field strength tensor $F_{\mu\nu} = \partial_\mu A_\nu - \partial_\nu A_\mu$ the Lagrangian of QED reads:

$$\mathscr{L}_{\mathrm{QED}} = \overline{\psi}\left(\mathrm{i}\gamma^\mu \partial_\mu - m\right)\psi + e\overline{\psi}\gamma^\mu A_\mu \psi - \frac{1}{4}F^{\mu\nu}F_{\mu\nu} .$$

An additional term of the form $m^2 A^\mu A_\mu$ would violate local gauge invariance and therefore the photon described by the vector field A_μ is a massless particle [51].

Quantum Chromodynamics

The quantum field theory describing the strong interaction is a gauge theory of a local $SU(3)$ symmetry. The basic fermions are six quarks, which come in the colour states *red*, *blue* and *green*. Each quark flavour (Figure 3.1) can be represented by a triplet of fermion fields $\Psi \equiv \left(\psi_\mathrm{r}, \psi_\mathrm{b}, \psi_\mathrm{g}\right)^\mathrm{T}$ with the free Lagrangian

$$\mathscr{L}_0 = \overline{\Psi}\left(\mathrm{i}\gamma^\mu \partial_\mu - m\right)\Psi .$$

The global $SU(3)$ symmetry of the Lagrangian needs to hold locally, i. e. $\mathscr{L}_0$ has to be invariant under gauge transformations of the form

$$\Psi(x) \longmapsto \mathrm{e}^{\frac{\mathrm{i}}{2}\alpha_a(x)\lambda_a}\Psi(x) ,$$

with $\alpha_a(x)$ being generalised phases and λ_a the so-called *Gell-Mann matrices* for $a = 1, \ldots, 8$ and an implied summation over a. Similarly to the approach conducted in QED, the introduction of (eight) gauge fields G^a_μ leads to the desired local $SU(3)$ invariance. However, for a gauge invariant Lagrangian the transformation prescription

$$G^a_\mu \longmapsto G^a_\mu - \frac{1}{g}\partial_\mu \alpha^a - f^{abc}\alpha^b G^c_\mu \tag{3.1}$$

for the gauge fields is necessary, where a, b, c run from 1 to 8, f_{abc} are the real-valued structure constants of the $SU(3)$ group and g the coupling constant of the strong interaction. The Lagrangian for QCD then reads:

$$\mathscr{L}_{\text{QCD}} = \overline{\Psi}\left(\mathrm{i}\gamma^\mu\partial_\mu - m\right)\Psi - \frac{g}{2}\left(\overline{\Psi}\gamma^\mu\lambda^a\Psi\right)G^a_\mu - \frac{1}{4}G^a_{\mu\nu}G^{a,\mu\nu} . \tag{3.2}$$

As in the case of photons in QED, local invariance requires the gauge bosons to be massless. The last term in (3.2) is a gauge invariant kinetic term, which due to the additional term in (3.1) is not purely kinetic, but includes interactions between the gauge bosons described by the gauge fields G^a_μ. Identifying these vector bosons with gluons, it follows that gluons must carry colour charge and henceforth interact with each other. This feature arises from the so-called non-Abelian character of the gauge group [48].

The coupling constant of the strong interaction is actually not constant, but depends on the spatial separation between particles, decreasing with smaller distances. This feature results in the so-called *asymptotic freedom*, which means that quarks on scales smaller than the ones characteristic for nuclear physics, e.g. smaller than the diameter of a proton, interact very little with each other.

On the other hand, a phenomenon known as *confinement* is the mere appearance of colourless quark states, i. e. quarks can only be found in nature in bound states where the colours cancel (e.g. a colour and anti-colour quark pair forming a *meson*) or add up to 'white' (e.g. the three quarks of a *baryon* with colours of red, blue and green) [51].

Weak interactions and electroweak unification

The weak force is present on sub-atomic scales and plays its most prominent roles in radioactive decays or fusion processes inside the sun. Weak interactions between particles with *weak isospin* I_3, which is the third component of the weak isospin vector $\vec{I}$, are mediated by the massive gauge bosons $W^\pm$ and Z, whose non-zero masses are in accordance to the short range of the interaction. The fermions participating in the weak interaction all have an isospin

of ± 1/2. The weak force permits flavour changing interactions between quarks, e.g. in the neutron beta decay $n \to p + e + \bar{\nu}_e$. Vertex factors of weak interactions contain vector and axial vector parts. This mixed V–A character of the coupling of the $W^{\pm}$ bosons is responsible for the maximal parity violation of the weak force: only 'left-handed' helicity state fermions and 'right-handed' helicity state anti-fermions interact with the gauge bosons of the weak force [51].
While the weak force couples the left-handed helicity state lepton doublets

$$\begin{pmatrix} e \\ \nu_e \end{pmatrix}_{\mathrm{L}}, \quad \begin{pmatrix} \mu \\ \nu_\mu \end{pmatrix}_{\mathrm{L}}, \quad \begin{pmatrix} \tau \\ \nu_\tau \end{pmatrix}_{\mathrm{L}},$$

i. e. conserves lepton flavour, it couples quark weak eigenstates

$$\begin{pmatrix} u \\ d' \end{pmatrix}_{\mathrm{L}}, \quad \begin{pmatrix} c \\ s' \end{pmatrix}_{\mathrm{L}}, \quad \begin{pmatrix} t \\ b' \end{pmatrix}_{\mathrm{L}}.$$

The linear combinations

$$\begin{pmatrix} d' \\ s' \\ b' \end{pmatrix} = \begin{pmatrix} V_{ud} & V_{us} & V_{ub} \\ V_{cd} & V_{cs} & V_{cb} \\ V_{td} & V_{ts} & V_{tb} \end{pmatrix} \begin{pmatrix} d \\ s \\ b \end{pmatrix}$$

defined by the Cabbibo–Kobayashi–Maskawa matrix allow for transitions between different quark generations with couplings between the quarks ij measured with the quantity V_{ij} [51].
The unified description of electromagnetism and the weak interaction, formulated by Glashow, Salam and Weinberg in the 1960s, describes the electromagnetic and weak interactions as manifestations of one gauge theory with underlying[1] $SU(2)_{\mathrm{L}} \times U(1)_Y$ symmetry. A relation between the electric charge Q, the weak isospin and the hypercharge Y is established by Gell-Mann and Nishijima

$$Q = I_3 + \frac{Y}{2}.$$

The dynamics of the gauge bosons are encoded in the Lagrangian

$$\mathscr{L}_{\mathrm{gauge}} = -\frac{1}{4} W^a_{\mu\nu} W^{a,\mu\nu} - \frac{1}{4} B_{\mu\nu} B^{\mu\nu}$$

in terms of field strength tensors

[1] The subscript 'L' emphasises the exclusive participation of left-handed helicity state fermions in the interaction.

$$W^a_{\mu\nu} = \partial_\mu W^a_\nu - \partial_\nu W^a_\mu + g\varepsilon^{abc} W^b_\mu W^c_\nu$$
$$B_{\mu\nu} = \partial_\mu B_\nu - \partial_\nu B_\mu \,,$$

with a, b, c from 1 to 3, the totally antisymmetric tensor defined so that $\varepsilon^{123} = 1$ and g being the weak interaction coupling strength. Gauge interactions of fermions or scalars are described by the covariant derivative

$$D_\mu = \partial_\mu - \mathrm{i}g' B_\mu Y - \mathrm{i}g W^a_\mu T^a \,, \tag{3.3}$$

with g' the coupling strength of the weak hypercharge interaction, Y the hypercharge operator and T^a the $SU(2)_\mathrm{L}$ generators.
A gauge boson mass term $\mathscr{L} \supset \frac{1}{2} m^2 B_\mu B^\mu$ however breaks local gauge invariance, which results in massless gauge bosons—contrary to experimental results [52, 53].
Since $SU(2)_\mathrm{L} \times U(1)_Y$ gauge transformations depend heavily on the helicity state, chiral fermion fields have to be considered, obtained by a projection $\psi_{\mathrm{L/R}} \equiv P_{\mathrm{L/R}}\psi$ with $P_{\mathrm{L/R}} = (1 \mp \gamma^5)/2$. Rewriting the Dirac Lagrangian in terms of these chiral fields leads to neatly separated kinetic terms for ψ_L and ψ_R, so that by invoking minimal substitution the covariant derivative incorporates gauge transformation properties, guaranteeing local gauge invariance. However, the appearing mass terms all contain both helicity state fields, which carry different $SU(2)_\mathrm{L} \times U(1)_Y$ charges, thus violating local gauge invariance [53].
Non-zero fermion and weak interaction gauge boson masses can be incorporated into the SM Lagrangian by invoking the Englert–Brout–Higgs mechanism [54–57] of spontaneous symmetry breaking.

The Higgs mechanism

The addition of a new $SU(2)_\mathrm{L}$ doublet field Φ to the SM,

$$\Phi = \begin{pmatrix} \phi^+ \\ \phi^0 \end{pmatrix} = \frac{1}{\sqrt{2}} \begin{pmatrix} \phi_1 + \mathrm{i}\phi_2 \\ \phi_3 + \mathrm{i}\phi_4 \end{pmatrix} \,,$$

with real scalar fields ϕ_i, leads to new terms in the Lagrangian

$$\mathscr{L}_\Phi = \left(D_\mu \Phi\right)^\dagger \left(D^\mu \Phi\right) - V(\Phi) + \mathscr{L}_\mathrm{Yukawa} \,. \tag{3.4}$$

The *Higgs field* Φ is a complex scalar field with two isospin components, i. e. having four degrees of freedom. Thus $SU(2)_L \times U(1)_Y$ gauge transformations correspond to rotations in this four-dimensional space. The general gauge invariant potential energy function of Φ,

$$V(\Phi) = -\mu^2 \Phi^\dagger \Phi + \lambda \left(\Phi^\dagger \Phi\right)^2 , \tag{3.5}$$

is visualised in Figure 3.2. It has for $\lambda > 0$ and $-\mu^2 < 0$ a minimum at $|\Phi| \equiv \sqrt{\Phi^\dagger \Phi} \neq 0$. The minimum of the scalar potential $V(\Phi)$ at $\Phi^\dagger \Phi = \mu^2/(2\lambda)$ defines a spherical surface in four dimensions upon which the states of minimal energy lie. Choosing one particular state as the vacuum state and reformulating the Lagrangian in terms of deviations around this new ground state make the breaking of the symmetry apparent. The former Lagrangian being even in Φ now lost its symmetry concerning the new field variable. However, still the same physical system is described, merely the symmetry is being concealed by this *spontaneous symmetry breaking*.

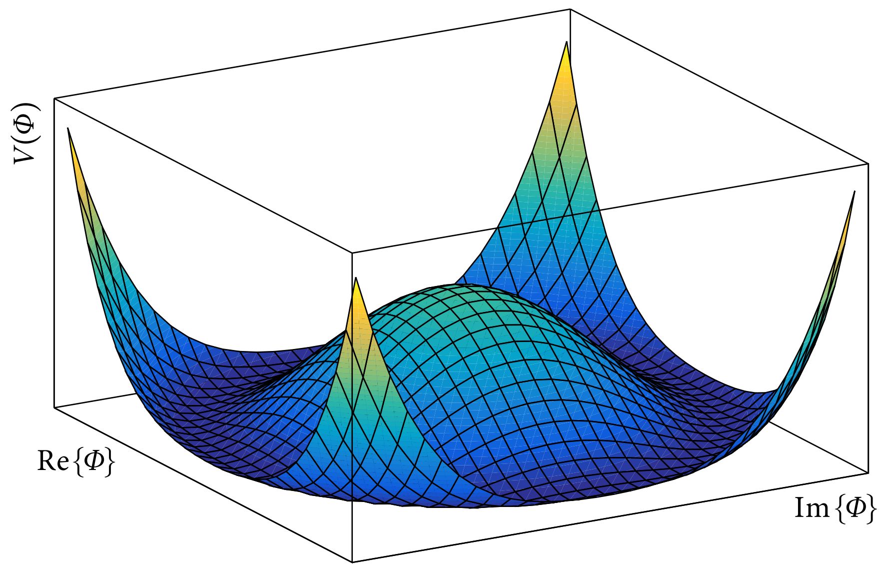

Figure 3.2: Three-dimensional plot of the potential energy function of the Higgs field, also known as the Mexican hat potential. It illustrates the maximum as an unstable ground state at $|\Phi| = 0$ and infinitely many new stable ground states at $|\Phi|^2 = \mu^2/(2\lambda)$. Choosing one particular new ground state leads to the spontaneous symmetry breaking [58].

For the particular choice of the vacuum state as $\langle\phi_1\rangle = \langle\phi_2\rangle = \langle\phi_4\rangle = 0$ and $\langle\phi_3\rangle \equiv v = \sqrt{\mu^2/\lambda}$, the mass terms in the potential function (Eq. 3.5) for the fields ϕ_1, ϕ_2 and ϕ_4 are zero, whereas the new real scalar field h with zero vacuum expectation value $\phi_3 = h + v$ yields a mass term $m_h = \sqrt{2\lambda v^2}$. For infinitesimal fluctuations about the vacuum, the Higgs field can be equivalently written as

$$\Phi = \frac{1}{\sqrt{2}} \exp\left(\frac{\mathrm{i}\xi^a \sigma^a}{v}\right) \begin{pmatrix} 0 \\ v + h \end{pmatrix},$$

with fields ξ^a and Pauli matrices σ^a summed over 1, 2, 3. Considering the gauge transformation of the $SU(2)_\mathrm{L}$ symmetry group

$$\Phi \longmapsto \exp\left(\mathrm{i}\lambda_\mathrm{L}^a(x) \frac{\sigma^a}{2}\right) \Phi$$

and the so-called unitary gauge $\lambda_\mathrm{L}^a(x) = -2\xi^a/v$, the Higgs field can be written solely in terms of the massive, real scalar field h

$$\Phi = \frac{1}{\sqrt{2}} \begin{pmatrix} 0 \\ v + h \end{pmatrix}.$$

The first term in Eq. 3.4 contains covariant derivatives of the form in Eq. 3.3 applied to the Higgs field Φ. The detailed study of the expression [53] reveals a properly normalised kinetic term for the real scalar field h and a term corresponding to the $W^\pm$ bosons

$$W_\mu^\pm = \frac{W_\mu^1 \mp \mathrm{i} W_\mu^2}{\sqrt{2}}$$

with an accompanying mass term $m_W^2 = g^2 v^2/4$, where $v \approx 246\,\mathrm{GeV}$ is the vacuum expectation value of the Higgs field, which is obtained by measurement of the $W^\pm$ boson mass or with the aid of the Fermi constant $G_\mathrm{F} = 2^{-1/2} v^2$ [59]. Further terms lead similarly to an expression for the Z boson

$$Z_\mu = \frac{1}{\sqrt{g^2 + g'^2}} \left(g W_\mu^3 - g' B_\mu\right)$$

and a corresponding mass term $m_Z^2 = \left(g^2 + g'^2\right) v^2/4$. They all couple to the excitation of the Higgs field, the *Higgs boson h*. The state orthogonal to Z_μ does not appear, thus is not interacting with the Higgs boson and is therefore massless and can be identified with the photon field A_μ [53].
Using the weak mixing angle θ_W defined as

$$\cos\theta_\mathrm{W} = \frac{g}{\sqrt{g^2 + g'^2}} = \frac{g}{g'} \sin\theta_\mathrm{W},$$

the expressions and current values [60] for the gauge boson masses can be summarised as

$$\begin{aligned} m_W &= \frac{gv}{2} = 80.379 \pm 0.012\text{GeV} , \\ m_Z &= \frac{m_W}{\cos\theta_\text{W}} = 91.1876 \pm 0.0021\text{GeV} , \\ m_h &= v\sqrt{2\lambda} = 125.18 \pm 0.16\text{GeV} . \end{aligned} \tag{3.6}$$

The last term in Eq. 3.4 describes the coupling to fermions. Following the requirements of Lorentz invariance, mass dimension value for terms in the Lagrangian and that Φ is an $SU(2)_\text{L}$ doublet, the Lagrangian $\mathscr{L}_\text{Yukawa}$ can be constructed. Using unitary gauge for Φ and reformulating reveals mass terms for fermions proportional to v, the Higgs vacuum expectation value [53]. The couplings of the SM Higgs boson to gauge bosons, fermions and the Higgs boson self coupling can be summarised with the following Lagrangian [52, Chapter 11]

$$\mathscr{L} = -g_{hff}\bar{f}fh + \frac{1}{3!}g_{hhh}h^3 + \frac{1}{4!}g_{hhhh}h^4 + \delta_V V_\mu V^\mu \left(g_{hVV}h + \frac{1}{2}g_{hhVV}h^2\right) ,$$

where $V = W$ or $V = Z$, $\delta_W = 1$, $\delta_Z = 1/2$ and the self coupling strengths are

$$g_{hhh} = \frac{3m_h^2}{v} , \quad g_{hhhh} = \frac{3m_h^2}{v^2} .$$

The linear and quadratic mass dependence of the coupling to fermions and heavy vector bosons, respectively, can be found in the expressions

$$g_{hff} = \frac{m_f}{v}, \quad g_{hVV} = \frac{2m_V^2}{v}, \quad g_{hhVV} = \frac{2m_V^2}{v^2} .$$

Neutrinos have been originally considered to be massless in the Standard Model. Although the discovery of neutrino oscillations [61–63] implies them to have a non-vanishing mass and thus interacting with the Higgs boson, neutrino masses and neutrino oscillations can be neglected in collider experiments due to the smallness of their masses.

3.2 Higgs phenomenology

3.2.1 Higgs boson production in high-energy proton–proton collisions at the LHC

high-energy proton–proton collisions are complex on many levels. The main scattering process is accompanied by bremsstrahlung, hadronisation and secondary soft interaction processes [64, 65]. The collisions can be classified as hard or soft scattering processes [66]. While the first are characterised by a high transverse energy interaction and often lead to the creation of resonances of high mass such as the Higgs boson, soft processes usually describe everything else [67]. They often result in final state radiation and are from a calculatory point of view difficult to handle. Soft scattering effects are accounted for through experimental measurements and the tuning of Monte Carlo samples. However, perturbation theory can be applied to hard scattering quite effectively guaranteeing high precision results.
Hard scattering processes between the quarks and gluons of the colliding protons are treated in the parton model. Accordingly, parton distribution functions $f(x_i, Q^2)$ are utilised to account for the probability to find a particular parton i with momentum fraction $0 < x_i < 1$ of the total momentum of the proton. Also, the dependence on the momentum transfer Q^2 is considered. With the factorisation theorem [68] the production cross-section for the process where two partons (a from proton p_A and b from proton p_B) collide and one Higgs boson together with additional particles X is created can be written as

$$\sigma(p_A + p_B \to H + X) = \int \mathrm{d}x_a \, \mathrm{d}x_b \, f_{a/A}(x_a, \mu_\mathrm{F}^2) f_{b/B}(x_b, \mu_\mathrm{F}^2) \hat{\sigma}_{ab\to H}(\mu_\mathrm{F}^2, \mu_\mathrm{R}^2) \,,$$

where μ_F and μ_R are the factorisation scale and the renormalisation scale of the running strong coupling constant, respectively. The PDFs cannot be calculated, but are for instance retrieved from deep inelastic electron–proton scattering measurements. They are extrapolated to the high energies of the LHC using the DGLAP evolution equations [69–71].
With the LHC providing high centre-of-mass energies, heavy particles like the Higgs boson can be produced in proton–proton collisions. Figure 3.3 depicts the tree-level Feynman diagrams of the main production modes described below. The cross-section values for a Higgs boson mass $m_H = 125.09$ GeV and a centre-of-mass energy $\sqrt{s} = 13$ TeV are summarised in Table 3.1. Even though different from the most current value (see Eq. 3.6), within the work of this thesis always a Higgs boson mass value of $m_H = 125.09$ GeV is used, because this value was the most current one at the time the data sets and software utilities used in this work, were created.

ggF The dominant Higgs boson production process at the LHC is the gluon–gluon fusion (ggF), where two gluons annihilate into a Higgs boson by means of an intermediate heavy quark loop. Since the coupling between the Higgs boson and SM particles is proportional to the respective mass of the particle, at tree-level the Higgs boson hardly couples to light

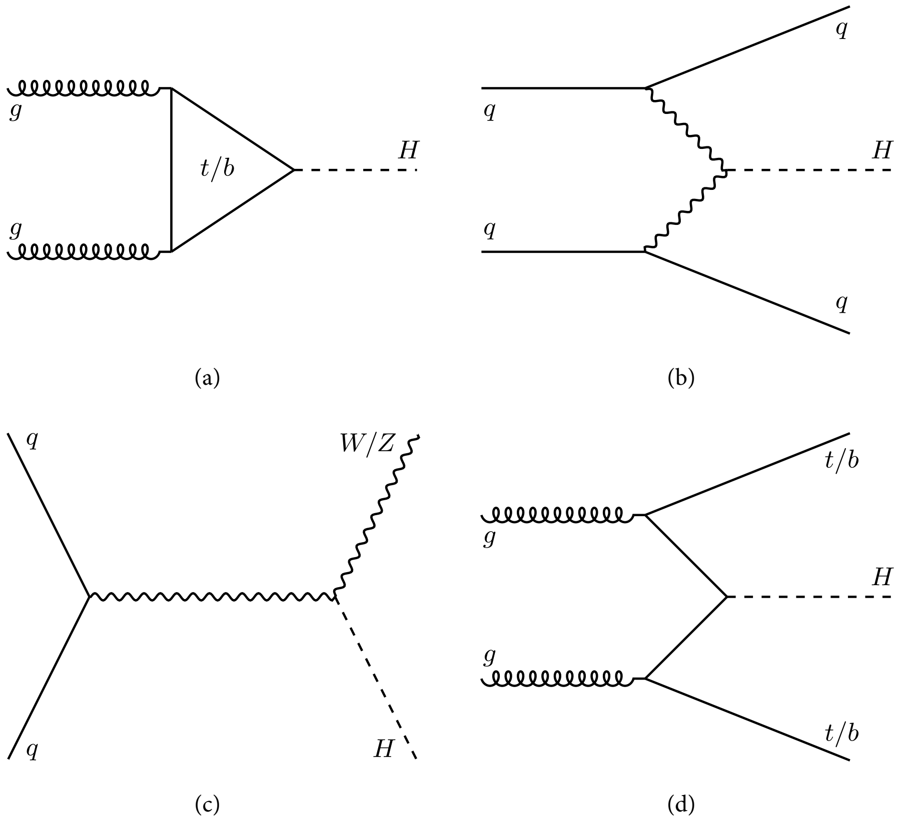

Figure 3.3: Feynman diagrams of the main production modes of the Higgs boson at the LHC with decreasing dominance: (a) gluon–gluon fusion with an intermediate heavy quark loop, (b) vector-boson fusion, (c) associate production with weak vector bosons and (d) associate production with heavy quarks [72].

quarks and not at all to gluons. However, with the gluon PDF at energies of the LHC being small at momentum fractions $x \lesssim 1$ and growing rapidly towards small x, the proton consists mostly of gluons. The top quark has a strong coupling to gluons and due to its high mass the strongest coupling to the Higgs boson out of all SM particles. This leads to the highest Higgs boson production cross-section for the ggF production via an intermediate top quark loop (Figure 3.3(a)) [75]. A minor contribution from bottom quarks is also present. Due to its relevance for this thesis, the ggF production process is covered in Section 3.4.1 in more detail.

VBF The Higgs boson production process where initial state quarks emit weak vector bosons (W, Z bosons) followed by a fusion of these bosons into a Higgs boson is called *vector-boson fusion* (or sometimes weak-boson fusion) (VBF). Besides being the second most

Table 3.1: Production cross-sections for the Higgs boson production mechanism of the four main production modes at the LHC. The cross-section values and $\pm(\text{PDF} + \alpha_S)$ % uncertainties given are of currently highest accuracy and with respect to a Higgs boson mass of $m_H = 125.09$ GeV and a centre-of-mass energy of $\sqrt{s} = 13$ TeV. In case of the $b\bar{b}H$ production mode, the $\pm(\text{QCD scale} + \text{PDF} + \alpha_S)$ % uncertainty is given [73, 74].

Production mode	Production mechanism	Cross-section [pb]
ggF	$pp \to H$	$48.52^{+3.2\,\%}_{-3.2\,\%}$
VBF	$pp \to qqH$	$3.78^{+2.1\,\%}_{-2.1\,\%}$
VH	$pp \to W^* \to WH$	$1.37^{+1.9\,\%}_{-1.9\,\%}$
	$pp \to Z^* \to ZH$	$0.88^{+1.6\,\%}_{-1.6\,\%}$
$t\bar{t}H$	$pp \to t\bar{t}H$	$0.51^{+3.6\,\%}_{-3.6\,\%}$
$b\bar{b}H$	$pp \to b\bar{b}H$	$0.49^{+20.1\,\%}_{-23.9\,\%}$

dominant, this production mode also provides a clear signature in the final state: the direction of movement of the incoming quarks is only slightly affected by radiation of W or Z bosons, resulting in their detection as forward and backward final state jets with a large difference in rapidity [65]. The cross-section for the VBF process is about one order of magnitude smaller than the cross-section from ggF.

VH A quark–antiquark annihilation into a virtual weak vector boson V ($V = W, Z$) and the subsequent radiation of a Higgs boson $q\bar{q} \to V^* \to VH$ is referred to as the VH production channel. The associate production of a Higgs boson with a W boson has an about 50 % higher cross-section than the associate production with a Z boson.

$t\bar{t}H/b\bar{b}H$ The production modes with cross-sections of about two orders of magnitude smaller than the cross-section for the ggF process is the associate production with top or bottom quarks abbreviated with $t\bar{t}H$ or $b\bar{b}H$, respectively. Two gluons decay each into a heavy quark–antiquark pair, where two subsequently annihilate into a Higgs boson while the other two hadronise. Due to the high third generation quark masses a high invariant mass at the collision is necessary for this production mode, which explains the low values of the cross-sections.
Figure 3.4 shows the cross-sections of the main Higgs boson production mechanisms at the LHC for different Higgs boson masses and centre-of-mass energies.

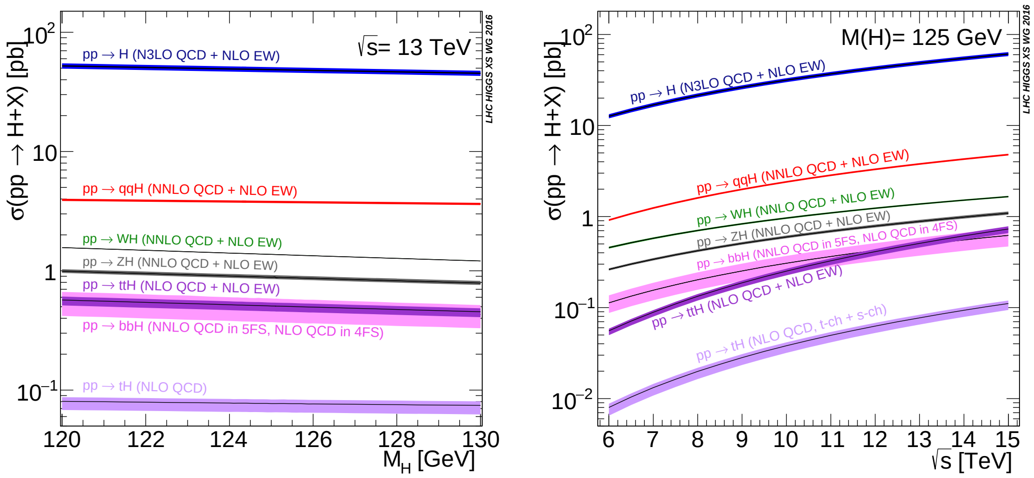

(a) (b)

Figure 3.4: The production cross-section of the SM Higgs boson is shown on a logarithmic axis (a) at a centre-of-mass energy of $\sqrt{s} = 13\,\text{TeV}$ for Higgs boson masses M_H between 120 GeV and 130 GeV and (b) for a Higgs boson mass of $m_H = 125\,\text{GeV}$ and centre-of-mass energies between 6 TeV and 15 TeV for the main production modes (top to bottom): gluon–gluon fusion (blue), vector-boson fusion (red), associated production with W and Z bosons (green) and associated production with heavy third generation quarks (magenta) [52, 76].

3.2.2 Decay of the Higgs boson

The Higgs boson is a short-lived particle with a total decay width of $\Gamma_H = \left(4.1^{+0.60\,\%}_{-0.61\,\%}\right)\text{MeV}$ with an uncertainty related to the variation of the strong coupling constant [77]. Therefore, the Higgs boson immediately decays inside the detector and is reconstructed via its decay products. Because of the Higgs boson coupling being proportional to the mass of the corresponding particle, it decays preferably to the heaviest state allowed by phase space [75], e. g. into a pair of bottom quarks with a probability of 58 % followed by the decay into $W^{\pm}$ bosons with 22 %. The main decays channels with respective branching ratios are displayed in Table 3.2, where the branching ratio is defined as the ratio of the decay width of a particular decay mode and the total decay width. Figure 3.5 shows the branching ratios as a function of the Higgs boson mass between 120 GeV and 130 GeV. Decays into massless gluons and photons with a probability of 8 % and 0.2 %, respectively, take place by means of an intermediate heavy quark loop. Since the photon interacts electromagnetically, $W^{\pm}$ boson loops additionally participate in the $\gamma\gamma$ decay mode.
Despite having the highest branching ratio, Higgs boson decays into a pair of bottom quarks are difficult to reconstruct in the large background of $b\bar{b}$-events. Leptons as final state particles,

Table 3.2: Branching ratios for the main decay channels given with respect to the total decay width of $\Gamma_H = 4.1\,\text{MeV}$ for a $m_H = 125.09\,\text{GeV}$ Higgs boson [77].

Decay channel	$b\bar{b}$	WW^*	gg	$\tau^+\tau^-$	$c\bar{c}$	ZZ^*	$\gamma\gamma$	$Z\gamma^*$
Branching ratio [%]	58.09	21.52	8.180	6.256	2.884	2.641	0.2270	0.1541

on the other hand, provide a clear signature. Therefore, Higgs boson decays into gauge bosons with subsequent leptonic decays play a significant role in LHC Higgs boson studies. Together with $H \to \gamma\gamma$, the leptonic decays $H \to WW \to \ell\nu\ell\nu$ and $H \to ZZ^* \to 4\ell$ ($\ell = e, \mu$) contributed to the Higgs boson discovery [5, 6]. Even though only about 3 % of all Higgs bosons decay into a pair of Z bosons and only less than 1 % into the fully leptonic final state, due to its clear experimental signature, the $H \to ZZ^* \to 4\ell$ channel is an important Higgs boson measurement channel at the LHC. In this thesis the Higgs boson is reconstructed via the four-lepton final state, which will be introduced in Section 4.

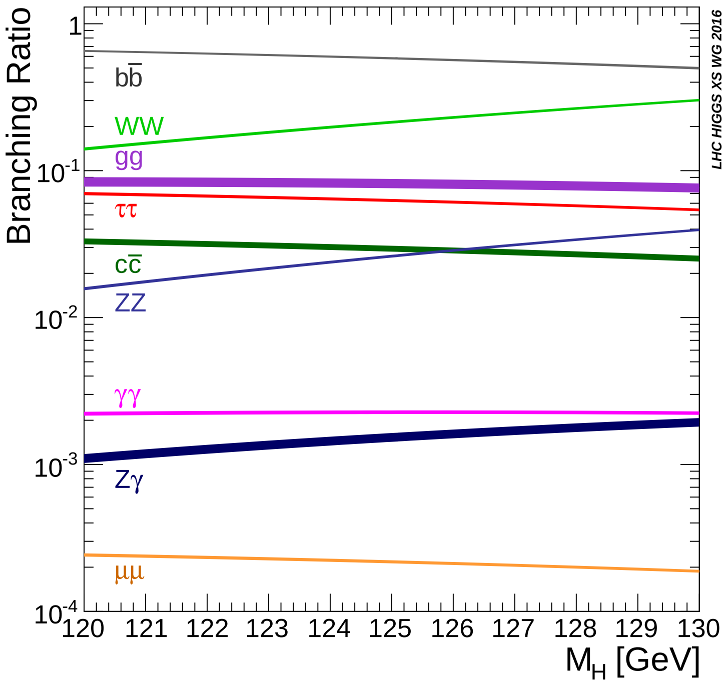

Figure 3.5: Branching ratios for the main decay channels of the Higgs boson as a function of its mass m_H in the range between 120 GeV and 130 GeV [77].

3.3 Physics beyond the Standard Model

The discovery of the Higgs boson in 2012 by the ATLAS and CMS Collaborations [5, 6] marked the SM a complete and self-consistent theory. Despite its ability to successfully predict and describe particle physics phenomena with extremely high precision, there are observations in nature that cannot be explained by the SM, hinting at BSM physics.

3.3.1 Motivation for physics beyond the Standard Model research

The hierarchy problem [78] addresses the vast difference in the numerical values of the weak force and gravity. In the context of naturalness the question leads to the smallness of the Higgs boson mass and why it appears to be unaffected by large radiative corrections [79, 80]. A strong evidence for Dark Matter (DM) comes from astrophysical observations of its gravitational effects at large distance scales [81, 82]. Albeit DM is assumed to be ubiquitous in the universe, no experimentally confirmed theory of its origin is present, thus calling for BSM physics. The most prominent research assumes DM to be some kind of *weakly interacting massive particle* (WIMP).
Prominent solutions to these two problems make often use of a highly elegant and phenomenologically appealing extension of the SM called *Supersymmetry* (SUSY). It provides a supersymmetric fermion as a (SUSY) transformation partner for each boson and vice versa [83–88]. In terms of the addition of new particles, the simplest supersymmetric extension of the SM is realised within the Minimal Supersymmetric Standard Model (MSSM). Additionally, it extends the Higgs boson sector by requiring two complex Higgs boson doublets [89, 90].
The term cosmic baryon asymmetry refers to the imbalance of matter and antimatter in our universe. The Big Bang should have produced particles and antiparticles in equal amounts. The observed asymmetry cannot be explained by the SM and leads to hypotheses beyond the SM [91], trying to find explanations for *baryogenesis*. Among the three necessary conditions to produce matter and antimatter at different rates, proposed by Sakharov [92] originally in 1967, the violation of the $\mathcal{CP}$-symmetry can be found. Since the $\mathcal{CP}$-violation in the SM is not sufficient to explain the observed asymmetry, theories addressing baryogenesis often seek additional sources of $\mathcal{CP}$-violation.

3.3.2 $\mathcal{CP}$-violation in the Higgs sector

The SM predicts the Higgs boson to have spin $J = 0$ and to conserve $\mathcal{CP}$-symmetry with even eigenvalue. Separate charge conjugation ($\mathcal{C}$) and parity transformation ($\mathcal{P}$) eigenvalues are predicted to be even as well. Assuming charge conservation, the $\mathcal{C} = +1$ nature of the Higgs boson is confirmed by the observation of the decay into two photons, since for each photon $\mathcal{C} = -1$ and the charge conjugation is a multiplicative quantum number [52, Chapter 11]. The

SM prediction $J^{\mathcal{CP}} = 0^+$ has been tested by ATLAS and CMS by comparing with different $J^{\mathcal{CP}}$ hypotheses, varying the spin ($J = 0, 1, 2$) or the parity eigenvalue $\mathcal{CP} = \pm 1$ of the resonance. The SM prediction is so far confirmed, alternative $J^{\mathcal{CP}}$ hypotheses are excluded at more than 99.9 % confidence level [15, 93, 94]. While the pure $\mathcal{CP}$-odd state $J^{\mathcal{CP}} = 0^-$ is excluded, a mixed state, where the Higgs boson is a superposition of $\mathcal{CP}$-even and $\mathcal{CP}$-odd eigenstates is still allowed. Such mixtures would result in $\mathcal{CP}$-violation, providing direct evidence for BSM physics [95].

The $\mathcal{CP}$-properties of a particle can be probed by analysing its coupling behaviour to other SM particles. The coupling of the Higgs boson to other elementary particles is determined by the tensor structure of the coupling in the interaction vertex. Non-vanishing $\mathcal{CP}$-odd contributions to the $\mathcal{CP}$-even SM prediction tensor structure of the Higgs boson coupling is called an anomalous coupling contribution and leads to the violation of $\mathcal{CP}$-invariance [16]. $\mathcal{CP}$-eigenvalue measurements and propositions of constraining Higgs boson $\mathcal{CP}$-properties often rely on the coupling to weak vector bosons. However, while unsuppressed (tree-level) couplings between the Higgs boson and the massive vector bosons exist for the $\mathcal{CP}$-even component, $\mathcal{CP}$-odd contributions enter with a higher-order operator making it difficult to probe these contributions. A better study of $\mathcal{CP}$-odd admixtures is possible in couplings between the Higgs boson and charged fermions or massless gauge bosons. In these cases the $\mathcal{CP}$-even and $\mathcal{CP}$-odd couplings are induced at the same order, namely at tree-level and at loop-level, respectively [16, 95].

In this thesis $\mathcal{CP}$-violation is searched for by means of studying the tensor structure of the coupling between the Higgs boson and gluons. BSM physics cannot only be explored via the hunt for new resonances, but also by searching for indirect effects on the couplings of the Higgs boson to SM particles. Additionally to the aforementioned induction of anomalous coupling contributions at the same order, loop processes are an eminent source of new particles. Both aspects take effect in the ggF production mode of the Higgs boson.

3.4 Effective gluon–gluon–Higgs boson coupling

3.4.1 Sensitivity of gluon–gluon fusion to BSM physics

Despite being a loop-induced process, a high gluon density inside the proton makes ggF the most dominant Higgs boson production mode by an order of magnitude higher cross-section (see Figure 3.4 and Table 3.1). Having two gluons in the initial state results in an enhanced tendency of producing further QCD radiation and next-to-leading order (NLO) QCD corrections to the inclusive ggF cross-section are known to be large [96, 97]. Defining the K-factor as $\sigma_{\text{NLO}}/\sigma_{\text{LO}}$, where all quantities are consistently evaluated with the respective accuracy, it has a K-factor of about 1.6 [98]. Since the Feynman diagram of the ggF mode already contains a loop at leading order (LO), calculations in higher orders in perturbation theory are a particularly challenging task [65]. The most recent results provide corrections up to next-to-next-to-next-to-leading order (N^3LO) [99, 100]. The computation of corrections

beyond LO can be greatly simplified by treating the Hgg interaction as point-like in the infinite top mass limit $m_t \rightarrow \infty$.
Real emission corrections to the ggF production mode can lead to additional jets in the final state, whose distributions carry information about gluon properties in the ggF production mode. Two-jet final state events, i. e. $pp \rightarrow H + 2j$ events (Figure 3.6), provide fairly well opportunities to probe for BSM physics. This can be done using kinematic distributions of observables known to preserve $\mathcal{CP}$-properties, such as the angular difference between the two tagging jets [95]. Beside shape information, the total production rate is also affected by the presence of BSM coupling parameters and must be considered especially in categories without shape information. Since the most ggF events come without additional jets, rate information currently is indispensable.

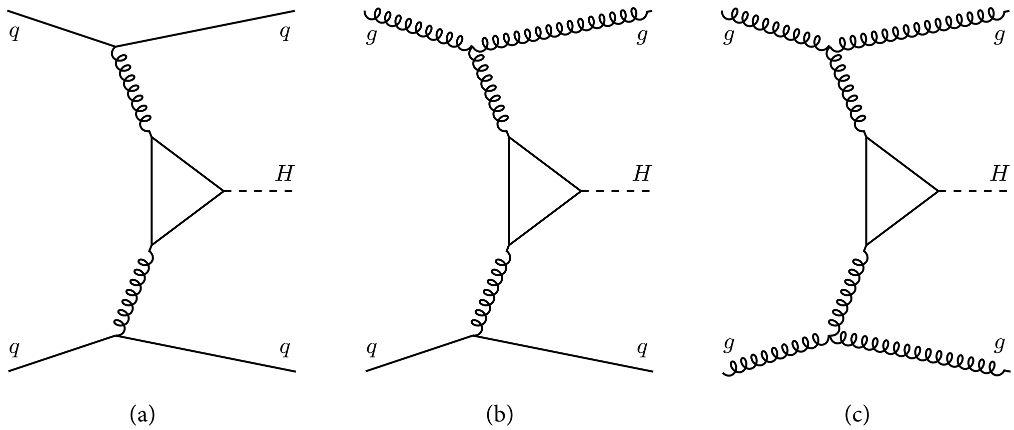

Figure 3.6: Feynman diagrams of the real emission correction processes contributing at orders of $\mathcal{O}\left(\alpha_s^4\right)$ to a final state with two jets. These are scatterings of (a) two (not necessarily same flavoured) quarks, (b) one gluon and one quark and (c) two gluons [72].

The crucial demand for the infinite top mass limit to serve as a good approximation is the transverse momentum of final state objects, since the $m_t \rightarrow \infty$ limit seems to break down for Higgs boson or jet $p_\mathrm{T} > 200\,\mathrm{GeV}$ [97, 101–103]. The work in this thesis accounts for this fact by applying corresponding event cuts.

3.4.2 The Higgs Characterisation model

The possibility for the Higgs boson not to be a pure $\mathcal{CP}$-even state as predicted by the SM, but rather to have BSM $\mathcal{CP}$-even and $\mathcal{CP}$-odd admixtures in the tensor structure of the coupling to gluons can be studied by using the Higgs Characterisation (HC) model. It utilises an effective field theory (EFT) approach, assuming new resonances entering only at energy scales larger than a certain cut-off value Λ, which is set to 1 TeV in this thesis. This assumption

is in accordance with the experimental results obtained at the LHC as well as in previous collider experiments, not showing any evidence for new physics at lower energy scales. It can be shown, that such theories are renormalisable and prove to be a viable approach for the problem of new-particle characterisation [17]. Since the top quark loop and the interactions in the production vertex cannot be resolved at energies below Λ, the Hgg interaction is treated as point-like and described in terms of effective couplings.
The expression for the Lagrangian of the HC model for the relevant spin–0 Higgs boson state can be written as

$$\mathscr{L}_{\mathrm{HC},0} = \mathscr{L}_{\mathrm{SM}-H} + \mathscr{L}_0 \ ,$$

with the first term on the right hand side $\mathscr{L}_{\mathrm{SM}-H}$ describing the SM Lagrangian without the Higgs boson whereas the second term $\mathscr{L}_0$ containing the kinetic and interaction terms of the relevant Higgs boson state [17]. Using the abbreviations

$$\mathrm{c}_\alpha \equiv \cos(\alpha) \quad \text{and} \quad \mathrm{s}_\alpha \equiv \sin(\alpha)$$

to account for possible $\mathcal{CP}$-mixing of 0^+ and 0^- states via the mixing angle α, the interaction between gluons with a Higgs field X_0 can be described by the Lagrangian

$$\mathscr{L}_0^V = -\frac{1}{4}\left[\mathrm{c}_\alpha \kappa_{Hgg} g_{Hgg} G^a_{\mu\nu} G^{a,\mu\nu} + \mathrm{s}_\alpha \kappa_{Agg} g_{Agg} G^a_{\mu\nu} \widetilde{G}^{a,\mu\nu}\right] X_0 \ , \tag{3.7}$$

with defining the reduced field strength tensor as

$$G^a_{\mu\nu} = \partial_\mu G^a_\nu - \partial_\nu G^a_\mu + g_\mathrm{s} f^{abc} G^b_\mu G^c_\nu \ ,$$

and the dual tensor as

$$\widetilde{G}^a_{\mu\nu} = \frac{1}{2}\varepsilon_{\mu\nu\rho\sigma} G^{a,\rho\sigma} \ .$$

The terms of the Lagrangian (Eq. 3.7) are grouped according to $\mathcal{CP}$-even and $\mathcal{CP}$-odd nature of the couplings, denoted by an H or A subscript, respectively. The first term transforms under $\mathcal{CP}$-symmetry with an even eigenvalue, whereas the second one does so with an odd eigenvalue. The couplings g_{Hgg} and g_{Agg} are defined in a way, such that in the $\mathcal{CP}$-even case the SM Higgs boson is reproduced and in a purely $\mathcal{CP}$-odd case, a pseudo-scalar Higgs boson is obtained [17]. The $\mathcal{CP}$-even coupling parameter κ_{Hgg} describes the coupling between the Higgs boson and the pair of gluons in accordance to the SM, while a value $\kappa_{Agg} \neq 0$ accounts for anomalous $\mathcal{CP}$-odd contribution to the gluon–gluon–Higgs boson coupling

Table 3.3: Exemplary configurations of the $\mathcal{CP}$-even and $\mathcal{CP}$-odd HC model coupling parameters $c_\alpha \kappa_{Hgg}$ and $s_\alpha \kappa_{Agg}$, respectively, and the mixing angle α leading to different Higgs boson states within the ggF production mode. The $\mathcal{CP}$-violating mixed state 0^{mix} is obtained for $\kappa_{Agg} \neq 0$ and $\alpha \neq 0$, $\alpha \neq \pi/2$.

$J^{\mathcal{CP}}$	Model	Parameter values		
		$c_\alpha \kappa_{Hgg}$	$s_\alpha \kappa_{Agg}$	α
0^+	SM Higgs boson	1	0	0
0^{mix}	BSM spin–0 $\mathcal{CP}$-mixed	1	0.6	$\pi/4$
0^-	BSM spin–0 $\mathcal{CP}$-odd	0	1	$\pi/2$

with a coupling strength proportional to $s_\alpha \kappa_{Agg}$. Table 3.3 shows exemplary scenarios for different parameter configurations resulting in certain Higgs boson states. The SM Higgs boson is obtained for a $\mathcal{CP}$-odd coupling strength parameter value $s_\alpha \kappa_{Agg} = 0$ and a $\mathcal{CP}$-even coupling strength parameter value $c_\alpha \kappa_{Hgg} = 1$. A purely $\mathcal{CP}$-odd BSM Higgs boson state corresponds to $s_\alpha \kappa_{Agg} = 1$ and $c_\alpha \kappa_{Hgg} = 0$. $\mathcal{CP}$-odd admixtures to the Hgg interaction vertex are realised by BSM spin–0 $\mathcal{CP}$-mixed states where $c_\alpha \kappa_{Hgg} = 1$ and $s_\alpha \kappa_{Agg} \neq 0$.
The Lagrangian (Eq. 3.7) is part of a more general expression taking into account the couplings of the Higgs boson to weak vector bosons and photons. However, since this work focusses on anomalous coupling contributions solely in the Hgg vertex, the coupling to Z bosons in the $H \to ZZ^* \to 4\ell$ decay channel (see Chapter 4) utilised for this work, is assumed to be in accordance to the SM. Thus, equation (Eq. 3.7) contains only the relevant term with the parameter of interest in combination with the mixing angle $s_\alpha \kappa_{Agg}$.

3.5 Latest status of Higgs boson properties measurements

In the following a brief overview is given of the current results from measurements that have been performed by ATLAS and CMS based on data sets obtained during LHC Run 1 and Run 2 in the time periods 2011–2012 and 2015–2017, respectively. Measurements of the Higgs boson mass, its coupling to SM particles and its spin and $\mathcal{CP}$-properties have been performed at centre-of-mass energies $\sqrt{s}$ of 7 TeV, 8 TeV and 13 TeV and results of high accuracy are available. The Higgs boson width as well as its self-coupling are currently not yet experimentally accessible. In this regard merely upper limits and constraints can be set [52, 104].
All results are within the SM predictions and no deviations have been observed so far.

3.5.1 Mass and couplings measurements

The mass of the Higgs boson is given by the expectation value v of the Higgs field and the Higgs self-coupling parameter λ as $m_H = \sqrt{2\lambda}v$. While the expectation value is fixed by means of the Fermi coupling G_F as $v = (\sqrt{2}G_F)^{-1/2}$, which can be experimentally extracted from muon decays [105], the self-coupling λ occurring in the Higgs potential (see Eq. 3.5) has no prediction within the SM [52, Chapter 11]. Therefore the Higgs boson mass is a free parameter in the SM and has to be measured. The mass is measured in the $H \to \gamma\gamma$ and $H \to ZZ^* \to 4\ell$ decay channels, which allow a full reconstruction of the invariant mass of the Higgs boson and have the best mass resolution. Figure 3.7 summarises the current results featuring individual and combined ATLAS and CMS Run 1 measurements [106], preliminary Run 2 measurements performed by ATLAS in the above mentioned channels [107] and by CMS in the 4ℓ channel [108]. The combined Run 1 result[2] with statistical and systematic uncertainties is given as $m_H = 125.09 \pm 0.21$ (stat.) $\pm$ 0.11 (syst.) GeV. Once the Higgs boson mass is determined, its couplings to other particles are fully predicted by the SM.
The coupling of the Higgs boson to SM particles is set by the masses of the particles, thus any deviations from the expected couplings are a hint at BSM physics. Higgs boson couplings are studied by measuring the product of production cross-section and branching ratio of the decay. Results for several production and decay mode combinations are shown in Figure 3.8. The results of the combined measurements from ATLAS and CMS using LHC Run 1 data are all within experimental and theoretical uncertainties and the observed data are consistent with a SM Higgs boson expectation [52, Chapter 11][109].
The couplings of the Higgs boson to vector bosons have been discovered in Run 1. The improved integrated luminosity of Run 2 promises progress in the study of couplings to fermions. The decay into a pair of tau leptons $H \to \tau^+\tau^-$ has been discovered by CMS [110] and an associate production with a top quark pair $t\bar{t}H$ by both, ATLAS [111] and CMS [112] and the decay into a pair of bottom quarks $H \to b\bar{b}$ is was recently observed by both collaborations [113].

3.5.2 Spin and parity measurements

Probing the spin and the behaviour under $\mathcal{CP}$-transformation is essential in unveiling the coupling properties of the Higgs boson and their agreement with SM predictions [52, Chapter 11].

Fixed $J^{\mathcal{CP}}$ hypothesis tests

The observation of the Higgs boson in the $H \to \gamma\gamma$ decay channel has important implications according to the Landau–Yang theorem [114, 115]: the spin–1 hypothesis is excluded and the observed particle is restricted to have either spin–0 or spin–2. Because the theorem is

[2] The value for the combined measurement (blue) given in Figure 3.7 states the systematic uncertainty erroneously as ±0.15 GeV instead of ±0.11 GeV, as given in the original source [106].

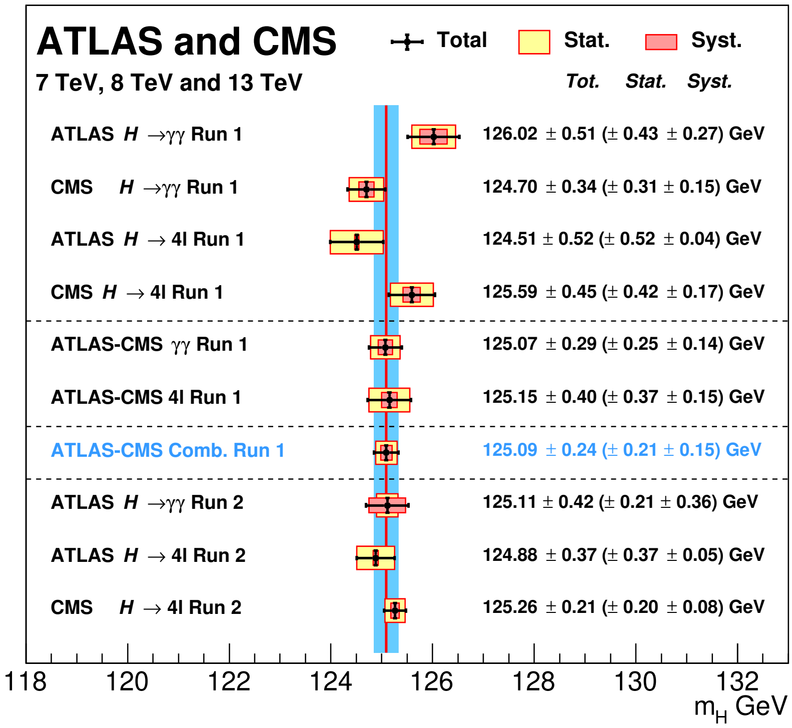

Figure 3.7: Summary of the ATLAS and CMS mass measurement results in the $H \to \gamma\gamma$ and the $H \to ZZ^* \to 4\ell$ decay channels. Results for Run 1 individual and combined analyses as well as individual preliminary Run 2 analyses are shown [52].

only applicable for a direct decay into a pair of photons, spin–1 hypotheses are still tested to account for possible decays into scalar bosons which then subsequently decay into two very collimated pairs of photons [52, Chapter 11].

Scenarios with fixed spin and parity have been probed in decays to $\gamma\gamma$ or in $H \to WW^* \to \ell\nu\ell\nu$ and $H \to ZZ^* \to 4\ell$ decays. The data are compatible with the SM 0^+ hypothesis and alternative $J^{\mathcal{CP}}$ hypotheses are excluded in favour of the SM hypothesis. ATLAS [14] and CMS [15] exclude a Higgs boson with a pseudo-scalar nature (0^-) at CL_S levels of 98 % and 99.8 %, respectively. Figure 3.9 shows a summary of several $J^{\mathcal{CP}}$ hypotheses studies performed by ATLAS. The studies performed by CMS involve a larger number of models, but the main conclusions are similar and fully consistent [52, Chapter 11].

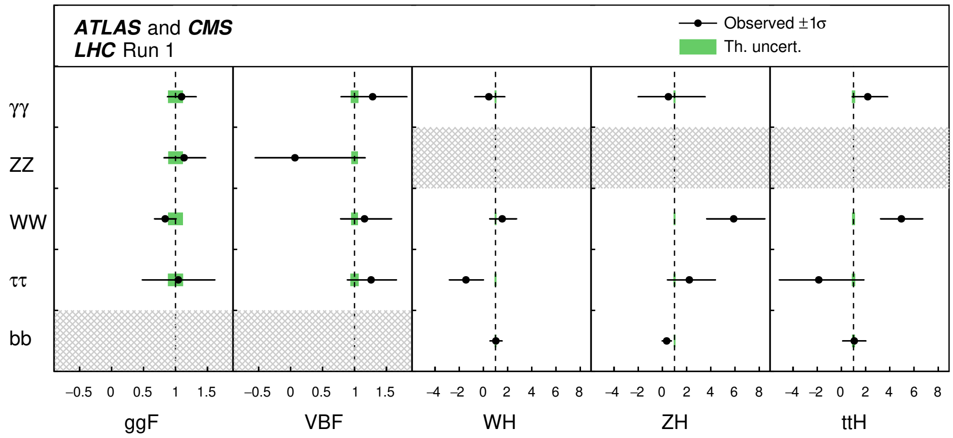

Figure 3.8: Combined measurements of the signal strength, which is the event yield for a specific Higgs boson production and decay, normalised to the SM expectation for a Higgs boson mass m_H = 125.09 GeV for different combinations of one of the main five Higgs boson production modes and one of the main five decay channels from ATLAS and CMS using LHC Run 1 data. For the hatched combinations no confidence interval could be determined due to a low amount of data [52].

Measurement of the Higgs boson coupling tensor structure to vector bosons

At ATLAS, the tensor structure of the Higgs bosons couplings to vector bosons and gluons is studied [18] within the effective field theory approach of the HC model (Section 3.4.2). Aside from the conclusive results from fixed $J^{\mathcal{CP}}$ tests, anomalous $\mathcal{CP}$-even and $\mathcal{CP}$-odd admixtures to the primarily $\mathcal{CP}$-even state of the Higgs boson are tested under the assumption of a spin–0 Higgs boson.
The tensor structure of the Higgs boson coupling to weak vector bosons has been studied by ATLAS [18] and CMS [15] with LHC Run 2 and fully reconstructed LHC Run 1 datasets, respectively. The obtained results are compatible with the SM predictions within 2σ.
The $\mathcal{CP}$-odd BSM Higgs coupling to gluons has been probed by ATLAS [18] by measuring the coupling strength parameter[3] κ_{Agg} while assuming all other BSM parameters to be 0 and fixing the SM coupling $\kappa_{Hgg} = 1$. Furthermore, changes in the Higgs sector from BSM effects are assumed not to affect the SM background. Figure 3.10 shows the measurement results statistically interpreted using likelihood tests [94]. The observed distribution has a best fit value $\hat{\kappa}_{Agg} = \pm 0.43$ and an observed 95 % confidence level interval $[-0.68,\ 0.68]$.

[3] The notation used in the original reference differs slightly by the one introduced in Section 3.4.2. Contrary to this work, there κ_{Agg} is proportional to the $\mathcal{CP}$-odd coupling strength.

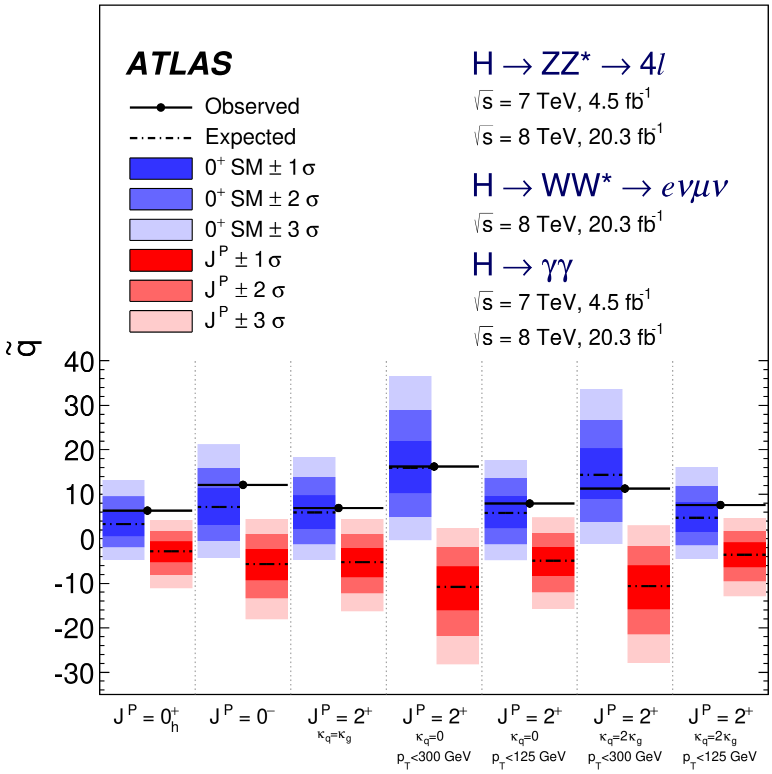

Figure 3.9: Distributions of the test statistic for the SM hypothesis $J^{\mathcal{CP}} = 0^+$ for spin and parity of the Higgs boson as observed in Run 1 data (blue) together with several alternative spin and parity hypotheses (red) studied in the decay channels $H \to ZZ^* \to 4\ell, H \to WW^* \to e\nu\mu\nu$ and $H \to \gamma\gamma$ with ATLAS [52].

No sensitivity to the sign of the BSM coupling parameter can be provided by the event yields measured in the reconstruction categories.
A detailed analysis description including best-fit values and exclusion limits can be found in [18].

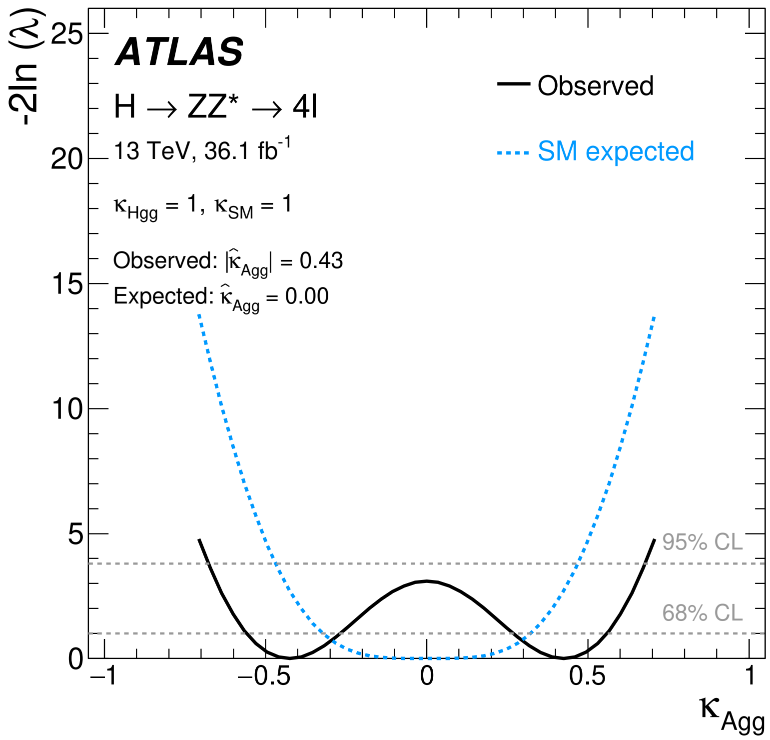

Figure 3.10: Observed (solid black line) and according to SM predictions expected (dashed blue line) negative log-likelihood scans for the BSM $\mathcal{CP}$-odd contribution to the tensor coupling structure for the Higgs boson–gluon interaction obtained from 36.1 fb^{-1} of data at $\sqrt{s}$ = 13 TeV, recorded with the ATLAS detector. Horizontal dashed lines indicate the values of the profile likelihood ratio corresponding to the 68 % and 95 % confidence level intervals [18, 94].

4

The $H \to ZZ^* \to 4\ell$ analysis channel

Even though the Higgs boson with a mass of $m_H = 125.09$ GeV decays into a pair of Z bosons with a branching ratio of only about 2.6 % (see Table 3.2), the decay channel $H \to ZZ^* \to 4\ell$ provides a very good sensitivity for the study of the Higgs boson properties due to a very low background contribution. This decay channel is employed in this thesis for the measurement of the tensor structure of the Higgs boson coupling to gluons. The selection of the $H \to ZZ^* \to 4\ell$ event candidates will therefore briefly be described in this chapter. Since the mass of the Higgs boson is below the threshold of $2 \cdot m_Z \approx 180$ GeV for the resonant ZZ production, one of the two Z bosons is produced off-shell, i. e. as a virtual particle, denoted by Z^*. The tree-level Feynman diagram for the $H \to ZZ^* \to 4\ell$ process is shown in Figure 4.1.

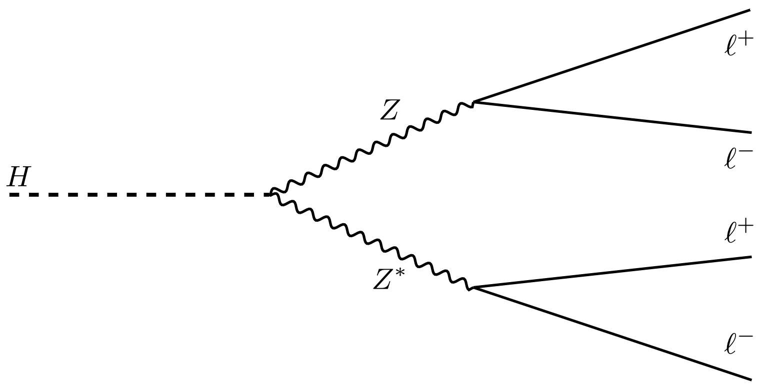

Figure 4.1: Tree-level Feynman diagram for the Higgs boson decay into one on-shell and one off-shell (Z^*) Z boson, which subsequently both decay into a pair of oppositely charged leptons $\ell^+\ell^-$, where $\ell \equiv e, \mu$ [72].

The Z boson decays predominantly hadronically with a branching ratio of about 70 %, but such decays are experimentally difficult to reconstruct due to the large QCD multijet background. The decay into an oppositely charged lepton pair $\ell^+\ell^-$ ($\ell \equiv e, \mu$) has a branching ratio of only about 3.4 % [60], but provides a clear decay signature in the detector. The dominant background processes with the same final state are the $ZZ^{(*)}$production, the $t\bar{t}$ production and the Z + jets production. The latter two processes can be strongly suppressed by requiring that leptons are isolated, i. e. that there is a low energy deposition around each lepton. The high signal-to-background ratio and additionally the ability to fully reconstruct the four-momenta of all decay products provide a very good sensitivity to $H \rightarrow ZZ^* \rightarrow 4\ell$ events.

In this chapter the used channel is presented. The simulated Monte Carlo (MC) samples used for the study of the event selection in this channel are briefly introduced in Section 4.1. The $H \rightarrow ZZ^* \rightarrow 4\ell$ event selection leading to Higgs boson candidates for the study of the coupling tensor structure is described in Section 4.2, followed by a discussion of relevant background contributions in Section 4.3. In Section 4.4, the event yields expected after the event selection is summarised.

4.1 Monte Carlo simulation

In order to study the $H \rightarrow ZZ^* \rightarrow 4\ell$ selection, several MC samples with a detailed simulation of the ATLAS detector are employed. The samples are provided by the official central ATLAS production system. No LHC proton–proton collision data is used in this thesis. All simulated events are generated at a centre-of-mass energy of $\sqrt{s} = 13$ TeV.

The Higgs boson events are generated separately for the dominant ggF, VBF and VH production modes using the event generator Powheg-Box v2 [116, 117]. The official samples are all assuming the SM structure of the Higgs boson couplings. The VBF and VH production modes are calculated up to NLO precision in the matrix element calculations. The ggF Higgs boson production sample is generated at next-to-next-to-leading order (NNLO) QCD precision using the Powheg NNLOPS method [118]. For the simulation of the decay and the parton showering Pythia8 [119] has been used. EvtGen [120] was used to account for properties from bottom and charm hadron decays.
The $ZZ^{(*)}$continuum background contribution from quark–antiquark annihilation (see Section 4.3) was simulated using Sherpa 2.2.2 [121] at NLO accuracy for final states with up to one jet and at LO accuracy for two and three final state jets. The gluon-induced $ZZ^{(*)}$continuum background is modelled at LO with gg2VV [122].
An overview of the MC sets used in this work is given in Appendix A.

4.2 Event selection

The $H \to ZZ^* \to 4\ell$ analysis begins with a pre-selection guaranteeing good data quality. Here it is ensured that all detector components have been functioning properly during the data taking. Furthermore, the events are required to have at least one vertex containing at least two associated $p_T^{\text{track}} > 400$ MeV tracks.
The four-lepton events are selected with single-lepton, dilepton and trilepton triggers, which accept electrons (muons), if certain identification criteria and E_T (p_T) thresholds are fulfilled [123].
These leptons are either electrons or muons and satisfy the 'loose' identification criteria (see Section 2.3.2 and Section 2.3.3). At least two pairs of oppositely charged leptons must be present in the selected events. The lepton quadruplets are classified according to their flavour content into 4μ, $2e2\mu$, $2\mu2e$ and $4e$ final state Higgs boson candidates. Further selection criteria are applied by requiring the transverse energy (transverse momentum) and the pseudo-rapidity of the electron (muon) to be $E_T > 7$ GeV ($p_T > 5$ GeV) and $|\Delta\eta| < 2.47$ ($|\Delta\eta| < 2.7$). Calorimeter tagged muons are required to have $p_T > 15$ GeV in the pseudo-rapidity range $|\Delta\eta| < 0.1$ in order to account for the MS acceptance gap [34]. The requirement for the longitudinal impact parameter $z_0 \cdot \sin(\theta) \leq 0.5$ mm constrains the leptons to the primary vertex and also reduces the contribution from hadronised b-quark background processes [123]. By narrowing the absolute value of the muon transverse impact parameter $|d_0| < 1$ mm, background contribution from cosmic-ray muons can be essentially eliminated.
Each final state must have at least one lepton quadruplet consisting of two pairs of same-flavour opposite-charge leptons. In each event, the three leptons with the highest transverse momentum p_T must have p_T greater than 20 GeV, 15 GeV and 10 GeV, respectively. The lepton pair with an invariant mass m_{12} (m_{34}) closest (second closest) to the mass of the Z boson $m_Z = 91\,187.6$ MeV is referred to as the leading (sub-leading) dilepton. The four possible final state decay channels 4μ, $2e2\mu$, $2\mu2e$ and $4e$ are studied separately.
The dilepton masses have to lie in appropriate mass ranges to increase the sensitivity: $50\,\text{GeV} \leq m_{12} \leq 106\,\text{GeV}$ and $m_{Z2,\text{min}} \leq m_{34} \leq 115\,\text{GeV}$. The threshold value $m_{Z2,\text{min}}$ is defined to be 12 GeV for an invariant mass of the lepton quadruplet $m_{4\ell} \leq 140$ GeV, rising linearly to a value of $m_{Z2,\text{min}} = 50$ GeV for invariant lepton quadruplet masses up to 190 GeV and remaining at 50 GeV for values of $m_{4\ell}$ above 190 GeV. To ensure an angular separation between the leptons, every two same-flavour (opposite-flavour) leptons are required to satisfy $\Delta R \geq 0.1$ (0.2), where

$$\Delta R = \sqrt{(\Delta\eta)^2 + (\Delta\phi)^2}\,.$$

An e^+e^- or $\mu^+\mu^-$ pair from the decay of a J/ψ meson with a mass of approximately 3 GeV [60] may be incorrectly attributed to originate from two Z boson decays. In order to exclude background from J/ψ meson decays, a J/ψ veto is imposed on lepton pairs in the decay

channels $4e$ and 4μ, requiring that the invariant dilepton mass be $m_{\ell\ell} \geq 5\,\text{GeV}$.
The final state jets are required to have transverse momenta $p_{\text{T}}^{\text{jet}} \geq 30\,\text{GeV}$ and jet pseudo-rapidities $|\eta| < 4.5$. An angular separation between jets and leptons is realised by invoking a jet–lepton-overlap removal, which discards the jets with an angular distance of $\Delta R < 0.2$ to electrons and $\Delta R < 0.1$ to muons.
The invariant lepton quadruplet mass $m_{4\ell}$ is constrained to a mass window of $118\,\text{GeV} \leq m_{4\ell} < 129\,\text{GeV}$ around the measured Higgs boson mass [106]. The size of the window is determined by the detector resolution of the mass measurement. The treatment of the Hgg vertex as an effective point-like interaction is a valid approximation only for Higgs boson and jet transverse momenta p_{T}^{H} and $p_{\text{T}}^{\text{jet}}$, respectively, smaller than or of the order of the top quark mass [97, 103] (see Section 3.4.1). Therefore, the requirements $p_{\text{T}}^{H} \leq 200\,\text{GeV}$ and $p_{\text{T}}^{\text{jet}} \leq 200\,\text{GeV}$ are applied to each event.
Eventually the requirement for isolated leptons reduces the contributions from reducible background processes Z+jets and $t\bar{t}$. It is realised by constraining the track based isolation $I_{\ell}^{\text{track}} < 0.15$ with

$$I_e^{\text{track}} = \frac{\sum_i p_{\text{T},i}^{\text{track}}}{E_{\text{T}}^{e}} \quad \text{and} \quad I_\mu^{\text{track}} = \frac{\sum_i p_{\text{T},i}^{\text{track}}}{p_{\text{T}}^{\mu}}$$

for tracks within a cone of $\Delta R \leq 0.2$ (0.3) around the reconstructed electron (muon). Additionally calorimeter based isolation requirements with $\Delta R \leq 0.2$ are imposed

$$I_e^{\text{calo}} = \frac{\sum_i E_{\text{T},i}^{\text{cluster}}}{E_{\text{T}}^{e}} < 0.2 \quad \text{and} \quad I_\mu^{\text{calo}} = \frac{\sum_i E_{\text{T},i}^{\text{cluster}}}{p_{\text{T}}^{\mu}} < 0.3\,.$$

By requiring for each quadruplet electron (muon) the transverse impact parameter significance $\left|d_0/\sigma_{d_0}\right| < 5$ (3), with σ_{d_0} being the error of the d_0 measurement, background contributions from b- and c-hadron decays can be further reduced. The vertex selection is improved by demanding $\chi^2/N_{\text{dof}} < 6$ for 4μ and $\chi^2/N_{\text{dof}} < 9$ for all other final states, where χ^2 represents the quality of the fit of the four leptons to the vertex and N_{dof} the number of degrees of freedom. The lepton resolution is improved by taking energy losses due to final state radiation (FSR) into account. An additional Z boson mass constraint is applied to the dilepton from the on-shell Z boson candidate. The transverse momentum of the lepton is corrected by performing a kinematic fit to the Z boson line shape, improving the four-lepton invariant mass resolution [107, 124, 125]. An overview of the event selection requirements is given in Table 4.1.
The selected Higgs boson event candidates are categorised according to their jet multiplicities into four categories: *0-jet*, *1-jet*, *2-jet-sameHemi* and *2-jet-oppHemi*, where the latter two contain events with at least two final state jets. The 2-jet events are split according to the relative directions of the two jets in the detector. The *2-jet-sameHemi* (*2-jet-oppHemi*) category contains the two leading jets, which lie in the same (opposite) hemisphere, i. e. have a positive

Table 4.1: Event selection requirements applied within the $H \to ZZ^* \to 4\ell$ detector-level analysis [124].

Lepton and jet requirements	
Electrons	Loose identification, $E_T > 7$ GeV and $\|\eta\| < 2.47$ Longitudinal impact parameter $z_0 \cdot \sin(\theta) < 0.5$ mm
Muons	Loose identification, $p_T > 5$ GeV Combined muons (CB): $\|\eta\| < 2.5$ Segment-tagged muons (ST): $\|\eta\| < 0.1$ Calorimeter-tagged muons (CT): $15\,\text{GeV} < p_T < 100\,\text{GeV}$ and $\|\eta\| < 0.1$ Longitudinal and transverse impact parameter (CB, ST and CT only): $z_0 \cdot \sin(\theta) < 0.5$ mm and $\|d_0\| < 1$ mm Extrapolated muons (EM): $2.5 < \|\eta\| < 2.7$
Jets	Anti-k_t jets with distance parameter $R = 0.4$ $p_T > 30$ GeV and $\|\eta\| < 4.5$ Jet–electron(muon)–overlap removal $\Delta R > 0.2$ (0.1)
Event selection	
Quadruplet selection	Consists of two pairs of same-flavour opposite-charge leptons For three highest transverse momentum leptons: $p_T > 20, 15, 10$ GeV Leading dilepton invariant mass: $50\,\text{GeV} \leq m_{12} \leq 106\,\text{GeV}$ Sub-leading dilepton invariant mass: $m_{Z2,\text{min}} \leq m_{34} \leq 115\,\text{GeV}$ $\Delta R > 0.1$ (0.2) for same-flavour (opposite-flavour) leptons Same-flavour opposite-charge pairing $m_{\ell\ell} \geq 5$ GeV (J/ψ veto)
Lepton isolation	Electron track isolation ($\Delta R \leq 0.2$) $I_e^{\text{track}} < 0.15$ Muon track isolation ($\Delta R \leq 0.3$) $I_\mu^{\text{track}} < 0.15$ Electron calorimeter isolation ($\Delta R \leq 0.2$) $I_e^{\text{calo}} < 0.2$ Muon calorimeter isolation ($\Delta R \leq 0.2$) $I_\mu^{\text{calo}} < 0.3$ Impact parameter significance $\|d_0/\sigma_{d_0}\| < 5$ (3) for electrons (muons)
Vertex selection	$\chi^2/N_{\text{dof}} < 6$ for 4μ final state $\chi^2/N_{\text{dof}} < 9$ for $2e2\mu$, $2\mu2e$ and $4e$ final states

(negative) product of rapidities $y_1 \cdot y_2$. The motivation for this categorisation is the additional sensitivity to BSM $\mathcal{CP}$-odd coupling contributions, as described in the next chapter (see Section 5.3).

4.3 Background estimation

Events with four leptons in the final state not originating from the decay $H \rightarrow ZZ^* \rightarrow 4\ell$ are referred to as background processes and have to be taken into account for the final evaluation of the sensitivity to the BSM coupling contributions. Background is classified as reducible and irreducible. The former background processes have less than four leptons produced on particle-level, i. e. some of the leptons originate either from subsequent hadron decays or from misidentifications of jets as leptons due to limited detector performance. The main reducible background processes are Z + jets, $t\bar{t}$ and WZ production. The lowest-order Feynman diagrams of these processes are depicted in Figure 4.2.
The contribution of reducible background processes is estimated using a data-driven approach, employing dedicated signal-depleted control regions in data. Since the contribution of these backgrounds is minor, the reducible background is neglected in this thesis.
Processes with four particle-level leptons in the final state are referred to as irreducible background coming mainly from the non-resonant $ZZ^{(*)}$production. The lowest-order Feynman diagrams for this process are shown in Figure 4.3.
For annihilations in kinematic regions of the on-shell Higgs boson production, the main contributions are expected from the quark–antiquark annihilation in Figure 4.3(a). Annihilations to a Z boson resonance only produce events with a four-lepton invariant mass around the Z boson mass (Figure 4.3(b)). Non-resonant $ZZ^{(*)}$production via gluon–gluon fusion (Figure 4.3(c)) gives the smallest contribution, since it is a loop-induced process. The contribution of the irreducible $ZZ^{(*)}$background is estimated with dedicated MC simulations, described in Section 4.1.

4.4 Results of the $H \rightarrow ZZ^* \rightarrow 4\ell$ event selection

The luminosity expected to be reached at the end of Run 2 is 120 fb^{-1}. The expected number of events at this amount of data obtainable by applying the event selection as described before is summarised in Table 4.2.
The number of expected events is given in each category for each of the Higgs boson production modes ggF, VBF, ZH and WH. Contributions from $t\bar{t}H$ are assumed to be negligibly small [18] and are therefore neglected. The irreducible background from non-resonant ZZ production is estimated with the aid of dedicated MC samples (see previous Sections 4.1 and 4.3).

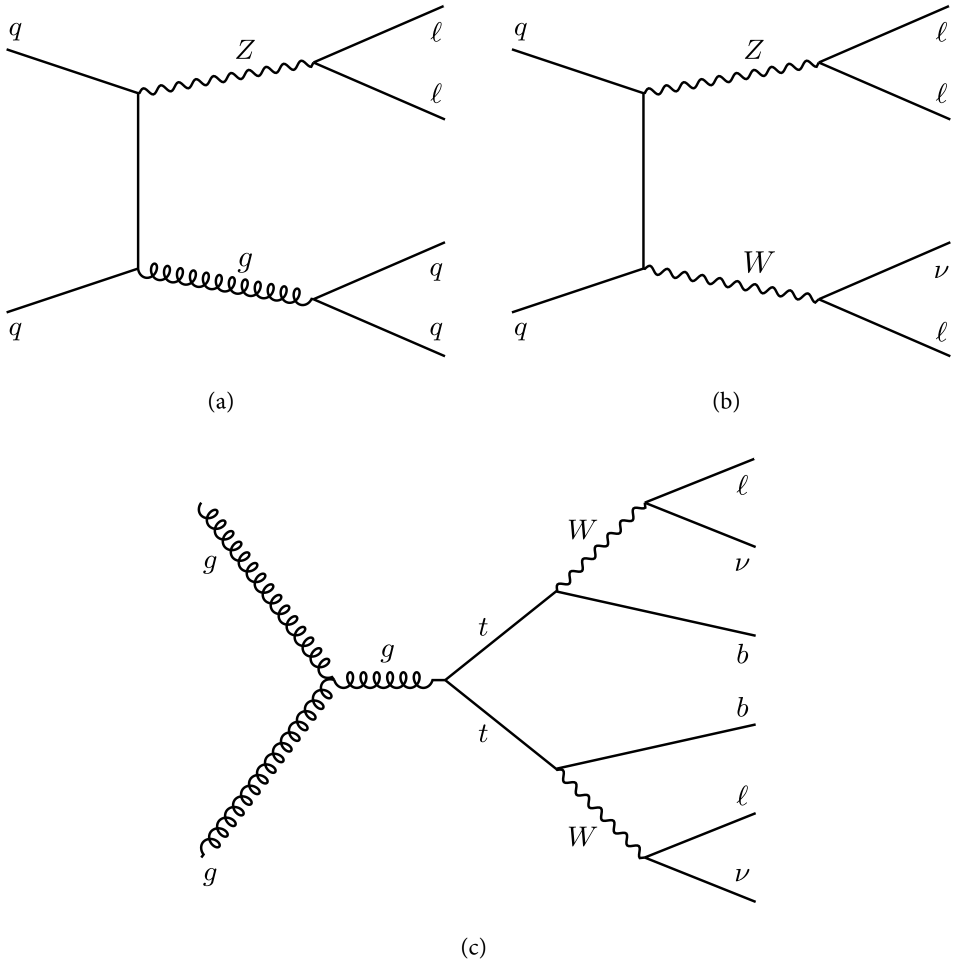

Figure 4.2: Leading-order Feynman diagrams for the main reducible background processes contributing to the Higgs boson decay channel $H \rightarrow ZZ^* \rightarrow 4\ell$: (a) Z + jets, (b) WZ and (c) $t\bar{t}$ production [72].

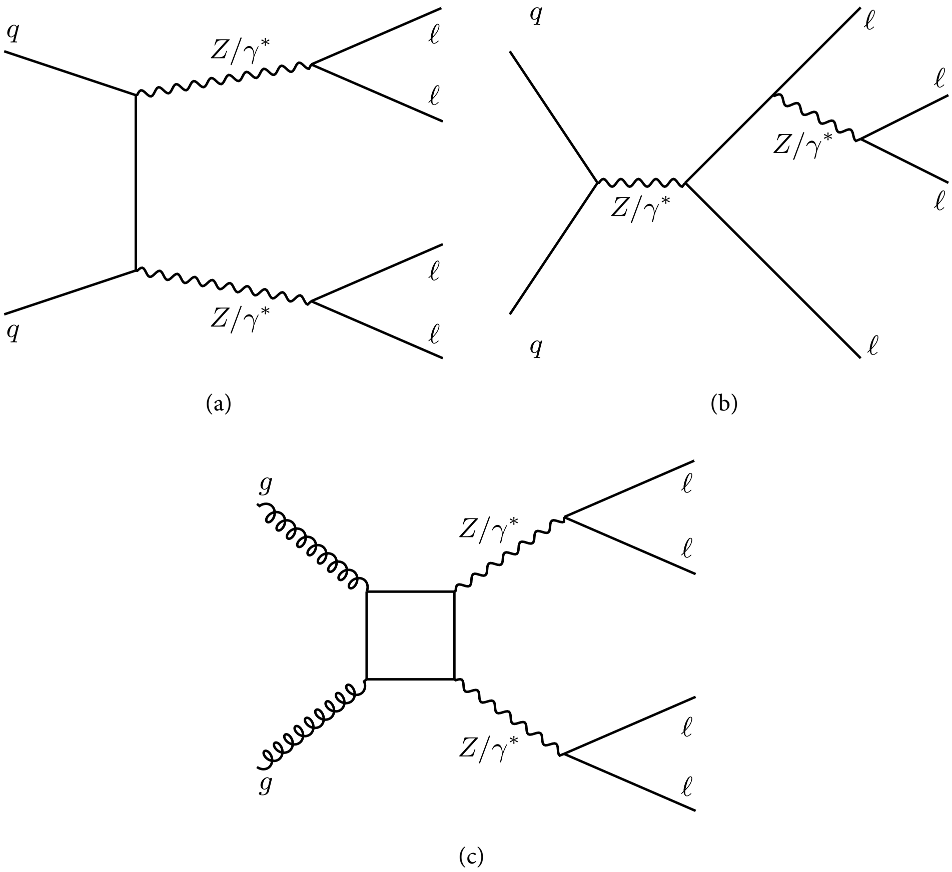

Figure 4.3: Leading-order Feynman diagrams for the main irreducible background processes contributing to the Higgs boson decay channel $H \rightarrow ZZ^* \rightarrow 4\ell$: Two quarks annihilate and either produce (a) a pair of Z bosons or photons or (b) create a Z boson with additional leptons through associated radiative lepton decay. The gluon–gluon fusion process (c) leads to the $ZZ^{(*)}$production through a quark loop [72].

Table 4.2: The number of expected events after the $H \rightarrow ZZ^* \rightarrow 4\ell$ event selection for a luminosity of 120 fb^{-1} given in terms of the individual Higgs boson production modes ggF, VBF, ZH and WH as well as the irreducible background from non-resonant $ZZ^{(*)}$ production. The number of expected events is listed per category according to the categorisation scheme of this thesis.

	ggF	VBF	ZH	WH	ZZ	Total
0-jet	86.28	0.95	0.53	0.74	45.77	134.27
1-jet	44.52	4.49	0.77	1.19	13.62	64.59
2-jet-sameHemi	11.72	1.36	0.75	1.10	3.36	18.29
2-jet-oppHemi	9.04	5.54	0.35	0.48	2.40	17.81
All	151.56	12.34	2.40	3.51	65.15	234.96

5

Anomalous coupling of the Higgs boson to gluons

In order search for anomalous $\mathcal{CP}$-odd contributions to the effective Higgs boson coupling to gluons, i. e. to study the sensitivity to physics scenarios with different BSM coupling parameter values, several $\mathcal{CP}$-sensitive observables are examined using simulated BSM signal and SM background samples. The variable $\Delta\phi_{jj}^{\text{sign}}$ corresponding to the azimuthal angle between the two leading jets produced together with the Higgs boson is shown to provide the largest sensitivity to possible admixtures of BSM couplings. Additionally, it is sensitive to the sign of the $\mathcal{CP}$-odd coupling strength parameter $s_\alpha \kappa_{Agg}$, allowing to probe for $\mathcal{CP}$-violation.

5.1 Monte Carlo simulations

The MC samples have been produced for different BSM parameter values. The existing MC samples from the official detailed simulation of the ATLAS detector are not suitable for sensitivity studies based on differential distributions of kinematic observables due to high statistical uncertainties, especially in final states with additional jets. Several example distributions obtained after the full event selection from the officially produced samples are shown in Figures 5.1 to 5.3. The BSM differential distribution shapes of the invariant mass of the two leading jets m_{jj} at particle-level (Figure 5.1(b)) do no show distinctive deviations from the SM shape, except of one or two individual bins. No clear trend is visible. The shapes of the distributions have large fluctuations at detector-level (Figure 5.1(a)), providing no clear usable tendency. The distributions of the leading jet transverse momentum p_{T}^{j1} at detector-level (Figure 5.2(a)) hint at a stronger shifting to lower values in the $\kappa_{Agg} = 0.5$ case than in the $\kappa_{Agg} = -0.5$ case, but no such information is clearly obtainable from the distributions at detector-level (Figure 5.2(b)). Thus, this behaviour might arise as a side effect from the reconstruction procedure, which in general tends to 'wash out' distinctive features. The distributions of the azimuthal angle difference $\Delta\phi_{jj}$ hint at distinctive features, but due to large statistical uncertainties are not suitable for a sensitivity study. Therefore, additional MC samples with a larger amount of data have been generated at particle-level. The values of BSM parameters have been chosen following the officially produced samples for the validation, and additional samples for more accurate sensitivity estimates.

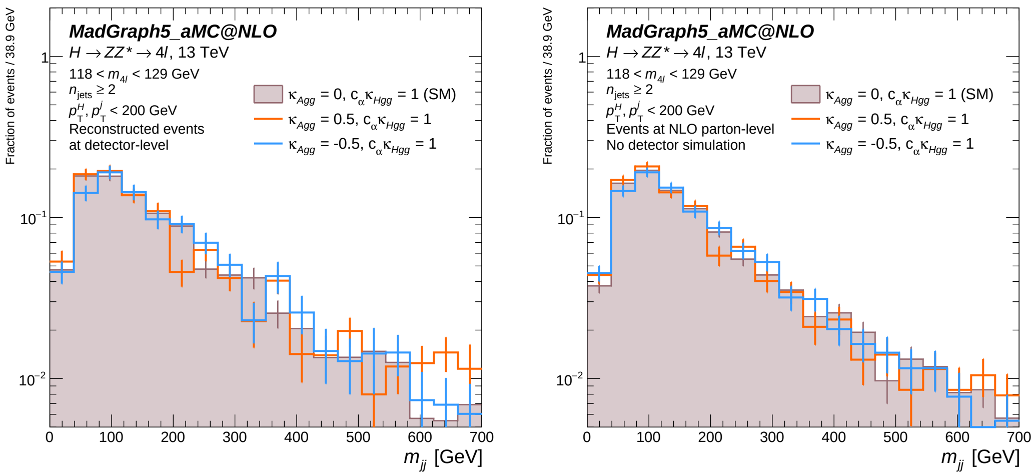

(a) (b)

Figure 5.1: Distributions of the invariant mass of the two leading jets in events with at least two final state jets (a) after full simulation of the detector response (detector-level) and (b) at particle-level for the SM scenario (grey shaded) and two $\mathcal{CP}$-odd coupling contributions scenarios.

5.1.1 Event generation

The signal events were generated using the official ATLAS simulation framework [126]. The parton-level generator MadGraph5_aMC@NLO v2_3_3_p1 [127] was used to model the ggF production of Higgs boson candidates at NLO with proton–proton collisions at $\sqrt{s} = 13$ TeV, using the NNPDF23LO [128] PDF set. The Higgs bosons are forced to decay into four leptons, i. e. $H \to ZZ^* \to 4\ell$. The BSM contributions in the interaction between the Higgs boson and gluons is implemented by means of the effective Lagrangian of the HC model (see Section 3.4.2).

Since the MadGraph5_aMC@NLO generator cannot simulate both, the production and decay processes with NLO accuracy at the same time, the MadSpin tool [129] is interfaced to MadGraph5_aMC@NLO to allow for the NLO accuracy of the $H \to ZZ^* \to 4\ell$ decay process. The resulting Les Houches [130] event files are then interfaced with Pythia 8.212 [119] for showering and hadronisation, using the A14 tune [131]. EvtGen [120] is used to simulate decays of B hadrons. In order to account for higher-order corrections essential for the loop-

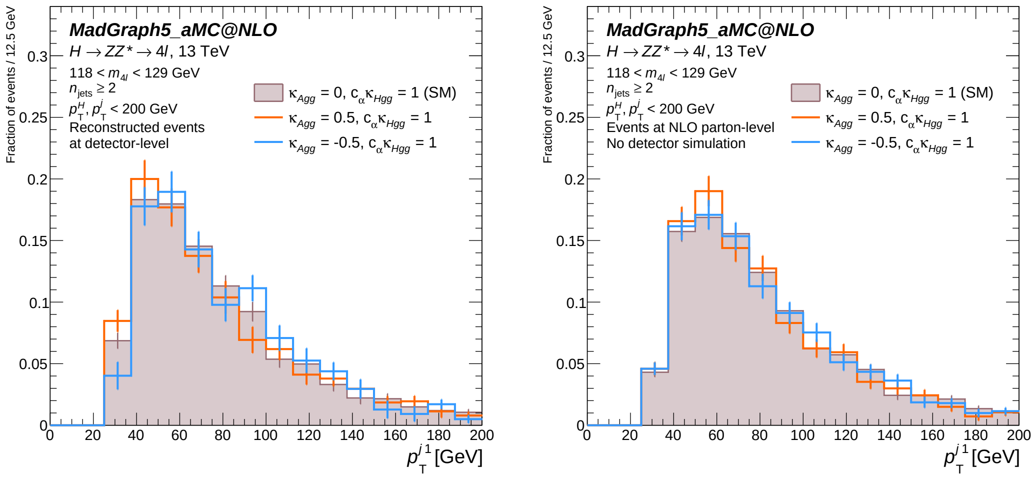

(a) (b)

Figure 5.2: Distribution of the leading jet transverse momentum in events with at least two final state jets (a) after full simulation of the detector response (detector-level) and (b) at particle-level for the SM scenario (grey shaded) and two $\mathcal{CP}$-odd coupling contributions scenarios.

induced ggF production mode, the FxFx merging technique [132] is used to match the final state jets after the parton shower and jet clustering to the original partons. In this way final states with multiple jets can be produced in ggF events generated at NLO.

5.1.2 Simulated points in the BSM parameter space

In order to study the impact of different values of the BSM $\mathcal{CP}$-odd coupling parameter $s_\alpha \kappa_{Agg}$, MC samples are produced for six values of base parameters, chosen such to allow for an interpolation in the interesting parameter range (see Table 5.1).
The sample for the SM scenario (`SM`), as well as two samples modelling the $\mathcal{CP}$-mixed states with $s_\alpha \kappa_{Agg} = \pm 0.5/\sqrt{2}$ (`BSMmix_kAgg_0p5`, `BSMmix_kAgg_n0p5`) and the pure $\mathcal{CP}$-odd sample (`BSMpure`) all have the same parameters as the corresponding fully simulated official MC samples and can therefore be used for the validation of the simulation framework. The validation results are presented in the next section.
In order to perform the sensitivity study, it is essential to model the signal for all possible values of BSM coupling parameters, not only the simulated ones. A continuous description of physical signal observables in the BSM coupling parameter space is provided by the morphing method described in Ref. [133]. The method allows for a signal interpolation in the BSM parameter space based on a complete and non-redundant set of input samples. The SM

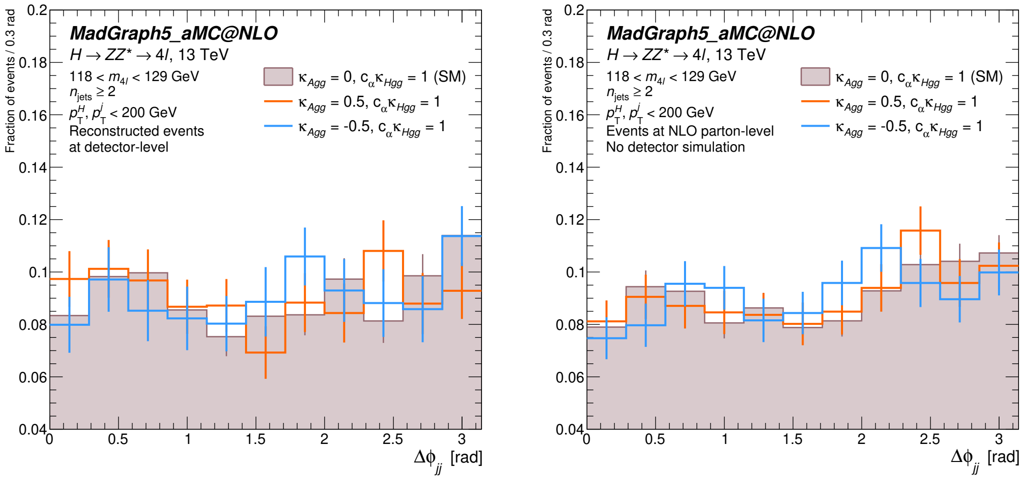

(a) (b)

Figure 5.3: Distribution of the azimuthal angle difference between the leading and the sub-leading jet in events with at least two final state jets (a) after full simulation of the detector response (detector-level) and (b) at particle-level for the SM scenario (grey shaded) and two $\mathcal{CP}$-odd coupling contributions scenarios.

sample together with two BSM mixture samples with $s_\alpha \kappa_{Agg} = \pm 2/\sqrt{2}$ (BSMmix_kAgg_2 and BSMmix_kAgg_n2), are used for this purpose. The values of $s_\alpha \kappa_{Agg} = \pm 2/\sqrt{2}$ have been chosen just to span the parameter space allowed by the current measurements (see Section 3.5.2). For the study of the $s_\alpha \kappa_{Agg}$ coupling in the ggF production vertex in this thesis three input samples are required. The $H \to ZZ^* \to 4\ell$ decay is assumed not to be affected by any BSM coupling contributions. The error associated with the prediction of the morphing method is negligible in the studied parameter range.

5.1.3 Validation of MC samples

In order to validate the generated MC samples, the differential distributions of selected observables in generated samples are compared to the same particle-level distributions form the corresponding official samples. A particle-level selection of four-lepton events (see Section 5.1.4) is applied.

Figures 5.4(a) and 5.4(b) representatively show the comparison of the distribution of the leading jet transverse momentum p_T^{j1} (SM sample) and of the signed difference in the azimuthal angle of the two leading jets $\Delta\phi_{jj}^{\text{sign}}$ (defined in Section 5.3) (BSMmix_kAgg_0p5 sample). In general the shapes show a good agreement, despite individual bins sometimes do not show coincidence within statistical uncertainties. Most likely this is the result of different Pythia

Table 5.1: List of ggF samples generated with MadGraph5_aMC@NLO for different values of the BSM $\mathcal{CP}$-odd parameter ($s_\alpha \kappa_{Agg}$). The respective cross-section at NLO is also shown, together with the total number of generated events.

Sample description	BSM parameter values				Cross-section [fb]	Number of generated events
	κ_{Hgg}	κ_{Agg}	c_α	s_α		
`SM`	1	0	1	0	4.1 ± 0.0093	470 000
`BSMmix_kAgg_n2`	1	−2	$\frac{1}{\sqrt{2}}$	$\frac{1}{\sqrt{2}}$	10 ± 0.022	470 000
`BSMmix_kAgg_2`	1	2	$\frac{1}{\sqrt{2}}$	$\frac{1}{\sqrt{2}}$	10 ± 0.025	450 000
`BSMmix_kAgg_0p5`	1	0.5	$\frac{1}{\sqrt{2}}$	$\frac{1}{\sqrt{2}}$	1.6 ± 0.0034	420 000
`BSMmix_kAgg_n0p5`	1	−0.5	$\frac{1}{\sqrt{2}}$	$\frac{1}{\sqrt{2}}$	1.6 ± 0.0030	370 000
`BSMpure`	0	1	$\frac{1}{\sqrt{2}}$	$\frac{1}{\sqrt{2}}$	2.3 ± 0.0043	450 000

versions used in the official MC samples generation (Pythia 8.210) and the MC samples generation within this study (Pythia 8.212).
Further validation plots for the `SM`, `BSMmix_kAgg_0p5`, `BSMmix_kAgg_n0p5` and `BSMpure` samples and additional observables can be found in Appendix B.

5.1.4 Particle-level $H \to ZZ^* \to 4\ell$ event selection

Since the study of the Higgs boson coupling tensor structure in this thesis is based upon particle-level information, the $H \to ZZ^* \to 4\ell$ particle-level event selection is employed on the generated MC data. The selection is a subset of the criteria applied after the full simulation of the detector response, i. e. on detector-level (see Section 4.2) and is briefly presented in the following, as well as provided as a tabulated summary in Table 5.2.
The selection of Higgs boson events at particle-level uses particle information from the *fiducial phase space*, which is the geometrical region lying within the detection capabilities of the ATLAS detector. All electrons (muons) with a transverse momentum $p_{\mathrm{T}} > 7\,\mathrm{GeV}$ (5 GeV) and pseudo-rapidity $|\eta| < 2.47$ (2.7) are paired into same-flavour opposite-charge dileptons which then are used to build potential final state quadruplets of the form 4μ, $2e2\mu$, $2\mu2e$ and $4e$. Fiducial jets undergo a jet–lepton–overlap removal only keeping jets with $\Delta R \geq 0.2$ (0.1) for electrons (muons). Furthermore, the jets are required to have transverse momenta greater than 30 GeV and must have an absolute rapidity lower than 4.4. Kinematic cuts are applied to the three leptons with the highest transverse momenta in each quadruplet requiring $p_{\mathrm{T}} > 20$, 15 and 10 GeV, respectively. The quadruplet with the dilepton invariant masses m_{12} and m_{34}

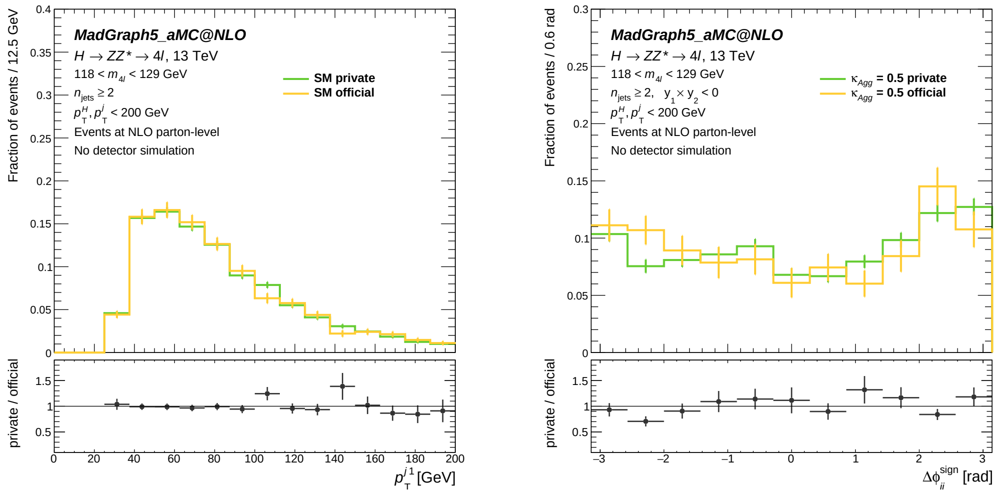

(a) (b)

Figure 5.4: Differential distributions of (a) the transverse momentum of the leading jet p_{T}^{j1} for the SM MC sample and (b) the difference $\Delta\phi_{jj}$ in the azimuthal angle of the two leading jets for the BSMmix_kAgg_0p5 MC sample generated within this work and the corresponding official MC sample at particle-level.

closest to the Z boson mass $m_Z = 91\,187.6$ MeV is then chosen as the final state quadruplet. In the next step certain Higgs boson selection criteria are employed on the quadruplet. The invariant masses of the four-lepton system and the two dileptons are constraint to mass ranges $118\,\mathrm{GeV} \leq m_{4\ell} \leq 129\,\mathrm{GeV}$, $50\,\mathrm{GeV} \leq m_{12} \leq 106\,\mathrm{GeV}$ and $12\,\mathrm{GeV} \leq m_{34}\ 115\,\mathrm{GeV}$, respectively. An angular separation $\Delta R \geq 0.1\ (0.2)$ is employed to same-flavour (opposite-flavour) leptons. Events with same-flavour leptons from J/ψ decays are rejected by requiring $m_{\ell\ell} \geq 5\,\mathrm{GeV}$ for the invariant mass of the lepton pair.
By setting thresholds for Higgs boson and jet transverse momenta of $p_{\mathrm{T}}^{H} \leq 200\,\mathrm{GeV}$ and $p_{\mathrm{T}}^{\mathrm{jet}} \leq 200\,\mathrm{GeV}$ the large top mass approximation is accounted for [97, 101–103] (see Section 3.4.1).
The selected events are categorised according to the event categorisation described in Section 4.2.

5.2 Signal model correction

The signal model is constructed by means of the morphing method using the input samples SM, BSMmix_kAgg_n2 and BSMmix_kAgg_2. The corrections described in the following are

Table 5.2: Event selection requirements applied within the $H \rightarrow ZZ^* \rightarrow 4\ell$ particle-level analysis in order to select suitable Higgs boson candidates for the sensitivity study within the work of this thesis.

Object selection	
Electrons	$p_T \geq 7$ GeV and $\lvert\eta\rvert \leq 2.47$
Muons	$p_T \geq 5$ GeV and $\lvert\eta\rvert \leq 2.7$
Jets	$p_T \geq 30$ GeV and $\lvert y\rvert \leq 4.4$ Jet–electron(–muon)–overlap removal: $\Delta R \geq 0.2$ (0.1)
Event selection	
Kinematic cuts	Perform on same-flavour opposite-charge dilepton pair quadruplets: Three highest-p_T leptons: $p_T > 20, 15$, and 10 GeV Angular separation of same-(opposite-)flavour leptons: $\Delta R \geq 0.1$ (0.1)
Mass ranges	Leading dileption invariant mass: 50 GeV $\geq m_{12} \geq$ 106 GeV Sub-leading dilepton invariant mass: 12 GeV $\geq m_{34} \geq$ 115 GeV Higgs boson mass range: 118 GeV $\geq m_{4\ell} \geq$ 129 GeV
J/ψ veto	Lepton pairs from different dileptons: $m_{\ell\ell} \geq 5$ GeV
Additional cuts	Higgs boson transverse momentum $p_T^H < 200$ GeV Jet transverse momenta $p_T^{\text{jet}} < 200$ GeV

applied to this signal model to account for the higher-order calculations and the impact of BSM coupling parameters on the total decay width of the Higgs boson.

5.2.1 Higher-order corrections

The samples used for this thesis are generated at NLO, while the inclusive production has been calculated at N^{3}LO [99, 100]. In addition the SM Powheg-Box sample provides an NNLO event-by-event accuracy for the inclusive ggF production. In order to take these higher-order calculations into account, appropriate corrections are applied on the generated MadGraph5_aMC@NLO samples. The Powheg-Box sample also provides the detector-level selection efficiency, as it is fully simulated with detailed ATLAS detector simulation. In order to account for both, the higher-order corrections and the difference between particle-level and detector-level selection, the so-called *best-prediction* scale factor f_c is applied to the predicted number of signal events in each event category c,

$$f_c = \frac{N_{\mathrm{SM},c}^{\mathrm{Powheg}}}{N_{\mathrm{SM},c}^{\mathrm{MG5}}} ,$$

where $N_{\mathrm{SM},c}^{\mathrm{Powheg}}$ is the number of expected events at a given luminosity provided by the Powheg-Box SM sample and $N_{\mathrm{SM},c}^{\mathrm{MG5}}$ is the number of events from SM MadGraph5_aMC@NLO SM sample. The Powheg-Box inclusive SM cross-section is scaled to the state-of-the-art N^{3}LO prediction. The best-prediction scale factors in each event category are shown in Table 5.3. The uncertainties for the estimated scale factors lie in the range of 0.4 % to 2.2 %. It is assumed, that the same scale factor obtained for the SM scenario can also be applied to BSM samples. This means, that the same higher-order corrections are assumed to hold for both, the SM and the BSM scenarios. Also, the four-lepton selection efficiency is assumed to be independent of SM or BSM coupling parameters. In order to test the latter assumption, the product of acceptance and efficiency

$$A \cdot \varepsilon = \frac{\text{Number of selected events}}{\text{Number of generated events}} ,$$

has been calculated for each of the generated SM and BSM MC samples from Table 5.1. The result is shown in Figure 5.5 for the inclusive four-lepton selection. Within the statistical uncertainty, the product $A \cdot \varepsilon$ is the same for MC samples with different BSM coupling parameter configurations.
Although the larger cross-section from higher-order calculations increases the number of expected events in each category by a factor of 1.24 to 1.48, the decrease due to the reconstruction efficiency prevails, leading to an eventual down scaling by a factor ranging from 0.73 to 0.81.

Table 5.3: Best-prediction scale factors calculated by taking the ratio of the number of expected events from the reconstructed Powheg-Box and the MadGraph5_aMC@NLO generator-level SM samples in each category.

Category	*0-jet*	*1-jet*	*2-jet-sameHemi*	*2-jet-oppHemi*	Total
Scale factor	0.73	0.77	0.81	0.79	0.75

5.2.2 Scaling of the total Higgs boson decay width

The probability for the Higgs boson to decay into a specific decay mode i is expressed by the branching ratio B_i defined as the ratio of the partial (Γ_i) to the total decay width (Γ)

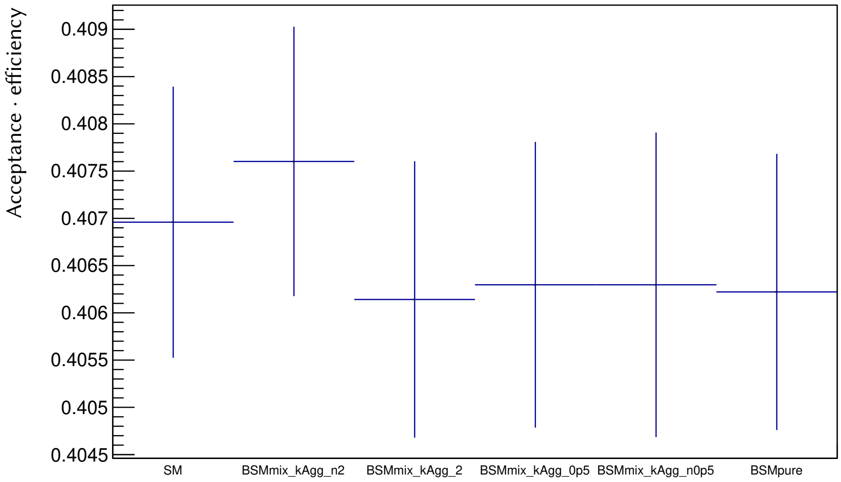

Figure 5.5: The product of acceptance and efficiency ($A \cdot \varepsilon$) as the ratio of selected to generated events for each MC sample.

$$B_i = \frac{\Gamma_i}{\Gamma} \, .$$

The partial decay widths Γ_i and consequently the total decay width Γ are affected by the BSM contributions in the tensor structure of the Higgs boson coupling. In the generated MadGraph5_aMC@NLO samples, the partial decay widths are correctly adjusted according to the input values of BSM parameters. However, the total decay width in these generated events is fixed to the SM value $\Gamma = \Gamma_{\mathrm{SM}}$ and needs to be corrected. For this purpose a correction function $f^{\Gamma}(\vec{g}_{\mathrm{BSM}})$ is determined for a given set $\vec{g}_{\mathrm{BSM}}$ of BSM coupling parameters

$$\begin{aligned} f^{\Gamma}(\vec{g}_{\mathrm{BSM}}) &= \frac{\Gamma_{\mathrm{SM}}}{\Gamma_{\mathrm{BSM}}} \\ &= \frac{\Gamma_{\mathrm{SM}}}{\sum_i \Gamma_{\mathrm{BSM},i}} \\ &= \frac{\Gamma_{\mathrm{SM}}}{\sum_i \Gamma_{\mathrm{SM},i} \cdot f_i(\vec{g}_{\mathrm{BSM}})} \\ &= \frac{1}{\sum_i B_{\mathrm{SM},i} \cdot f_i(\vec{g}_{\mathrm{BSM}})} \, . \end{aligned}$$

The individual correction function for each decay mode i is denoted by $f_i(\vec{g}_{\mathrm{BSM}})$. For the SM

Table 5.4: The SM values for the branching ratios of Higgs boson decays into a pair of gluons (B_{gg}) and into all remaining SM decays ($B_{\text{otherdecays}}$) together with the values of constant coefficients c_1^{gg} and c_2^{gg} used in the correction formula for the Higgs boson decay width (compare Eq. 5.2).

Branching ratios		Coefficients	
$B_{\text{other decays}}$	B_{gg}	c_1^{gg}	c_2^{gg}
0.9143	0.0857	2.285	0

scenario, the individual correction function is equal to 1 for each decay mode. The $\mathcal{CP}$-odd coupling parameter $s_\alpha \kappa_{Agg}$ affects the decay width for the Higgs boson decay into a pair of gluons, thus altering the total Higgs boson decay width. Since other anomalous coupling contributions are assumed to be zero in this analysis,the correction function can be written as

$$f^{\Gamma}(\vec{g}_{\text{BSM}}) = \frac{1}{B_{\text{other decays}} + B_{gg} \cdot f_{gg}\big(s_\alpha \kappa_{Agg}\big)} , \tag{5.1}$$

with B_{gg} and $B_{\text{other decays}}$ being the SM value of the $H \to gg$ branching ratio and the sum of the SM values of all other branching ratios, respectively. The correction function f_{gg} is a polynomial of the form

$$f_{gg}\big(s_\alpha \kappa_{Agg}\big) = \big(c_\alpha \kappa_{Hgg}\big)^2 + c_1^{gg} \cdot \big(s_\alpha \kappa_{Agg}\big)^2 + c_2^{gg} \cdot c_\alpha \kappa_{Hgg} s_\alpha \kappa_{Agg} . \tag{5.2}$$

The values for the branching ratios B_{gg} and $B_{\text{other decays}}$ and coefficients c_1^{gg} and c_2^{gg} used in Eqs. 5.1 and 5.2, respectively, are listed in Table 5.4. The constants c_i^{gg} are calculated by using the morphing method from the cross-section values of the input samples [125, 133]. The total decay width at a given BSM point $\vec{g}_{\text{BSM}}$ is then obtained by multiplying the SM value with the value of the correction function $f^{\Gamma}(\vec{g}_{\text{BSM}})$.
The resulting correction function $f^{\Gamma}(\vec{g}_{\text{BSM}})$ is drawn in Figure 5.6. Since all correction values are smaller than or equal to 1, the number of expected events from MC simulations is an overestimation of the correct expectation. In the currently experimentally allowed $s_\alpha \kappa_{Agg}$ parameter range from −0.67 to 0.64 [18] the correction is lies between 7.4 % and 8.1 %.
A detailed description of the total decay width correction is provided in [125].

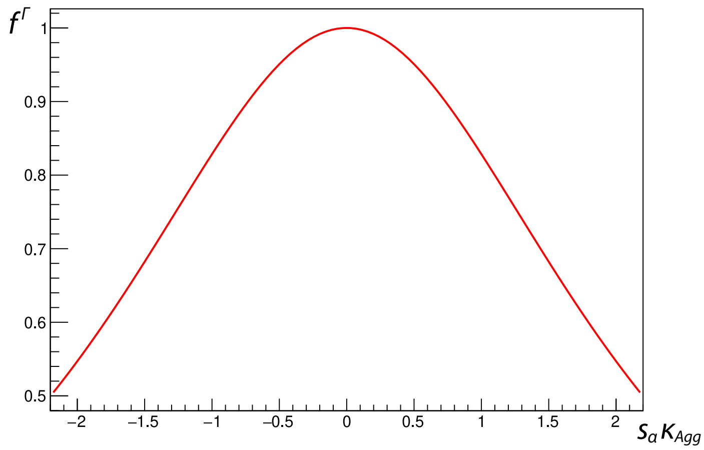

Figure 5.6: The multiplicative correction factor to the Higgs boson decay width as a function of the $\mathcal{CP}$-odd BSM parameter $s_{\alpha}\kappa_{Agg}$. The correction function is defined as the ratio $\Gamma_{\mathrm{SM}}/\Gamma_{\mathrm{BSM}}$ between the total decay width Γ_{SM} in the SM scenario and the total decay width Γ_{BSM} in the presence of the BSM parameter $s_{\alpha}\kappa_{Agg}$.

5.3 $\mathcal{CP}$-sensitive observables

The presence of BSM contributions to the Higgs boson coupling to gauge bosons affects rather strongly the rates of the Higgs boson production. However, as evident from former studies [18] (see Section 3.5.2), this observable does not provide direct sensitivity to $\mathcal{CP}$-violation, since the rates can be also changed by the $\mathcal{CP}$-even parameter $c_{\alpha}\kappa_{Hgg}$. The $\mathcal{CP}$-violating effects would manifest themselves in asymmetric distributions of kinematic properties of final state products, i. e. in distributions, which are sensitive to the sign of the $\mathcal{CP}$-odd BSM coupling parameter $s_{\alpha}\kappa_{Agg}$. The final state products originating from the ggF production vertex are the jets, as illustrated with Feynman diagrams in Figure 3.6. Therefore, the properties of theses jets are studied in this thesis.
The distributions of the related kinematic variables, such as the invariant mass m_{jj} and the pseudo-rapidity difference $\Delta\eta_{jj}$ of the two leading jets are shown in Figure 5.7.
Although the m_{jj} distribution changes with different BSM scenarios at large m_{jj} values, a very poor discrimination of $s_{\alpha}\kappa_{Agg}$ values can be made with these observables.
Motivated by the phenomenological studies of gluon-induced $pp \to H + 2j$ processes in Ref. [103], the main sensitivity is expected to come from angular correlations between the two highest-p_{T} jets [134–138]. Therefore, the difference $\Delta\phi_{jj} = \phi(j1) - \phi(j2)$ in the azimuthal angle of the two leading jets is studied. The distribution of this observable is shown in Figure 5.8 for the SM and different BSM scenarios.

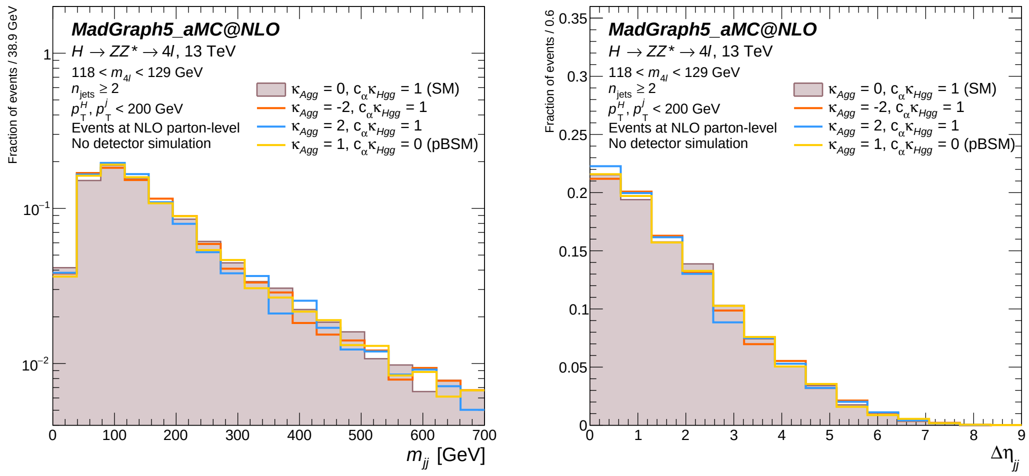

(a)

(b)

Figure 5.7: The normalised distributions of (a) the invariant mass m_{jj} and (b) the pseudo-rapidity difference $\Delta\eta_{jj}$ of the two leading jets in ggF Higgs boson production after the four-lepton selection. The distributions are shown for the SM scenario (grey shaded), a pure BSM $\mathcal{CP}$-odd (yellow) as well as BSM mixed $s_\alpha \kappa_{Agg} = \pm 2/\sqrt{2}$ scenarios (red and blue, respectively).

The regions with $1 \lesssim \Delta\phi_{jj} \lesssim 2.3$ and $2.3 \lesssim \Delta\phi_{jj} \lesssim 3.1$ allow for a clear distinction between the absence and the presence of an anomalous $\mathcal{CP}$-odd contribution to the Hgg coupling. The separation from the SM is slightly more pronounced in the case of the pure BSM sample, but samples with mixed SM and BSM contributions can also be discriminated from the SM scenario. However, the sign of the $s_\alpha \kappa_{Agg}$ coupling parameter in mixed samples cannot be distinguished.

An alternative, so-called 'signed', definition of the difference in the azimuthal angle between the two leading jets $\Delta\phi_{jj}$ is obtained by setting constraints on the orientations of the two jets

$$\Delta\phi_{jj}^{\text{sign}} = \phi(j_+) - \phi(j_-) \; .$$

The two jets are restrained to lie in opposite hemispheres, with j_+ being the jet in the hemisphere with positive rapidity $y > 0$ and j_- in the hemisphere with negative rapidity $y < 0$. An illustration of the $\Delta\phi_{jj}^{\text{sign}}$ definition is given in Figure 5.9.

The $\Delta\phi_{jj}^{\text{sign}}$ distribution is shown in Figure 5.10. As for $\Delta\phi_{jj}$, the SM and the pure BSM scenario can be clearly distinguished.

While in the SM case the minima of the distribution are at $\pm\pi/2$, the pure BSM scenario

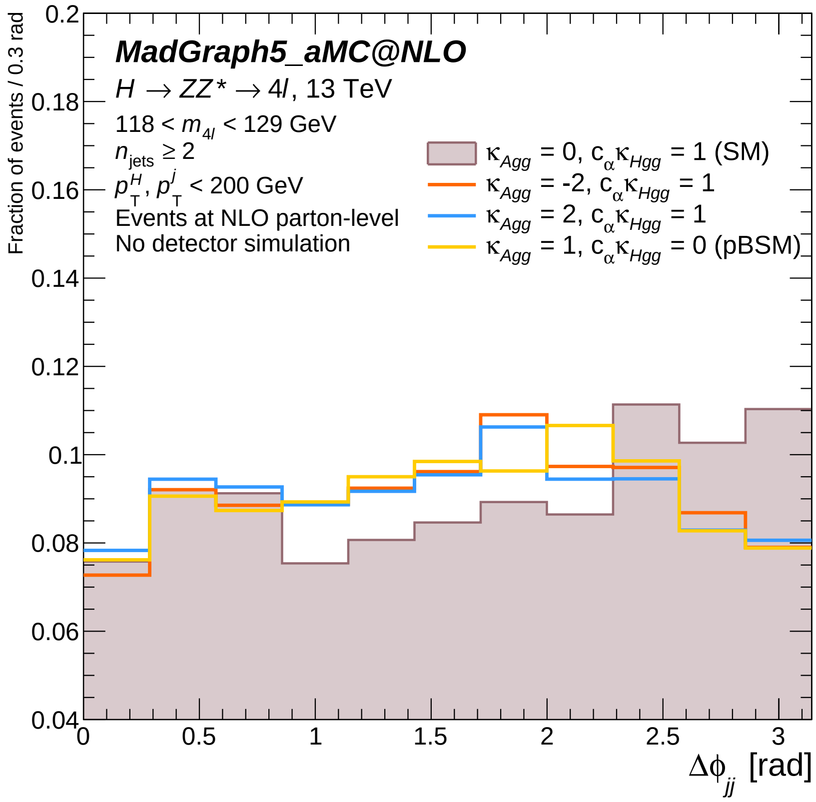

Figure 5.8: The normalised distribution of the difference $\Delta\phi_{jj}$ in the azimuthal angle of the two leading jets in ggF Higgs boson production after the four-lepton selection. The distributions are shown for the SM scenario (shaded grey), the pure BSM $\mathcal{CP}$-odd scenario (yellow) as well as BSM mixed $s_\alpha \kappa_{Agg} = \pm 2/\sqrt{2}$ scenarios (red and blue, respectively).

predicts minima at 0 and $\pm\pi$. In addition, the sensitivity to the sign of the $\mathcal{CP}$-odd coupling strength parameter $s_\alpha \kappa_{Agg}$ is recovered through the asymmetric distribution from the mixed SM and BSM samples. The position of local maxima can be observed accordingly. For $\mathcal{CP}$-mixed scenarios, the distribution in the case of the parameter value $s_\alpha \kappa_{Agg} = -2/\sqrt{2}$ results in a more pronounced maximum at around $\Delta\phi_{jj}^{\text{sign}} = -2$ rad, while for $s_\alpha \kappa_{Agg} = 2/\sqrt{2}$ the maximum is at the opposite side at the value of $\Delta\phi_{jj}^{\text{sign}} = 2$ rad.
Following the studies of Ref. [103], additional discrimination between SM and BSM scenarios is expected by selecting events with large m_{jj} and $\Delta\eta_{jj}$ values. These selection requirements have not been applied in this thesis due to the limited number of expected events in the four-lepton final state.

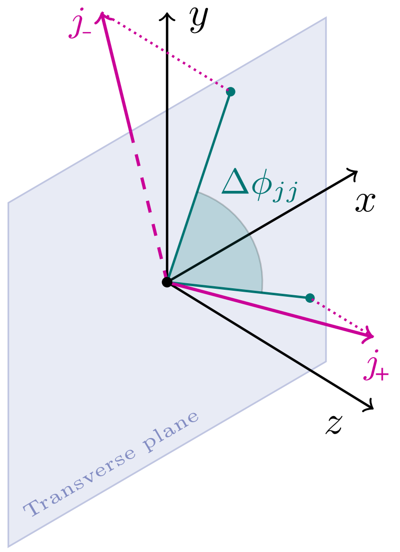

Figure 5.9: The signed difference in the azimuthal angle between the jet j_+ pointing in the detector hemisphere with positive rapidity and the jet j_- with negative rapidity.

5.4 Results

In order to evaluate the sensitivity to the $\mathcal{CP}$-odd BSM coupling parameter $s_\alpha \kappa_{Agg}$, expected constraints on this coupling are evaluated at 68 % and 95 % confidence level (CL). The expected sensitivity from the $\Delta\phi_{jj}^{\text{sign}}$ observable is evaluated assuming a dataset with an integrated luminosity of 120 fb^{-1}, which is expected by the end of the LHC Run 2 in 2018. With the LHC roadmap aiming for an integrated luminosity of about 300 fb^{-1} at the end of Run 3 in 2021 and with the high-luminosity LHC project (HL-LHC) designed for 3000 fb^{-1} until 2030, an outlook is given also for these higher-luminosity scenarios.

The sensitivity to the coupling parameter $s_\alpha \kappa_{Agg}$ is determined from a likelihood function [94], defined as a product of Poisson probabilities P,

$$L\left(\text{data}|\kappa_{Agg}\right) = \prod_i^{N_\text{cat}} \prod_j^{N_\text{bins}} P\left(N_{i,j}|S_{i,j}\left(s_\alpha \kappa_{Agg}\right) + B_{i,j}\right) ,$$

with 'data' being represented by MC simulation, $N_{i,j}$ the number of observed events in event category i and bin j of the studied observable (event yield or $\Delta\phi_{jj}^{\text{sign}}$ differential distribution), $N_\text{cat} = 4$ the number of event categories and N_bins the number of bins of the utilised observable. Since the shape information of the $\mathcal{CP}$-sensitive observable $\Delta\phi_{jj}^{\text{sign}}$ is only used in the event category with two opposite-hemisphere jets (*2-jet-oppHemi*), the number of bins is

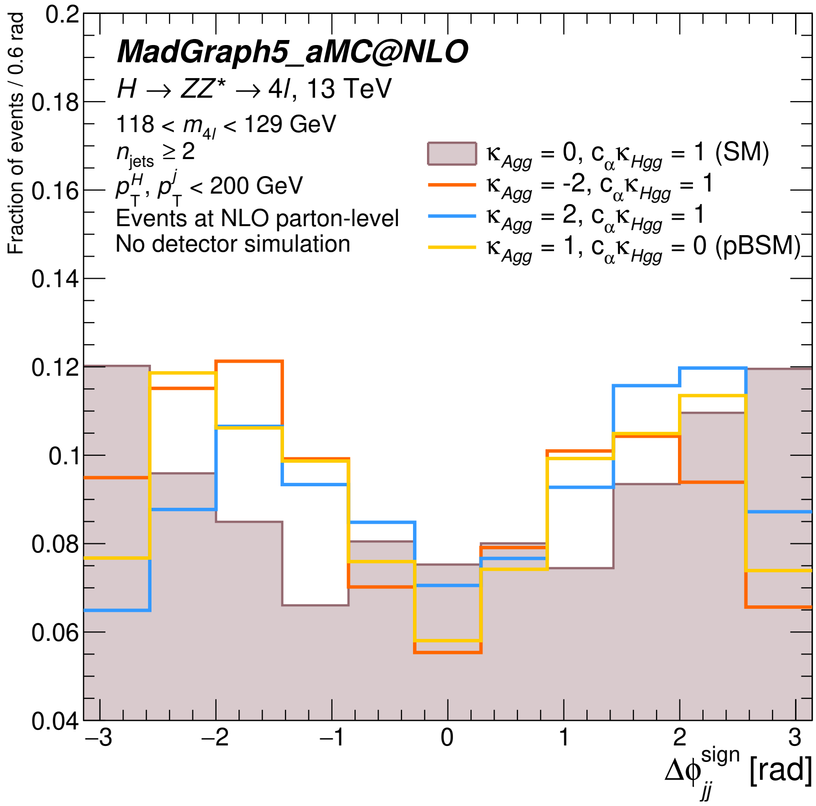

Figure 5.10: The normalised distribution of the signed difference $\Delta\phi_{jj}^{\text{sign}}$ of the azimuthal angle difference of the two leading jets pointing to opposite hemispheres. The kinematic properties are shown for ggF Higgs boson production after the four-lepton selection. The distributions are shown for the SM (shaded grey), the pure BSM $\mathcal{CP}$-odd (yellow) as well as two mixed BSM scenarios, which correspond to anomalous $\mathcal{CP}$-odd coupling strength parameters $s_\alpha \kappa_{Agg} = \pm 2/\sqrt{2}$ (red and blue, respectively).

different from 1 only in this category, i. e. $N_{\text{bins}} = 11$. In the remaining categories only the corresponding event yield is used. $S_{i,j}$ is the predicted number of signal events and $B_{i,j}$ the expected background for event category i and bin j. The Poisson probabilities represent the likelihood to observe $N_{i,j}$ events given the expectations from signal and background in the corresponding category and bin. In order to compare the hypotheses with different $s_\alpha \kappa_{Agg}$ values, a test statistic [94] based on a ratio of profile likelihoods is used:

$$t = -2 \ln \lambda \equiv -2 \ln \frac{L(\kappa_{Agg})}{L(\hat{\kappa}_{Agg})}, \tag{5.3}$$

with $\hat{\kappa}_{Agg}$ being the best-fit value of the BSM coupling parameter obtained by maximising the likelihood function with free κ_{Agg} parameter. The fit of the signal-plus-background model is performed on pseudo-data in the form of so-called *Asimov* data sets [94]. An Asimov data set corresponds to one large simulated signal sample, which is used as reference data. $L(\kappa_{Agg})$ is evaluated for a set of fixed κ_{Agg} values, allowing for a scan of the test statistic in dependence on κ_{Agg}. Two different Asimov data sets are used: 1. An SM Asimov data set for the test of the SM hypothesis is built from the generated SM sample, and 2. a BSM Asimov data set with the current best-fit value of the BSM parameter $s_\alpha \kappa_{Agg} = 0.43$ [18]. This data set is used for the test of a representative BSM hypothesis.
Measurements are affected by statistical and systematic uncertainties. The latter arise from limitations related to the ATLAS detector, such as uncertainties in luminosity determination, final state particle reconstruction, pile-up modelling or data-driven background estimation. Systematic uncertainties from theoretical predictions also contribute. They are related to the QCD scale, PDF sets and parton shower simulation [125]. Since the systematic uncertainties are expected to be small compared to the statistical uncertainties, especially in the *2-jet-oppHemi* event category, they have been neglected in this thesis.

Comparison with current results from the data set with 36.1 fb^{-1}

Using SM Asimov pseudo-data for an integrated luminosity of 36.1 fb^{-1}, the results are compared to the ones from the most recent published analysis [18]. Figure 5.11 shows the expected test statistic from a scan over the $s_\alpha \kappa_{Agg}$ parameter values. The results from the published analysis use only the event yields in each event category as the final observable, while the results from this thesis include also the information from the shape of the differential distribution of $\Delta\phi_{jj}^{\text{sign}}$.
The contamination from the VBF and VH Higgs boson production and from the dominant ZZ background is taken into account based on the predictions from the published analysis and assuming, that there are no BSM coupling contributions to these processes. In order to have a more realistic comparison, only statistical uncertainties are considered.
The exclusion limits under the SM hypothesis are $[-0.29, 0.30]$ at 68 % CL and $[-0.42, 0.43]$ at 95 % CL, when $\Delta\phi_{jj}^{\text{sign}}$ information is taken into account. The expected exclusion limits are about 5 % worse than the published ones, most likely due to the more involved event categorisation in the case of the published analysis.

Sensitivity at the end of the LHC Run 2

In order to compare the sensitivity with and without the $\Delta\phi_{jj}^{\text{sign}}$ observable, this time using the SM Asimov data set for 120 fb^{-1}, the set-up using only event yields in simplified event categories from this thesis is compared to a set-up using also the $\Delta\phi_{jj}^{\text{sign}}$ observable (see Figure 5.12).

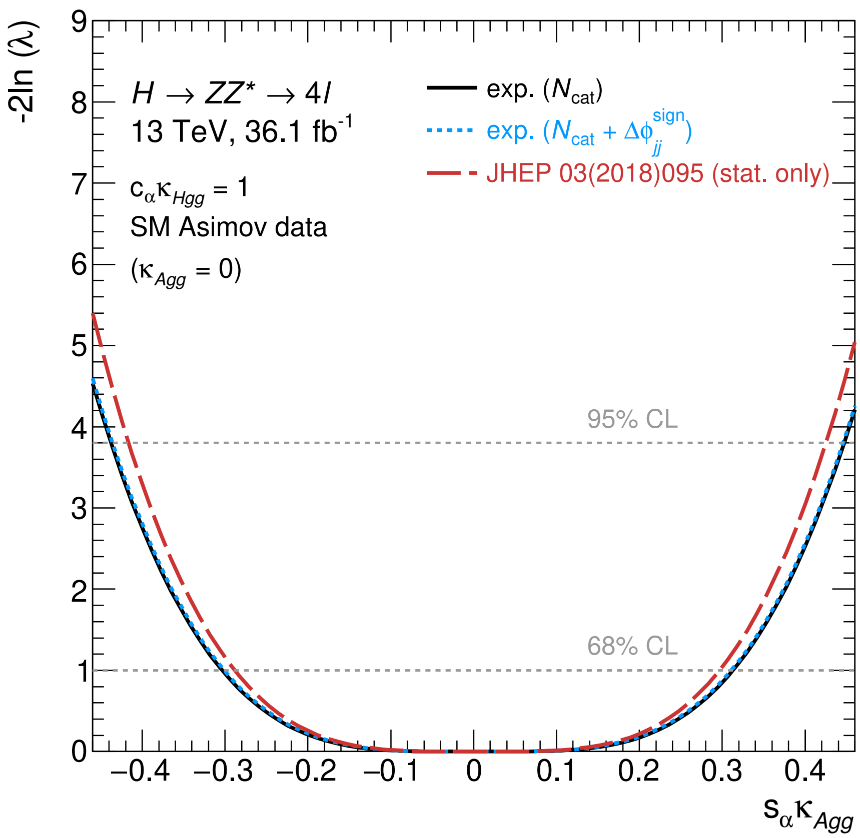

Figure 5.11: Expected test statistic under the SM hypothesis as a function of the $\mathcal{CP}$-odd coupling parameter $s_\alpha \kappa_{Agg}$ for an integrated luminosity of 36.1 fb^{-1} for the published analysis with statistical uncertainties only (black), one for the analysis based on event yields in the event categories from Section 4.2 (red dashed) and the corresponding analysis utilising in addition the $\mathcal{CP}$-sensitive observable $\Delta\phi_{jj}^{\text{sign}}$ (blue). Dashed horizontal lines indicate the thresholds corresponding to 68 % and 95 % CL intervals.

The distributions of the test statistic (Eq. 5.3) as a function of the $\mathcal{CP}$-odd coupling parameter $s_\alpha \kappa_{Agg}$ are similar, i. e. the $\Delta\phi_{jj}^{\text{sign}}$ observable gives very little additional sensitivity under the SM hypothesis. The 68 % CL and 95 % CL limits are listed in Table 5.5. The BSM parameter is constrained to $[-0.31, 0.33]$ at 95 % CL.

In order to see, that the width of the exclusion limits scales as expected, one can perform an estimate of how the statistical uncertainty scales with the integrated luminosity,

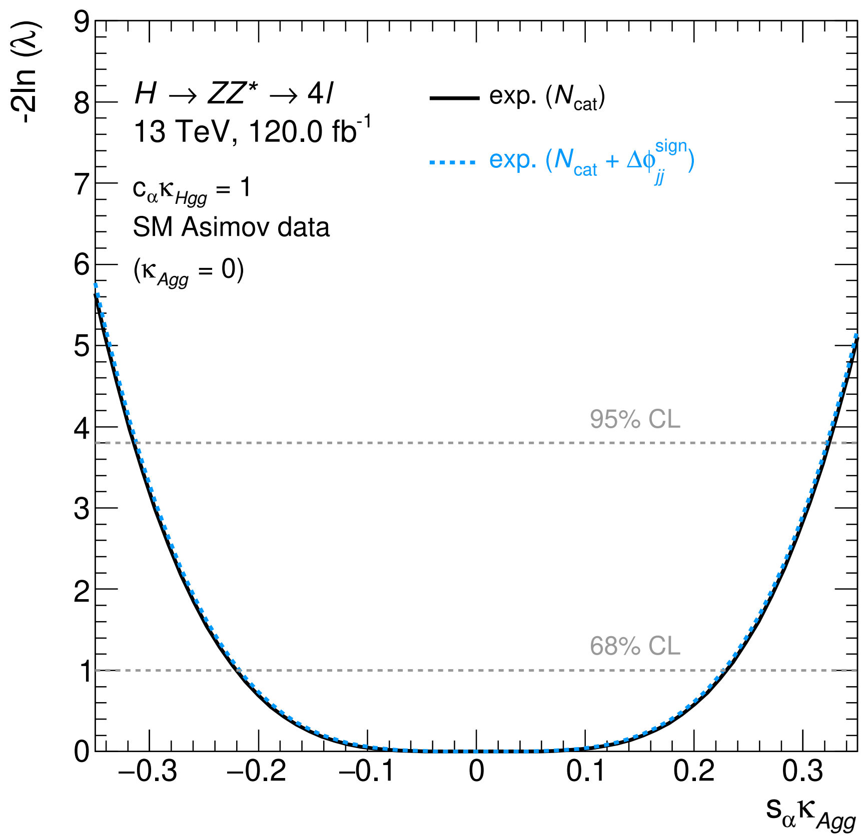

Figure 5.12: Expected test statistic under the SM hypothesis as a function of the $\mathcal{CP}$-odd coupling parameter $s_\alpha \kappa_{Agg}$ for an integrated luminosity of 120 fb^{-1} at a centre-of-mass energy of $\sqrt{s}$ = 13 TeV for the analysis based on event yields in the event categories from Section 4.2 (solid black) and the corresponding analysis utilising in addition the $\mathcal{CP}$-sensitive observable $\Delta\phi_{jj}^{\text{sign}}$ (dotted blue). Dashed horizontal lines indicate the thresholds corresponding to 68 % and 95 % CL intervals.

assuming a Poisson distribution so that a standard deviation of 1σ corresponds to $\sqrt{N}$, for N being the number of expected events. Using a shorthand notation for the $\mathcal{CP}$-odd coupling parameter $\kappa \equiv s_\alpha \kappa_{Agg}$ and considering the relations $N \propto L\sigma$ and $\sigma \propto \kappa^2$ with L and σ being the integrated luminosity and the ggF cross-section, respectively, the number of events expected as a function of κ can be written as (omitting prefactors)

$$N = \kappa^2 + N_{\text{SM}} \, , \tag{5.4}$$

with N_{SM} being the event yield predicted by the SM for a given integrated luminosity. Assuming an integrated luminosity L_1, the half width of the 1σ exclusion interval is expected at $N_1 = N_{\mathrm{SM}} + \sqrt{N_{\mathrm{SM}}}$ events. Therefore, the value for κ, where 1σ is located, κ_{L_1}, can be retrieved from

$$N_{\mathrm{SM}} + \sqrt{N_{\mathrm{SM}}} = \kappa_{L_1}^2 + N_{\mathrm{SM}} \quad \Longrightarrow \quad \kappa_{L_1} = \sqrt[4]{N_{\mathrm{SM}}}\,. \tag{5.5}$$

Transitioning from the luminosity L_1 to L_2, the number of expected events scales with $l \equiv L_2/L_1$, i. e. the number of events expected for a luminosity L_2 is $N_2 = lN_1$. With Equations 5.4 and 5.5, the half width of the 1σ exclusion interval κ_{L_2} can be estimated from

$$lN_{\mathrm{SM}} + \sqrt{lN_{\mathrm{SM}}} = l\kappa_{L_2}^2 + lN_{\mathrm{SM}} \quad \Longrightarrow \quad \kappa_{L_2} = \sqrt[4]{\frac{N_{\mathrm{SM}}}{l}} = \kappa_{L_1}\sqrt[4]{\frac{1}{l}} = \kappa_{L_1}\sqrt[4]{\frac{L_1}{L_2}}\,,$$

where N_{SM} is the event yield predicted by the SM for the integrated luminosity L_1. This implies, that the product of the half width of the 1σ exclusion limit κ and the fourth root of the corresponding integrated luminosity L is a constant quantity

$$\kappa \cdot \sqrt[4]{L} = \text{const.}\,,$$

which is approximatively the case for the results obtained in this thesis.

The two analysis approaches with and without the $\Delta\phi_{jj}^{\mathrm{sign}}$ variable are also compared to each other under the employment of the BSM Asimov data set with an integrated luminosity of 120 fb^{-1} (see Figure 5.13).
In this case, a sensitivity improvement is expected, when utilising the $\mathcal{CP}$-sensitive observable $\Delta\phi_{jj}^{\mathrm{sign}}$. This observable allows for the discrimination of the sign of the coupling parameter $s_\alpha\kappa_{Agg}$, as opposed to the event yield information only. The $\Delta\phi_{jj}^{\mathrm{sign}}$ distribution allows for an exclusion of the wrong-sign hypothesis at almost 68 % CL. The SM signal in this BSM scenario can be excluded at the level of more than 2σ (standard deviations). The 68 % CL and 95 % CL limits are listed in Table 5.5.

Sensitivity at the end of LHC Run 3 and at the end of HL-LHC operation

In order to study the signal sensitivity with an increasing amount of data, the scans of the expected test statistic over different values of the $\mathcal{CP}$-odd coupling parameter $s_\alpha\kappa_{Agg}$ are performed also for integrated luminosities of 300 fb^{-1} and 3000 fb^{-1}. In all cases, the $\Delta\phi_{jj}^{\mathrm{sign}}$

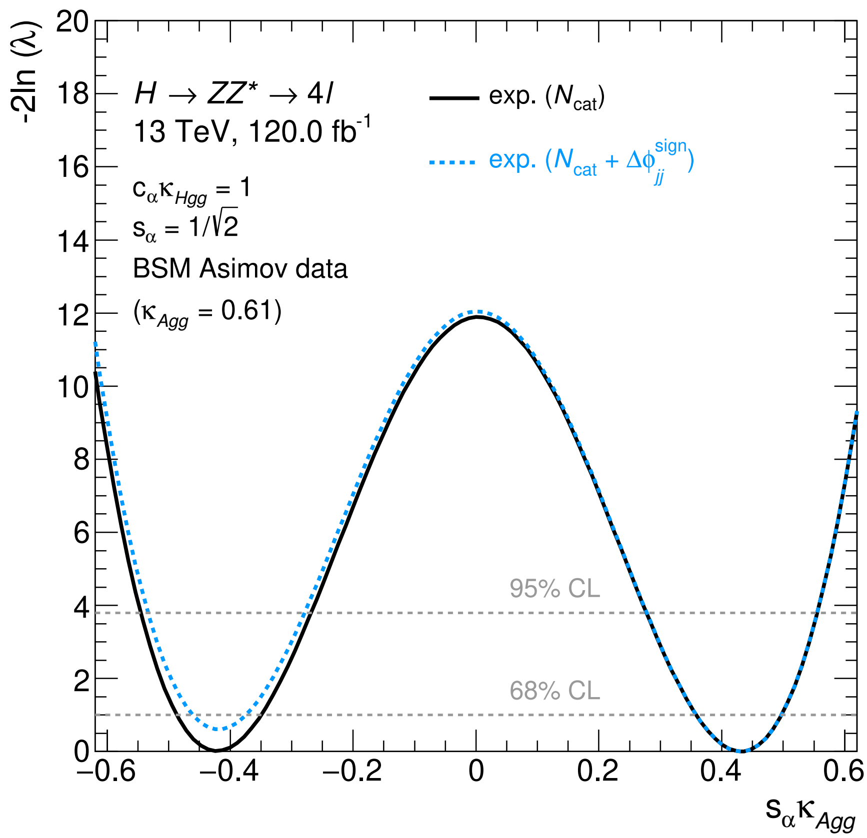

Figure 5.13: Expected test statistic under the BSM hypothesis represented by an Asimov data set with a $\mathcal{CP}$-odd coupling strength parameter value of $s_\alpha \kappa_{Agg} = 0.43$ as a function of $s_\alpha \kappa_{Agg}$ for an integrated luminosity of 120 fb^{-1} at a centre-of-mass energy of $\sqrt{s} = 13$ TeV for the analysis based on event yields in the event categories (solid black) and the corresponding analysis utilising in addition the $\mathcal{CP}$-sensitive observable $\Delta\phi_{jj}^{\mathrm{sign}}$ (dotted blue). Dashed horizontal lines indicate the thresholds corresponding to 68 % and 95 % CL intervals.

observable is included in the fit results. Figure 5.14 shows the corresponding scans for the BSM Asimov data sets with integrated luminosities of 120 fb^{-1}, 300 fb^{-1} and 3000 fb^{-1} corresponding to the expectations at the end of the LHC Run 2 and Run 3, as well as at the end of the HL-LHC project, respectively.

The exclusion limits at $s_\alpha \kappa_{Agg} = 0.43$ improve with increasing luminosity. With 300 fb^{-1} of data, the wrong-sign hypothesis $s_\alpha \kappa_{Agg} = -0.43$ is disfavoured at the level of more than 1σ under the BSM $s_\alpha \kappa_{Agg} = 0.43$ hypothesis. With 3000 fb^{-1} of data, the wrong sign hypothesis

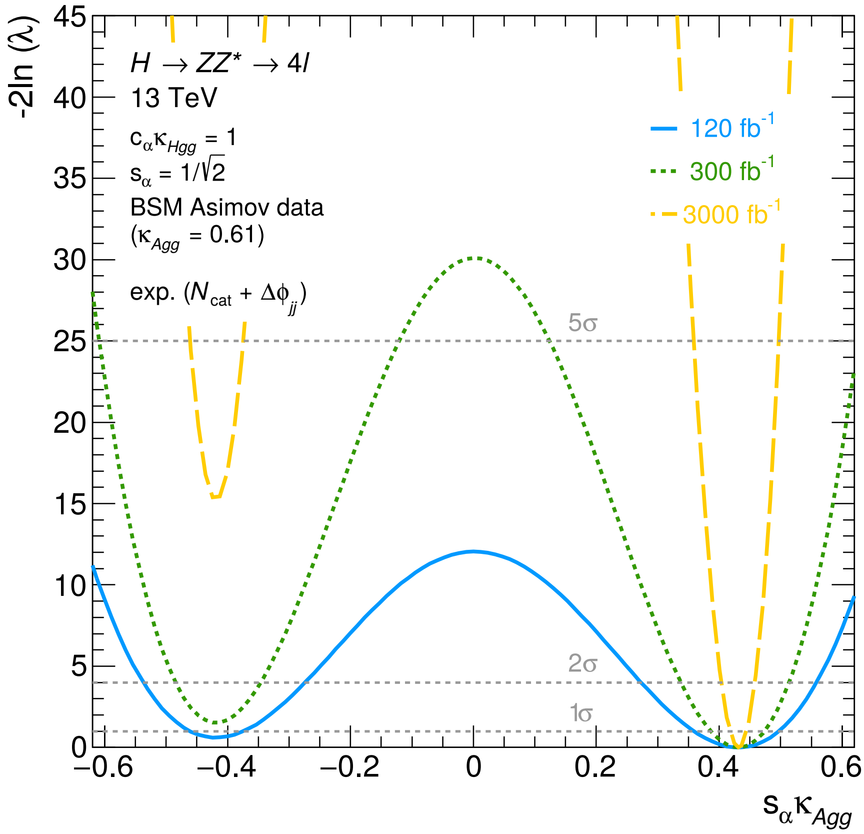

Figure 5.14: Expected test statistics for BSM pseudo-data with a $\mathcal{CP}$-odd coupling parameter value of $s_\alpha \kappa_{Agg} = 0.43$ as a function of $s_\alpha \kappa_{Agg}$ for 120 fb^{-1}, 300 fb^{-1} and 3000 fb^{-1} corresponding to the expected luminosities at the ends of LHC Run 2 (solid blue), Run 3 (dotted green) and the HL-LHC project (dashed yellow), respectively, at a centre-of-mass energy of $\sqrt{s} = 13$ TeV.

in the studied BSM scenario can be excluded at the level of about 4σ. Additional sensitivity is expected from the increased centre-of-mass energy going from 13 TeV in Run 2 to 14 TeV in Run 3 and at the HL-LHC. The improvement to be expected for Run 3 and the HL-LHC is estimated by a scaling of the cross-sections [73] and is shown in Figures 5.15 and 5.16, respectively. For the ggF cross-section scaling it is assumed, that the scale factor is unaffected by BSM $\mathcal{CP}$-odd coupling contributions studied in this thesis.
The corresponding expected confidence intervals at 68 % CL and 95 % CL are summarised in Table 5.5.

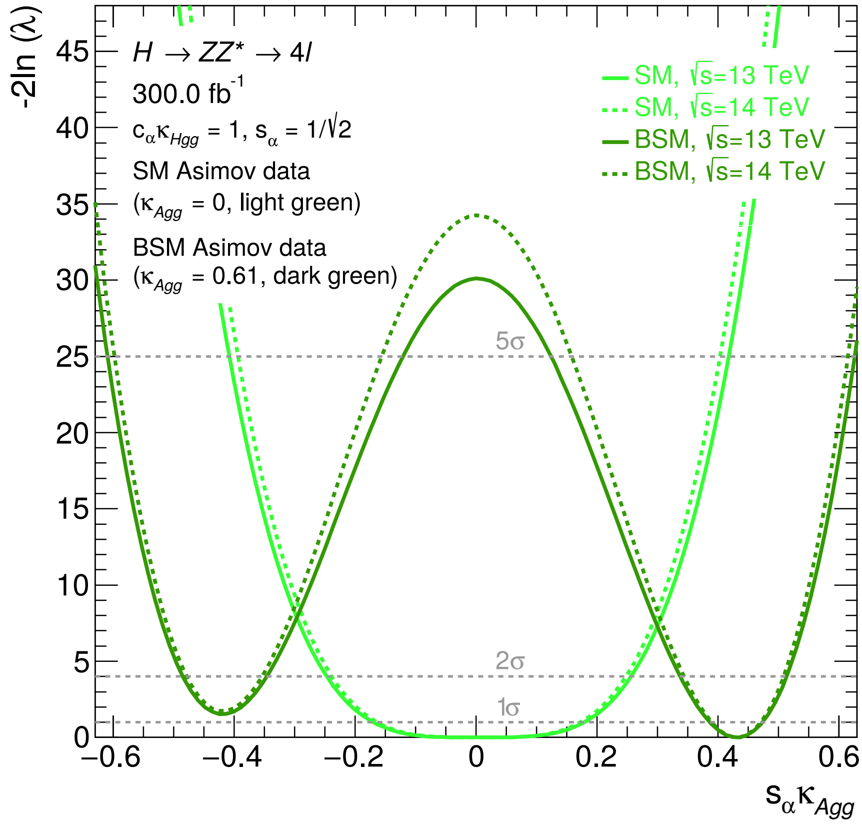

Figure 5.15: Expected test statistics for SM (light green) and BSM pseudo-data with a $\mathcal{CP}$-odd coupling parameter value of $s_\alpha\kappa_{Agg} = 0.43$ (dark green) as a function of $s_\alpha\kappa_{Agg}$ at LHC Run 2 and Run 3 centre-of-mass energies of $\sqrt{s} = 13$ TeV (solid line) and $\sqrt{s} = 14$ TeV (dotted line), respectively, for an integrated luminosity of 300 fb^{-1}, corresponding to the expected value at the end of LHC Run 3.

The luminosity thresholds corresponding to the exclusion of the wrong-sign values at the level of 2σ, 3σ, 4σ and 5σ are listed in Table 5.6.

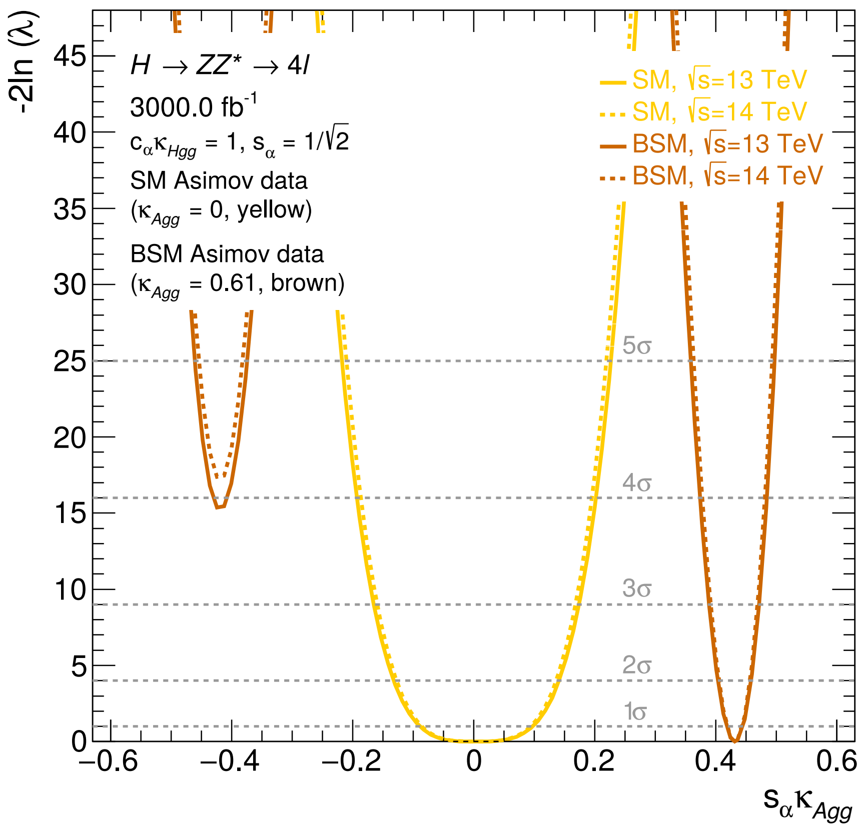

Figure 5.16: Expected test statistic for SM (orange) and BSM pseudo-data with a $\mathcal{CP}$-odd coupling parameter value of $s_\alpha \kappa_{Agg} = 0.43$ (brown) as a function of $s_\alpha \kappa_{Agg}$ at LHC Run 2 and Run 3 centre-of-mass energies of $\sqrt{s} = 13$ TeV (solid line) and $\sqrt{s} = 14$ TeV (dotted line), respectively, for an integrated luminosity of 3000 fb^{-1}, corresponding to the expected value at the end of the HL-LHC project.

Table 5.5: Exclusion limits for the $\mathcal{CP}$-odd coupling parameter $s_\alpha \kappa_{Agg}$ at 68 % CL and 95 % CL for integrated luminosities of 36.1 fb^{-1} and 120 fb^{-1} at a centre-of-mass energy of $\sqrt{s} = 13$ TeV and of 300 fb^{-1} and 3000 fb^{-1} at a centre-of-mass energy of $\sqrt{s} = 14$ TeV, assuming the SM or the BSM ($s_\alpha \kappa_{Agg} = 0.43$) hypothesis.

L [fb^{-1}]	$\sqrt{s}$ [TeV]	SM Asimov data 68 % CL	SM Asimov data 95 % CL
36.1	13	$[-0.30, 0.31]$	$[-0.44, 0.45]$
120	13	$[-0.22, 0.23]$	$[-0.31, 0.32]$
300	14	$[-0.16, 0.17]$	$[-0.24, 0.25]$
3000	14	$[-0.09, 0.09]$	$[-0.13, 0.13]$

L [fb^{-1}]	$\sqrt{s}$ [TeV]	BSM Asimov data ($s_\alpha \kappa_{Agg} = 0.43$) 68 % CL	BSM Asimov data ($s_\alpha \kappa_{Agg} = 0.43$) 95 % CL
36.1	13	$[-0.52, -0.29] \cup [0.29, 0.55]$	$[-0.63, 0.65]$
120	13	$[-0.46, -0.38] \cup [0.36, 0.50]$	$[-0.53, -0.28] \cup [0.28, 0.56]$
300	14	$[0.39, 0.47]$	$[-0.48, -0.36] \cup [0.35, 0.51]$
3000	14	$[0.42, 0.44]$	$[0.41, 0.46]$

Table 5.6: The integrated luminosity needed to reach the 2σ, 3σ, 4σ and 5σ exclusion of the wrong-sign $s_\alpha \kappa_{Agg}$ value for the BSM ($s_\alpha \kappa_{Agg} = 0.43$) scenario at a centre-of-mass energy $\sqrt{s} = 14$ TeV.

Standard deviation	2σ	3σ	4σ	5σ
Luminosity [fb^{-1}]	≈ 700	≈ 1550	≈ 2770	≈ 4300

6
Summary

Thousands of scientists each day gain further insight to how nature works and what the universe is made of. The ATLAS detector, one of the most complex machines ever built plays a prominent role therein, as it makes measurements at exceptional precisions possible, enabling the discovery of new particles or the verification of predicted properties of known particles. Even though with the observation of all major Higgs boson production and decay modes, the Standard Model (SM) today is more complete than ever, many unexplained phenomena still puzzle physicists and motivate the search for physics beyond the Standard Model (BSM).
Of utter importance for the evolution of the early universe is the $\mathcal{CP}$-violation. Searches for the $\mathcal{CP}$-violating sources are intensively studied, looking also at BSM scenarios with extensions of the SM Higgs boson sector. This thesis focusses on the possibility, that the Higgs boson is not a pure $\mathcal{CP}$-even state as predicted by the SM, but a mixed $\mathcal{CP}$ state with small $\mathcal{CP}$-odd contribution. Such anomalous contributions can be examined by measuring the tensor structure of the Higgs boson coupling to SM particles.
The gluon–gluon fusion is not only the most dominant Higgs boson production mode at the LHC, but also, since it is a loop-induced process, it provides good sensitivity to BSM physics, which is also expected to enter at the loop level. Using the Higgs characterisation model, the Hgg interaction vertex can be treated as a point-like interaction in an effective field theory approach.
Current measurements of the tensor coupling structure based on the measured production rates show no significant deviation from the SM prediction. Future analyses can be improved by including the information on the kinematic properties of a pair of jets, which can be produced in the gluon–gluon fusion process via higher-order corrections. The shape of the distribution of angular jet separation introduces the sensitivity to the sign of the $\mathcal{CP}$-odd contribution, other than the production rate alone.
The study is performed in the decay channel $H \rightarrow ZZ^{*} \rightarrow 4\ell$ characterised by a high signal-to-background ratio and a clear signature in the detector. Higgs boson candidate events are categorised according to the jet multiplicities, where the *2-jet* category is further split according to the relative orientation of the two leading jets. For the sensitivity study of

this thesis Monte Carlo samples have been generated for different values of the $\mathcal{CP}$-odd Hgg coupling parameter. Corrections have been applied to the simulated data in order to account for higher-order predictions of the cross-section, for selection and detector efficiencies and the proper modelling of the total decay width of the Higgs boson.
It was shown, that the difference in the azimuthal angle of the two leading jets in opposite hemispheres, that is, the observable $\Delta\phi_{jj}^{\text{sign}}$, is sensitive to the sign of the $\mathcal{CP}$-odd BSM coupling parameter $s_\alpha\kappa_{Agg}$. The sensitivity to the $\mathcal{CP}$-odd coupling contribution has been evaluated for different values of integrated luminosities in accordance to the expected values for the ends of LHC Run 2, Run 3 and the HL-LHC project. The results show that under a SM hypothesis the analysis of this thesis delivers exclusion limits, which are slightly worse than the ones from the published analysis based on the production rate information. This can be attributed to the more sophisticated categorisation scheme of the latter. Under a BSM hypothesis corresponding to a $\mathcal{CP}$-odd coupling parameter value equal to the best-fit value of current published measurements, a discrimination with regard to the sign of $s_\alpha\kappa_{Agg}$ is possible. The wrong-sign hypothesis can be excluded with almost 1σ significance, at slightly more than 1σ and at more than 4σ for an integrated luminosity of 120 fb^{-1} and a centre-of-mass energy of $\sqrt{s} = 13$ TeV and for 300 fb^{-1} and 3000 fb^{-1} at $\sqrt{s} = 14$ TeV, respectively.

A

Monte Carlo Simulation Samples

Table A.1

MC ID	Process	Generation and parton showering
345060	ggF	Powheg+Pythia8+EvtGen
344235	VBF	Powheg+Pythia8+EvtGen
345038	ZH	Powheg+Pythia8+EvtGen
345039	W^+H	Powheg+Pythia8+EvtGen
345040	W^-H	Powheg+Pythia8+EvtGen
343212	$ggZZ$	Powheg+gg2vv+Pythia8+EvtGen
343213		Powheg+gg2vv+Pythia8+EvtGen
345107	$qqZZ$	Sherpa
345108		Sherpa
363490		Sherpa

B

Validation plots of MC samples

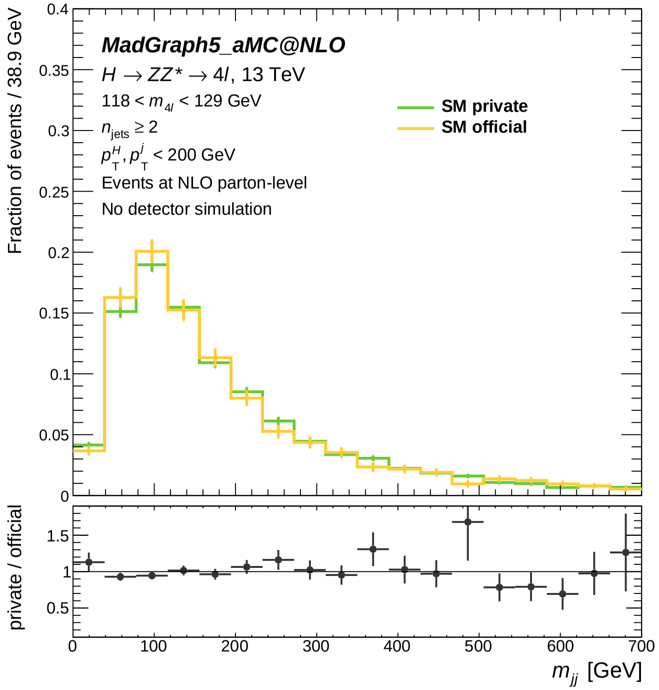

(a)

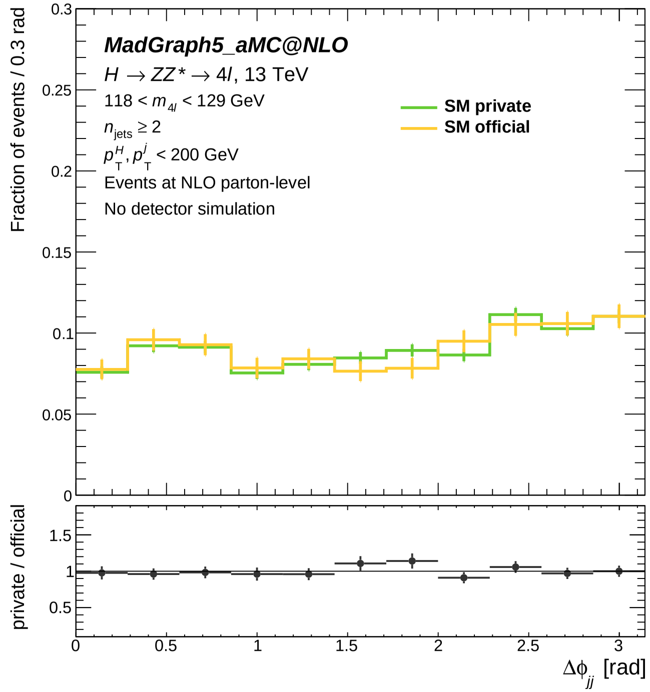

(b)

Figure B.1: Differential distributions of (a) the invariant mass m_{jj} of and (b) the difference in the azimuthal angle $\Delta\phi_{jj}$ between the two leading jets for the SM MC sample generated within this work and the corresponding official MC sample at particle-level.

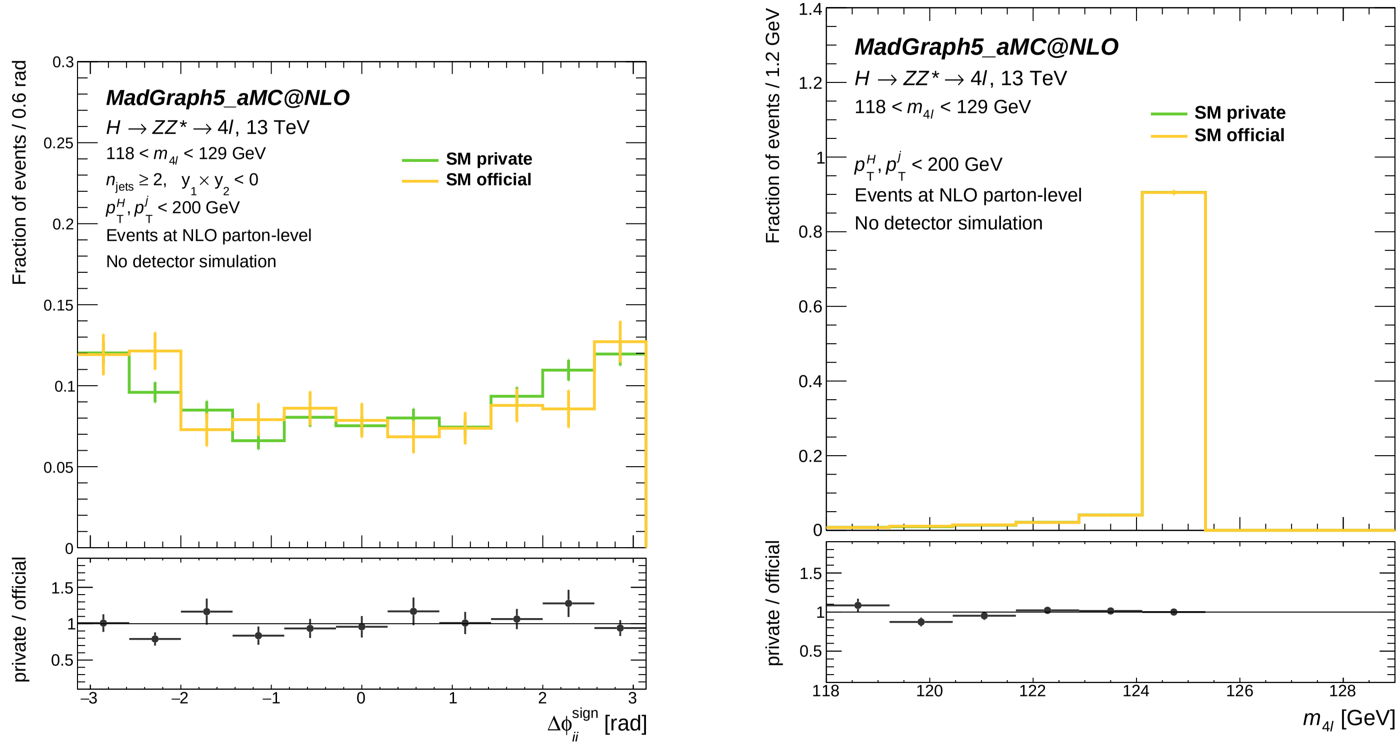

(a)

(b)

Figure B.2: Differential distributions of (a) the signed difference in the azimuthal angle between the two leading jets $\Delta\phi_{jj}^{\text{sign}}$ and (b) the four-lepton invariant mass $m_{4\ell}$ for the SM MC sample generated within this work and the corresponding official MC sample at particle-level.

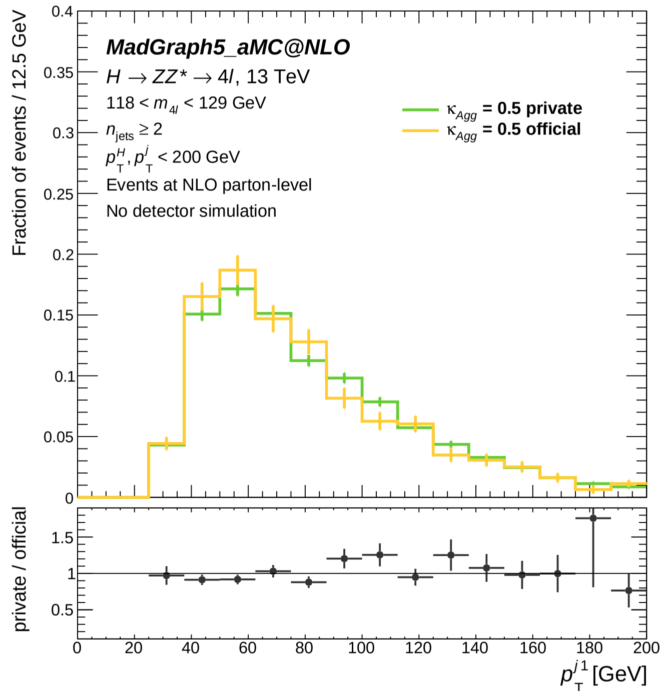

(a)

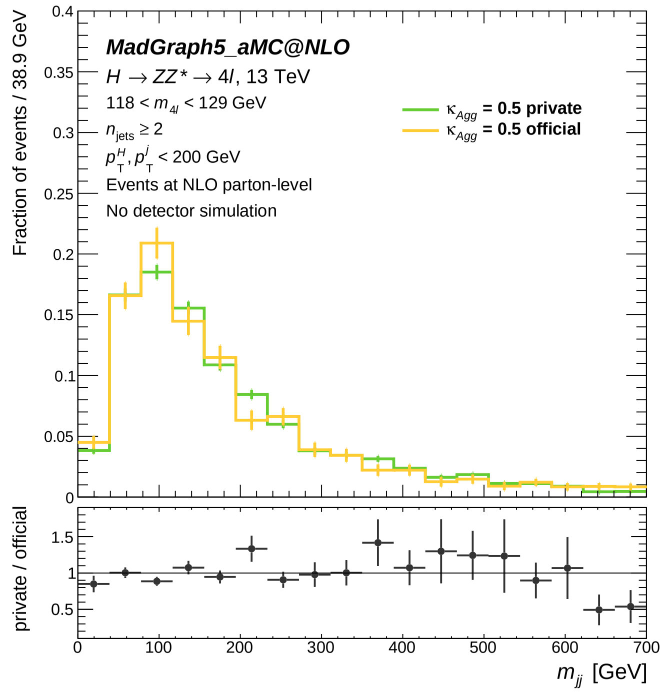

(b)

Figure B.3: Differential distributions of (a) the transverse momentum of the leading jet p_{T}^{j1} and (b) the invariant mass m_{jj} of the leading jets for the `BSMmix_kAgg_0p5` MC sample generated within this work and the corresponding official MC sample at particle-level.

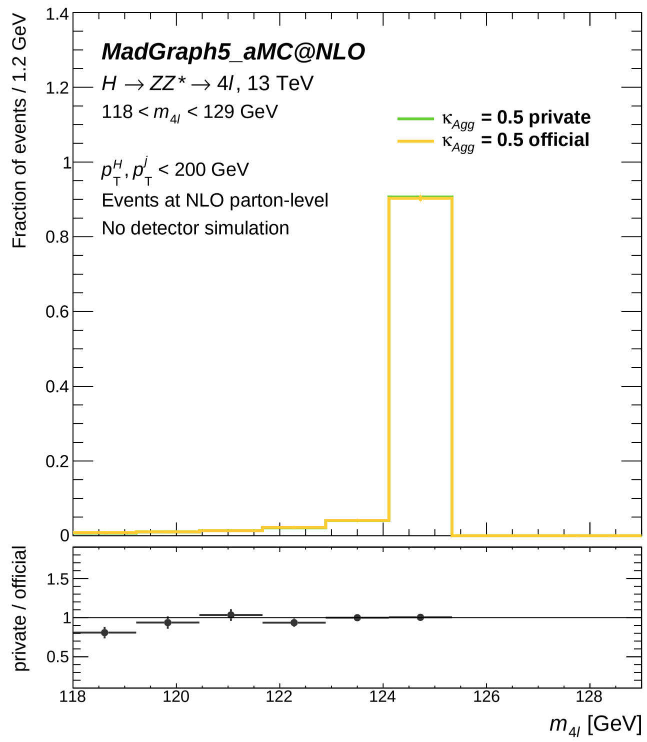

(a)

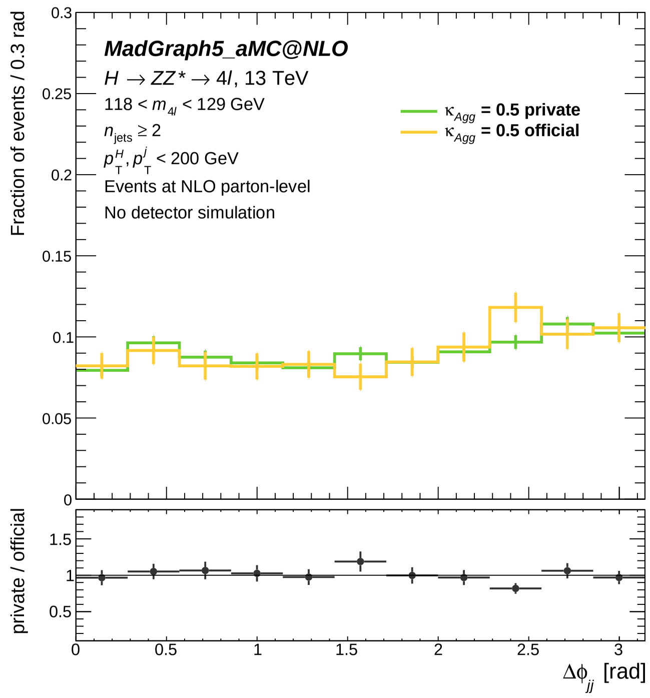

(b)

Figure B.4: Differential distributions of (a) the four-lepton invariant mass $m_{4\ell}$ and (b) the difference in the azimuthal angle $\Delta\phi_{jj}$ of the two leading jets for the `BSMmix_kAgg_0p5` MC sample generated within this work and the corresponding official MC sample at particle-level.

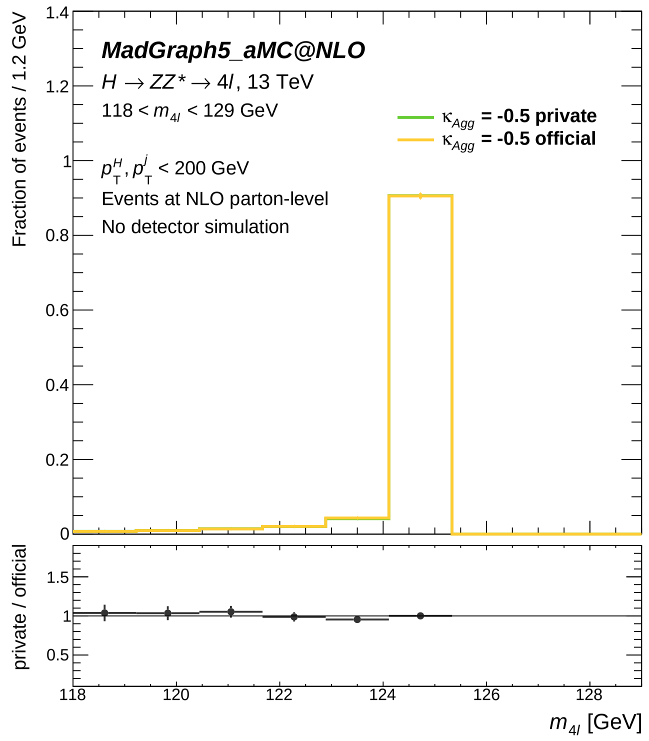

(a)

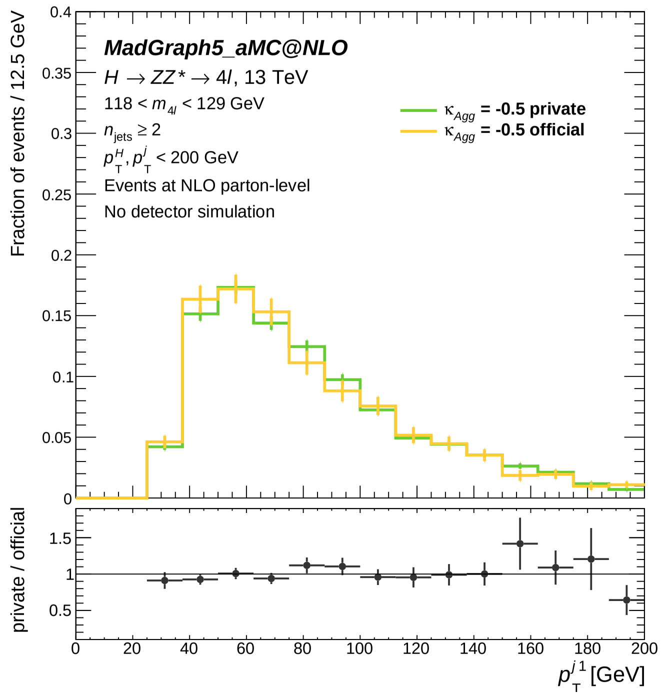

(b)

Figure B.5: Differential distributions of (a) the four-lepton invariant mass $m_{4\ell}$ and (b) the transverse momentum of the leading jet p_{T}^{j1} for the `BSMmix_kAgg_n0p5` MC sample generated within this work and the corresponding official MC sample at particle-level.

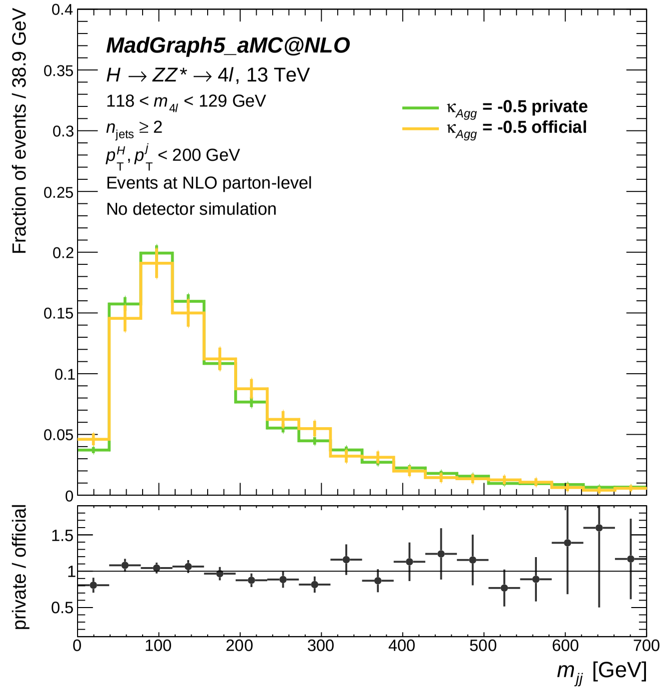

(a)

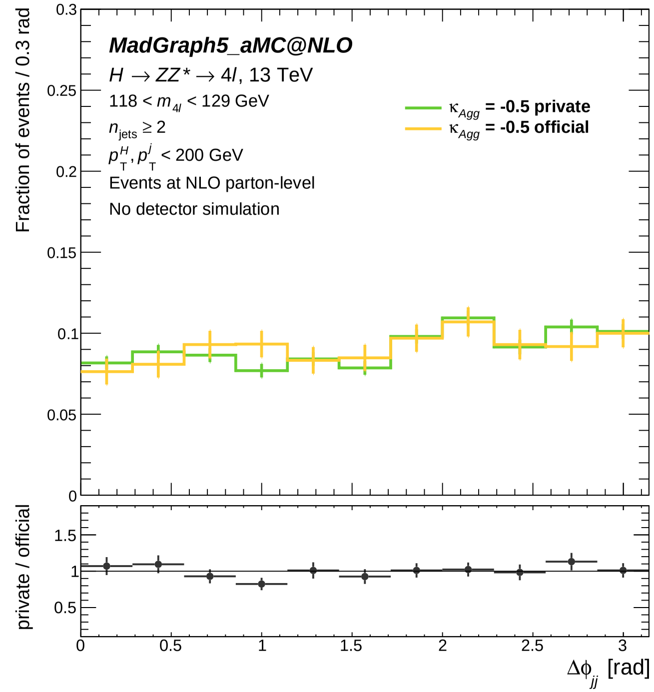

(b)

Figure B.6: Differential distributions of (a) the invariant mass m_{jj} and (b) the difference of the azimuthal angle of the two leading jets for the `BSMmix_kAgg_n0p5` MC sample generated within this work and the corresponding official MC sample at particle-level.

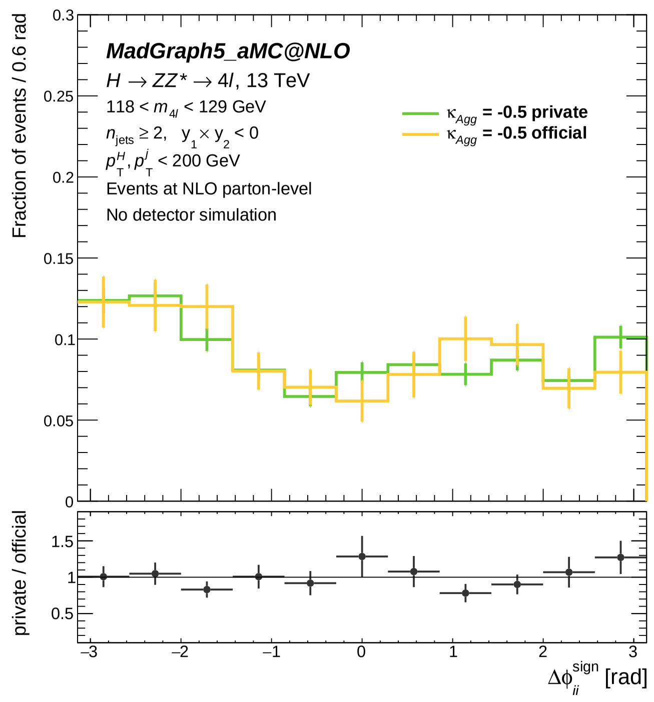

(a)

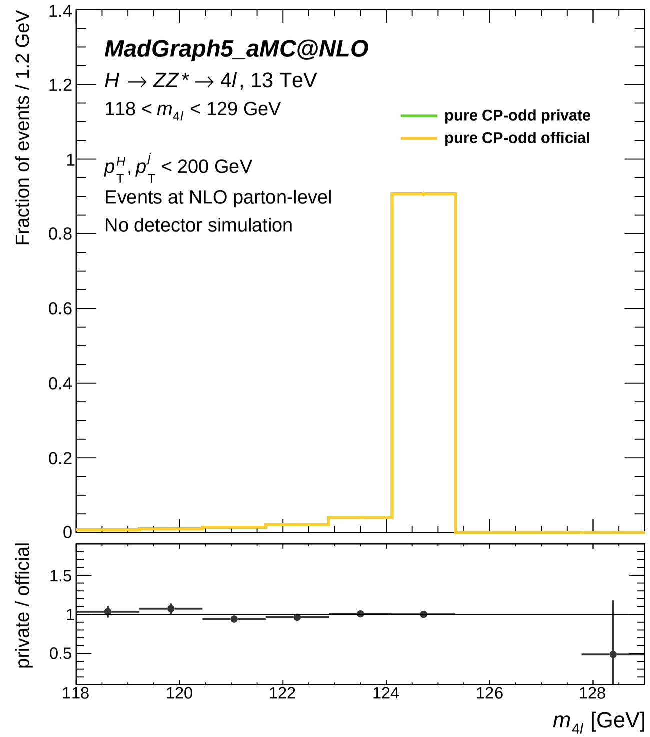

(b)

Figure B.7: Differential distributions of (a) the signed difference in the azimuthal angle between the two leading jets $\Delta\phi_{jj}^{\text{sign}}$ for the `BSMmix_kAgg_n0p5` MC sample and (b) the four-lepton invariant mass $m_{4\ell}$ for the `BSMpure` MC sample generated within this work and the corresponding official MC samples at particle-level.

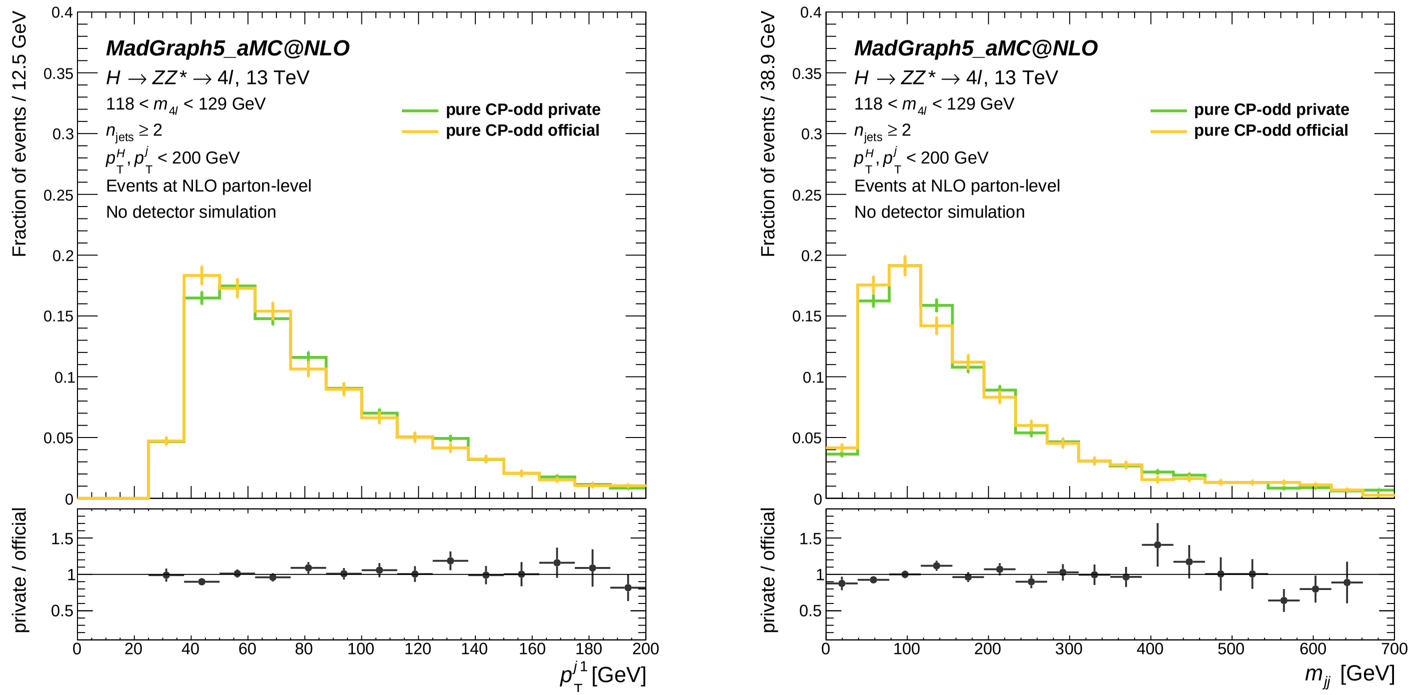

(a) (b)

Figure B.8: Differential distributions of (a) the transverse momentum of the leading jet p_T^{j1} and (b) the invariant mass m_{jj} of the leading jets for the `BSMpure` MC sample generated within this work and the corresponding official MC sample at particle-level.

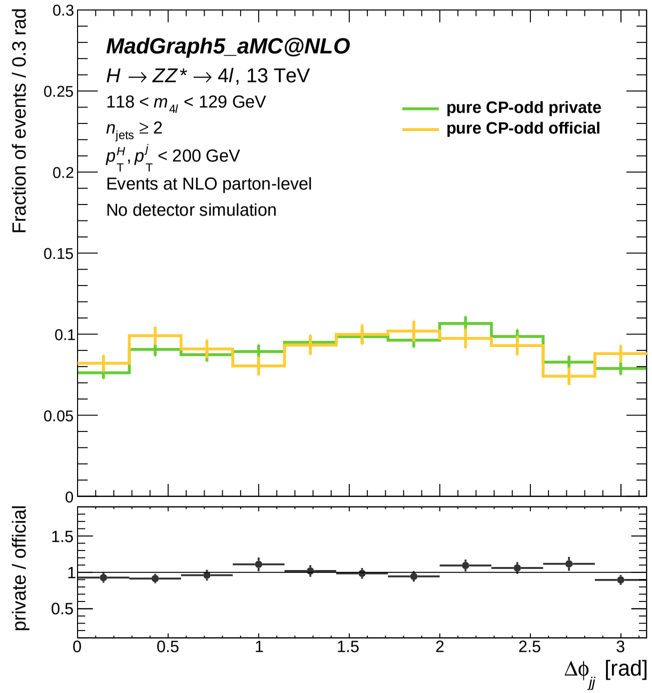

(a)

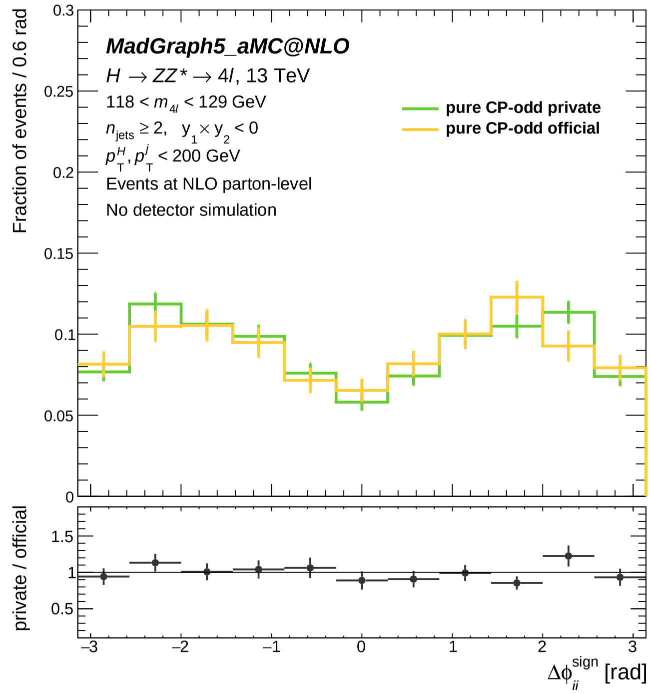

(b)

Figure B.9: Differential distributions of (a) the difference $\Delta\phi_{jj}$ and (b) the signed difference $\Delta\phi_{jj}^{\text{sign}}$ in the azimuthal angle for the `BSMpure` MC sample generated within this work and the corresponding official MC sample at particle-level.

Acknowledgements

An dieser Stelle möchte ich mich bei allen Menschen bedanken, die mich während des letzten Abschnitts meines Studiums unterstützt und begleitet haben.

In erster Linie danke ich Dr. Sandra Kortner für ihre wertvolle Betreuung. Danke für deine hilfreichen Anregungen und dafür, dass du immer Zeit für mich gefunden hast.
Auch möchte ich PD Dr. Oliver Kortner für die Möglichkeit bedanken, mich in meiner Forschungsphase mit den spannenden Eigenschaften des Higgs-Bosons beschäftigen zu können. Danke für das Stellen des Arbeitsthemas und die unkomplizierte Betreuung.
Ein großes Dankeschön geht an Verena Walbrecht und Dr. Katharina Ecker für die tägliche Zusammenarbeit und die wertvolle Hilfe. Danke für die unzähligen erleuchtenden Erklärungen und dafür, dass ihr jederzeit für Fragen und Anregungen zur Verfügung standet. Die kurzweiligen Kaffeepausen, das Eisessen und die Unterhaltungen haben jeden Tag bereichert.
Herzlichst möchte ich auch der ganzen MDT-Arbeitsgruppe danken. Ihr habt dazu beigetragen, dass ich vieles dazugelernt habe und eine angenehme und kollegiale Atmosphäre erfahren habe.

Danke an meine Eltern Ludmilla und Dimitri für eure unbezahlbare Unterstützung und Liebe. Auch meiner Schwerster Galina möchte ich für alles und dafür, dass du immer für mich da bist, danken.
Abschließend richtet sich mein Dank an Melanie; danke für deine verständnisvolle Geduld, deine Hilfe und Zuversicht!

Bibliography

[1] S. L. Glashow, *Partial Symmetries of Weak Interactions*, Nucl. Phys. **22** (1961) 579.

[2] Steven Weinberg, *A Model of Leptons*, Phys. Rev. Lett. **19** (1967) 1264.

[3] Abdus Salam, *Weak and Electromagnetic Interactions*, Conf. Proc. **C680519** (1968) 367.

[4] Gerard 't Hooft and M. J. G. Veltman, *Regularization and Renormalization of Gauge Fields*, Nucl. Phys. **B44** (1972) 189.

[5] ATLAS Collaboration, *Observation of a new particle in the search for the Standard Model Higgs boson with the ATLAS detector at the LHC*, Phys. Lett. B **716** (2012) 1, arXiv: `1207.7214 [hep-ex]`.

[6] CMS Collaboration, *Observation of a new boson at a mass of 125 GeV with the CMS experiment at the LHC*, Phys. Lett. B **716** (2012) 30, arXiv: `1207.7235 [hep-ex]`.

[7] Lyndon Evans and Philip Bryant, *LHC Machine*, Journal of Instrumentation **3** (2008) S08001, URL: `http://stacks.iop.org/1748-0221/3/i=08/a=S08001`.

[8] F. Englert and R. Brout, *Broken symmetry and the mass of gauge vector mesons*, Phys. Rev. Lett. **13** (1964) 321.

[9] Peter W. Higgs, *Broken symmetries, massless particles and gauge fields*, Phys. Lett. **12** (1964) 132.

[10] Peter W. Higgs, *Broken symmetries and the masses of gauge bosons*, Phys. Rev. Lett. **13** (1964) 508.

[11] G.S. Guralnik, C.R. Hagen and T.W.B. Kibble, *Global conservation laws and massless particles*, Phys. Rev. Lett. **13** (1964) 585.

[12] Peter W. Higgs, *Spontaneous symmetry breakdown without massless bosons*, Phys. Rev. **145** (1966) 1156.

[13] T.W.B. Kibble, *Symmetry breaking in non-Abelian gauge theories*, Phys. Rev. **155** (1967) 1554.

[14] ATLAS Collaboration, *Evidence for the spin-0 nature of the Higgs boson using ATLAS data*, Phys. Lett. B **726** (2013) 120, arXiv: `1307.1432 [hep-ex]`.

[15] CMS Collaboration, *Constraints on the spin-parity and anomalous HVV couplings of the Higgs boson in proton collisions at* 7 *and* 8 *TeV*, Phys. Rev. D **92** (2015) 012004, arXiv: 1411.3441 [hep-ex].

[16] LHC Higgs Cross Section Working Group, S. Heinemeyer, C. Mariotti, G. Passarino and R. Tanaka (Eds.), *Handbook of LHC Higgs Cross Sections: 3. Higgs Properties*, CERN-2013-004 (2013), arXiv: 1307.1347 [hep-ph].

[17] P. Artoisenet, P. de Aquino, F. Demartin, R. Frederix, S. Frixione et al., *A framework for Higgs characterisation*, JHEP **1311** (2013) 043, arXiv: 1306.6464 [hep-ph].

[18] ATLAS Collaboration, *Measurement of the Higgs boson coupling properties in the* $H \to ZZ^* \to 4\ell$ *decay channel at* $\sqrt{s} = 13$ *TeV with the ATLAS detector*, ATLAS-CONF-2017-043, 2017, URL: https://cds.cern.ch/record/2273849.

[19] Rende Steerenberg for the Operations group, *LHC report: full house for the LHC*, ed. by Stefania Pandolfi, 2017, URL: https://cds.cern.ch/record/2272573.

[20] Corinne Pralavorio, *Record luminosity: well done LHC*, 2017, URL: https://cds.cern.ch/record/2295027.

[21] *The accelerator complex*, (2012), URL: https://cds.cern.ch/record/1997193.

[22] Julie Haffner, *The CERN accelerator complex. Complexe des accélérateurs du CERN*, (2013), General Photo, URL: http://cds.cern.ch/record/1621894.

[23] Michael Hostettler and Giulia Papotti, 'Luminosity Lifetime at the LHC in 2012 Proton Physics Operation', *Proceedings, 4th International Particle Accelerator Conference (IPAC 2013): Shanghai, China, May 12-17, 2013*, 2013 TUPFI029, URL: http://JACoW.org/IPAC2013/papers/tupfi029.pdf.

[24] ATLAS Collaboration, *Luminosity public results run 1*, URL: https://twiki.cern.ch/twiki/bin/view/AtlasPublic/LuminosityPublicResults.

[25] Rende Steerenberg for the Operations group, *LHC Report: The LHC is full!*, ed. by Anais Schaeffer, 2018, URL: https://home.cern/cern-people/updates/2018/05/lhc-report-lhc-full (visited on 17/05/2018).

[26] ATLAS Collaboration, *Luminosity public results run 2*, URL: https://twiki.cern.ch/twiki/bin/view/AtlasPublic/LuminosityPublicResultsRun2.

[27] ATLAS Collaboration, *The ATLAS Experiment at the CERN Large Hadron Collider*, JINST **3** (2008) S08003.

[28] Joao Pequenao, 'Computer generated image of the whole ATLAS detector', 2008, URL: http://cds.cern.ch/record/1095924.

[29] C.Y. Wong, *Introduction to High-energy Heavy-ion Collisions*, World Scientific, 1994, ISBN: 9789810202637.

[30] ATLAS Collaboration,
Operation and performance of the ATLAS semiconductor tracker,
JINST **9** (2014) P08009, arXiv: 1404.7473 [hep-ex].

[31] M Capeans et al., *ATLAS Insertable B-Layer Technical Design Report*,
tech. rep. CERN-LHCC-2010-013. ATLAS-TDR-19, 2010,
URL: http://cds.cern.ch/record/1291633.

[32] Audrey Ducourthial et al., *Thin and edgeless sensors for ATLAS pixel detector upgrade. Thin and edgeless sensors for ATLAS pixel detector upgrade*,
JINST **12** (2017) C12038. 10 p, 10 pages, 7 figures, to appear in the proceedings of the PSD11 conference, 3th-8th September 2017, Open University (Milton Keynes),
URL: http://cds.cern.ch/record/2300091.

[33] E. Diehl, 'Calibration and Performance of the ATLAS Muon Spectrometer',
Particles and fields. Proceedings, Meeting of the Division of the American Physical Society, DPF 2011, Providence, USA, August 9-13, 2011, 2011,
arXiv: 1109.6933 [physics.ins-det], URL:
http://inspirehep.net/record/930228/files/arXiv:1109.6933.pdf.

[34] ATLAS Collaboration, *Muon reconstruction performance of the ATLAS detector in proton–proton collision data at $\sqrt{s}$ = 13 TeV*, Eur. Phys. J. C **76** (2016) 292,
arXiv: 1603.05598 [hep-ex].

[35] ATLAS Collaboration, *Performance of the ATLAS Trigger System in 2015*,
Eur. Phys. J. C **77** (2017) 317, arXiv: 1611.09661 [hep-ex].

[36] Joao Pequenao and Paul Schaffner,
'An computer generated image representing how ATLAS detects particles', 2013,
URL: https://cds.cern.ch/record/1505342.

[37] ATLAS Collaboration, *Performance of the ATLAS Inner Detector Track and Vertex Reconstruction in High Pile-Up LHC Environment*, ATLAS-CONF-2012-042, 2012,
URL: https://cds.cern.ch/record/1435196.

[38] ATLAS Collaboration, *Performance of the ATLAS track reconstruction algorithms in dense environments in LHC Run 2*, Eur. Phys. J. C **77** (2017) 673,
arXiv: 1704.07983 [hep-ex].

[39] ATLAS Collaboration, *Performance of primary vertex reconstruction in proton–proton collisions at $\sqrt{s}$ = 7 TeV in the ATLAS experiment*,
ATLAS-CONF-2010-069, 2010, URL: https://cds.cern.ch/record/1281344.

[40] ATLAS Collaboration, *Electron efficiency measurements with the ATLAS detector using the 2015 LHC proton–proton collision data*, ATLAS-CONF-2016-024, 2016,
URL: https://cds.cern.ch/record/2157687.

[41] ATLAS Collaboration, *Measurement of the muon reconstruction performance of the ATLAS detector using 2011 and 2012 LHC proton–proton collision data*, Eur. Phys. J. C **74** (2014) 3130, arXiv: 1407.3935 [hep-ex].

[42] ATLAS Collaboration, *Performance of the ATLAS Silicon Pattern Recognition Algorithm in Data and Simulation at $\sqrt{s} = 7$ TeV*, ATLAS-CONF-2010-072, 2010, URL: https://cds.cern.ch/record/1281363.

[43] ATLAS Collaboration, *Muon reconstruction performance in early $\sqrt{s} = 13$ TeV data*, ATL-PHYS-PUB-2015-037, 2015, URL: https://cds.cern.ch/record/2047831.

[44] ATLAS Collaboration, *Determination of the jet energy scale and resolution at ATLAS using Z/γ-jet events in data at $\sqrt{s} = 8$ TeV*, ATLAS-CONF-2015-057, 2015, URL: https://cds.cern.ch/record/2059846.

[45] Matteo Cacciari, Gavin P. Salam and Gregory Soyez, *The Anti-k(t) jet clustering algorithm*, JHEP **04** (2008) 063, arXiv: 0802.1189 [hep-ph].

[46] ATLAS Collaboration, *Jet energy resolution in proton–proton collisions at $\sqrt{s} = 7$ TeV recorded in 2010 with the ATLAS detector*, Eur. Phys. J. C **73** (2013) 2306, arXiv: 1210.6210 [hep-ex].

[47] ATLAS Collaboration, *Selection of jets produced in* 13 *TeV proton–proton collisions with the ATLAS detector*, ATLAS-CONF-2015-029, 2015, URL: https://cds.cern.ch/record/2037702.

[48] Francis Halzen and Alan D. Martin, *QUARKS AND LEPTONS: An Introductory Course in Modern Particle Physics*, JOHN WILEY & SONS, 1984, ISBN: 0-471-88741-2.

[49] Wolfgang Hollik, *Quantum field theory and the Standard Model*, (2010), arXiv: 1012.3883v1 [hep-ph].

[50] Cush, *Standard Model of Elementary Particles*, 2017, URL: https://commons.wikimedia.org/wiki/File:Standard_Model_of_Elementary_Particles_dark.svg (visited on 29/05/2018).

[51] David Griffiths, *Introduction to Elementary Particles*, Second, Revised Edition, WILEY-VCH Verlag GmbH & Co. KGaA, 2014, ISBN: 978-3-527-40601-2.

[52] M. Tanabashi *et al.* (Particle Data Group), *2018 Review of Particle Physics*, Phys. Rev. **D98** (2018) 030001.

[53] Heather E. Logan, *TASI 2013 lectures on Higgs physics within and beyond the Standard Model*, (2014), arXiv: 1406.1786 [hep-ph].

[54] Peter W. Higgs, *Broken Symmetries and the Masses of Gauge Bosons*, Phys. Rev. Lett. **13** (16 1964) 508, URL: https://link.aps.org/doi/10.1103/PhysRevLett.13.508.

[55] F. Englert and R. Brout, *Broken Symmetry and the Mass of Gauge Vector Mesons*, Phys. Rev. Lett. **13** (9 1964) 321, URL: https://link.aps.org/doi/10.1103/PhysRevLett.13.321.

[56] G. S. Guralnik, C. R. Hagen and T. W. B. Kibble, *Global Conservation Laws and Massless Particles*, Phys. Rev. Lett. **13** (20 1964) 585, URL: https://link.aps.org/doi/10.1103/PhysRevLett.13.585.

[57] Peter W. Higgs, *Spontaneous Symmetry Breakdown without Massless Bosons*, Phys. Rev. **145** (4 1966) 1156, URL: https://link.aps.org/doi/10.1103/PhysRev.145.1156.

[58] Wim de Boer, 'The Discovery of the Higgs Boson with the CMS Detector and its Implications for Supersymmetry and Cosmology', *Time and Matter 2013 (TAM2013) Venice, Italy*, 2013, arXiv: 1309.0721 [hep-ph], URL: http://inspirehep.net/record/1252561/files/arXiv:1309.0721.pdf.

[59] Vernon Barger, Tao Han, Paul Langacker, Bob McElrath and Peter Zerwas, *Effects of genuine dimension-six Higgs operators*, Phys. Rev. D **67** (11 2003) 115001, URL: https://link.aps.org/doi/10.1103/PhysRevD.67.115001.

[60] M. Tanabashi *et al.* (Particle Data Group), *pdgLive - 2018 Review of Particle Physics*, URL: pdglive.lbl.gov/Viewer.action (visited on 11/06/2018).

[61] Super-Kamiokande Collaboration, *Evidence for Oscillation of Atmospheric Neutrinos*, Phys. Rev. Lett. **81** (8 1998) 1562, URL: https://link.aps.org/doi/10.1103/PhysRevLett.81.1562.

[62] SNO Collaboration, *Measurement of the Rate of $\nu_e + d \to p + p + e^-$ Interactions Produced by ^8B Solar Neutrinos at the Sudbury Neutrino Observatory*, Phys. Rev. Lett. **87** (7 2001) 071301, URL: https://link.aps.org/doi/10.1103/PhysRevLett.87.071301.

[63] SNO Collaboration, *Direct Evidence for Neutrino Flavor Transformation from Neutral-Current Interactions in the Sudbury Neutrino Observatory*, Phys. Rev. Lett. **89** (1 2002) 011301, URL: https://link.aps.org/doi/10.1103/PhysRevLett.89.011301.

[64] Amber Harmon, *Sherpa and Open Science Grid: Predicting the emergence of jets*, 2014, URL: https://sciencenode.org/feature/sherpa-and-open-science-grid-predicting-emergence-jets.php (visited on 12/06/2018).

[65] John M. Campbell, J. W. Huston and W. J. Stirling, *Hard Interactions of Quarks and Gluons: A Primer for LHC Physics*, Rept. Prog. Phys. **70** (2007) 89, arXiv: hep-ph/0611148 [hep-ph].

[66] Xin-nian Wang and Rudolph C. Hwa, *Effect of jet production on the multiplicity dependence of average transverse momentum*, Phys. Rev. D **39** (1 1989) 187, URL: https://link.aps.org/doi/10.1103/PhysRevD.39.187.

[67] D. Acosta et al., *Soft and hard interactions in $p\overline{p}$ collisions at $\sqrt{s}$ = 1800 and 630 GeV*, Phys. Rev. D **65** (7 2002) 072005, URL: https://link.aps.org/doi/10.1103/PhysRevD.65.072005.

[68] F Maltoni, *Basics of QCD for the LHC: $pp \to H + X$ as a case study. Basics of QCD for the LHC: Higgs production as a case study*, (2014), URL: https://cds.cern.ch/record/2008764.

[69] Yuri L. Dokshitzer, *Calculation of the Structure Functions for Deep Inelastic Scattering and e+ e- Annihilation by Perturbation Theory in Quantum Chromodynamics.*, Sov. Phys. JETP **46** (1977) 641, [Zh. Eksp. Teor. Fiz.73,1216(1977)].

[70] V. N. Gribov and L. N. Lipatov, *Deep inelastic e p scattering in perturbation theory*, Sov. J. Nucl. Phys. **15** (1972) 438, [Yad. Fiz.15,781(1972)].

[71] G. Altarelli and G. Parisi, *Asymptotic freedom in parton language*, Nuclear Physics B **126** (1977) 298, ISSN: 0550-3213, URL: http://www.sciencedirect.com/science/article/pii/0550321377903844.

[72] Joshua Ellis, *TikZ-Feynman: Feynman diagrams with TikZ*, Comput. Phys. Commun. **210** (2017) 103, arXiv: 1601.05437 [hep-ph].

[73] LHC Higgs Cross Section Working Group, *Higgs cross sections and decay branching ratios*, URL: https://twiki.cern.ch/twiki/bin/view/LHCPhysics/LHCHXSWG (visited on 13/06/2018).

[74] Jon Butterworth et al., *PDF4LHC recommendations for LHC Run II*, J. Phys. **G43** (2016) 023001, arXiv: 1510.03865 [hep-ph].

[75] Tilman Plehn, *Lectures on LHC Physics*, 2nd ed., Springer International Publishing, 2015, ISBN: 978-3-319-05941-9.

[76] LHC Higgs Cross Section Working Group et al., *Handbook of LHC Higgs Cross Sections: 4. Deciphering the nature of the Higgs sector*, (CERN, Geneva, 2016), arXiv: 1610.07922 [hep-ph].

[77] D. de Florian et al.,
Handbook of LHC Higgs Cross Sections: 4. Deciphering the Nature of the Higgs Sector,
tech. rep. FERMILAB-FN-1025-T,
869 pages, 295 figures, 248 tables and 1645 citations. Working Group web page:
https://twiki.cern.ch/twiki/bin/view/LHCPhysics/LHCHXSWG, 2016,
URL: `https://cds.cern.ch/record/2227475`.

[78] G. Dvali, *A Lecture on the Hierarchy Problem and Gravity*, (2013),
URL: `https://cds.cern.ch/record/2120792`.

[79] C.H.Llewellyn Smith and G.G. Ross, *The real gauge hierarchy problem*,
Physics Letters B **105** (1981) 38, ISSN: 0370-2693, URL: `http://www.sciencedirect.com/science/article/pii/0370269381900356`.

[80] Steven Weinberg, *Gauge hierarchies*, Physics Letters B **82** (1979) 387, ISSN: 0370-2693,
URL: `http://www.sciencedirect.com/science/article/pii/037026937990248X`.

[81] A. Bosma, *21-cm line studies of spiral galaxies. II. The distribution and kinematics of neutral hydrogen in spiral galaxies of various morphological types.*,
Astron.J. **86** (1981) 1825.

[82] V. C. Rubin, D. Burstein, W. K. Ford Jr. and N. Thonnard, *Rotation velocities of 16 SA galaxies and a comparison of Sa, Sb, and SC rotation properties*,
Astrophys.J. **289** (1985) 81.

[83] Stephen P. Martin, 'A Supersymmetry Primer', *Perspectives on Supersymmetry II*,
WORLD SCIENTIFIC, 2011 1, eprint: `https://www.worldscientific.com/doi/pdf/10.1142/9789814307505_0001`,
URL: `https://www.worldscientific.com/doi/abs/10.1142/9789814307505_0001`.

[84] Yuri A. Golfand and E. P. Likhtman,
Extension of the Algebra of Poincare Group Generators and Violation of p Invariance,
JETP Lett. **13** (1971) 323, [Pisma Zh. Eksp. Teor. Fiz.13,452(1971)].

[85] D. V. Volkov and V. P. Akulov, *Is the Neutrino a Goldstone Particle?*,
Phys. Lett. B **46** (1973) 109.

[86] J. Wess and B. Zumino, *Supergauge Transformations in Four-Dimensions*,
Nucl. Phys. B **70** (1974) 39.

[87] J. Wess and B. Zumino, *Supergauge Invariant Extension of Quantum Electrodynamics*,
Nucl. Phys. B **78** (1974) 1.

[88] Abdus Salam and J. A. Strathdee, *Supersymmetry and Nonabelian Gauges*,
Phys. Lett. B **51** (1974) 353.

[89] Pierre Fayet, *Supersymmetry and weak, electromagnetic and strong interactions*, Phys. Lett. B **64** (1976) 159.

[90] Pierre Fayet, *Spontaneously broken supersymmetric theories of weak, electromagnetic and strong interactions*, Phys. Lett. B **69** (1977) 489.

[91] Laurent Canetti, Marco Drewes and Mikhail Shaposhnikov, *Matter and Antimatter in the Universe*, New J. Phys. **14** (2012) 095012, arXiv: `1204.4186 [hep-ph]`.

[92] Andrei D. Sakharov, *Violation of CP invariance, C asymmetry, and baryon asymmetry of the universe*, Soviet Physics Uspekhi **34** (1991) 392, URL: `http://stacks.iop.org/0038-5670/34/i=5/a=A08`.

[93] ATLAS Collaboration, *Study of the spin and parity of the Higgs boson in diboson decays with the ATLAS detector*, Eur. Phys. J. C **75** (2015) 476, arXiv: `1506.05669 [hep-ex]`, Erratum: Eur. Phys. J. C **76** (2016) 152.

[94] Glen Cowan, Kyle Cranmer, Eilam Gross and Ofer Vitells, *Asymptotic formulae for likelihood-based tests of new physics*, Eur. Phys. J. **C71** (2011) 1554, [Erratum: Eur. Phys. J.C73,2501(2013)], arXiv: `1007.1727 [physics.data-an]`.

[95] Matthew J. Dolan, Philip Harris, Martin Jankowiak and Michael Spannowsky, *Constraining CP-violating Higgs Sectors at the LHC using gluon fusion*, Phys. Rev. **D90** (2014) 073008, arXiv: `1406.3322 [hep-ph]`.

[96] G Luisoni et al., *Higgs Boson production in association with jets in gluon-gluon fusion*, Journal of Physics: Conference Series **762** (2016) 012069, URL: `http://stacks.iop.org/1742-6596/762/i=1/a=012069`.

[97] V. Del Duca, W. Kilgore, C. Oleari, C. Schmidt and D. Zeppenfeld, *Higgs + 2 jets via gluon fusion*, Phys. Rev. Lett. **87** (2001) 122001, arXiv: `hep-ph/0105129 [hep-ph]`.

[98] Dirk Graudenz, 'The Physics of the standard model Higgs boson at the LHC', *'95 QCD and high-energy hadronic interactions. Proceedings, 30th Rencontres de Moriond, Moriond Particle Physics Meetings, Hadronic Session, Le Arcs, France, March 19-25, 1995*, 1995 65, arXiv: `hep-ph/9504223 [hep-ph]`, URL: `http://preprints.cern.ch/cgi-bin/setlink?base=preprint&categ=cern&id=th95-77`.

[99] Charalampos Anastasiou, Claude Duhr, Falko Dulat, Franz Herzog and Bernhard Mistlberger, *Higgs Boson Gluon-Fusion Production in QCD at Three Loops*, Phys. Rev. Lett. **114** (2015) 212001, arXiv: `1503.06056 [hep-ph]`.

[100] Charalampos Anastasiou et al., *High precision determination of the gluon fusion Higgs boson cross-section at the LHC*, JHEP **05** (2016) 058, arXiv: 1602.00695 [hep-ph].

[101] Nicolas Greiner, Stefan Höche, Gionata Luisoni, Marek Schönherr and Jan-Christopher Winter, *Full mass dependence in Higgs boson production in association with jets at the LHC and FCC*, JHEP **01** (2017) 091, arXiv: 1608.01195 [hep-ph].

[102] S. P. Jones, M. Kerner and G. Luisoni, *Next-to-Leading-Order QCD Corrections to Higgs Boson Plus Jet Production with Full Top-Quark Mass Dependence*, Phys. Rev. Lett. **120** (2018) 162001, arXiv: 1802.00349 [hep-ph].

[103] V. Del Duca, W. Kilgore, C. Oleari, C. Schmidt and D. Zeppenfeld, *Gluon fusion contributions to H + 2 jet production*, Nucl. Phys. **B616** (2001) 367, arXiv: hep-ph/0108030 [hep-ph].

[104] Luca Di Luzio, Ramona Gröber and Michael Spannowsky, *Maxi-sizing the trilinear Higgs self-coupling: how large could it be?*, The European Physical Journal C **77** (2017) 788, ISSN: 1434-6052, URL: https://doi.org/10.1140/epjc/s10052-017-5361-0.

[105] Timo van Ritbergen and Robin G. Stuart, *On the precise determination of the Fermi coupling constant from the muon lifetime*, Nuclear Physics B **564** (2000) 343, ISSN: 0550-3213, URL: http://www.sciencedirect.com/science/article/pii/S0550321399005726.

[106] ATLAS and CMS Collaborations, *Combined Measurement of the Higgs Boson Mass in pp Collisions at* $\sqrt{s} = 7$ *and* 8 *TeV with the ATLAS and CMS Experiments*, Phys. Rev. Lett. **114** (2015) 191803, arXiv: 1503.07589 [hep-ex].

[107] ATLAS Collaboration, *Measurement of the Higgs boson mass in the* $H \to ZZ^* \to 4\ell$ *and* $H \to \gamma\gamma$ *channels with* $\sqrt{s} = 13$ *TeV pp collisions using the ATLAS detector*, ATLAS-CONF-2017-046, 2017, URL: https://cds.cern.ch/record/2273853.

[108] CMS Collaboration, *Measurements of properties of the Higgs boson decaying into the four-lepton final state in pp collisions at* $\sqrt{s} = 13$ *TeV*, JHEP **11** (2017) 047, arXiv: 1706.09936 [hep-ex].

[109] ATLAS and CMS Collaborations, *Measurements of the Higgs boson production and decay rates and constraints on its couplings from a combined ATLAS and CMS analysis of the LHC pp collision data at* $\sqrt{s} = 7$ *and* 8 *TeV*, JHEP **08** (2016) 045, arXiv: 1606.02266 [hep-ex].

[110] CMS Collaboration, *Observation of the Higgs boson decay to a pair of* τ *leptons*, Phys. Lett. B **779** (2018) 283, arXiv: 1708.00373 [hep-ex].

[111] ATLAS Collaboration, *Observation of Higgs boson production in association with a top quark pair at the LHC with the ATLAS detector*, (2018), arXiv: 1806.00425 [hep-ex].

[112] CMS Collaboration, *Observation of* $t\bar{t}H$ *production*, Phys. Rev. Lett. **120** (2018) 231801, arXiv: 1804.02610 [hep-ex].

[113] *Observation of* $H \to b\bar{b}$ *decays and* VH *production with the ATLAS detector*, tech. rep. CERN-EP-2018-215, CERN, 2018, URL: https://cds.cern.ch/record/2636066.

[114] L. D. Landau, *On the angular momentum of a system of two photons*, Dokl. Akad. Nauk Ser. Fiz. **60** (1948) 207.

[115] C. N. Yang, *Selection Rules for the Dematerialization of a Particle into Two Photons*, Phys. Rev. **77** (2 1950) 242, URL: https://link.aps.org/doi/10.1103/PhysRev.77.242.

[116] Simone Alioli, Paolo Nason, Carlo Oleari and Emanuele Re, *NLO Higgs boson production via gluon fusion matched with shower in POWHEG*, JHEP **04** (2009) 002, arXiv: 0812.0578 [hep-ph].

[117] Paolo Nason and Carlo Oleari, *NLO Higgs boson production via vector-boson fusion matched with shower in POWHEG*, JHEP **02** (2010) 037, arXiv: 0911.5299 [hep-ph].

[118] Keith Hamilton, Paolo Nason, Emanuele Re and Giulia Zanderighi, *NNLOPS simulation of Higgs boson production*, JHEP **10** (2013) 222, arXiv: 1309.0017 [hep-ph].

[119] Torbjörn Sjöstrand et al., *An Introduction to PYTHIA 8.2*, Comput. Phys. Commun. **191** (2015) 159, arXiv: 1410.3012 [hep-ph].

[120] D. J. Lange, *The EvtGen particle decay simulation package*, Nucl. Instrum. Meth. **A462** (2001) 152.

[121] T. Gleisberg et al., *Event generation with SHERPA 1.1*, JHEP **02** (2009) 007, arXiv: 0811.4622 [hep-ph].

[122] Nikolas Kauer, Claire O'Brien and Eleni Vryonidou, *Interference effects for* $H \to W\ W \to \ell\nu q\bar{q}'$ *and* $H \to ZZ \to \ell\bar{\ell}q\bar{q}$ *searches in gluon fusion at the LHC*, JHEP **10** (2015) 074, arXiv: 1506.01694 [hep-ph].

[123] ATLAS Collaboration, *Measurements of the Higgs boson production cross section at* 7, 8 *and* 13 *TeV centre-of-mass energies and search for new physics at* 13 *TeV in the* $H \to ZZ^* \to \ell^+\ell^-\ell'^+\ell'^-$ *final state with the ATLAS detector*, ATLAS-CONF-2015-059, 2015, URL: https://cds.cern.ch/record/2114825.

[124] ATLAS Collaboration,
Study of the Higgs boson properties and search for high-mass scalar resonances in the $H \to ZZ^* \to 4\ell$ decay channel at $\sqrt{s} = 13$ TeV with the ATLAS detector,
ATLAS-CONF-2016-079, 2016, URL: https://cds.cern.ch/record/2206253.

[125] Katharina Maria Ecker, 'Measurement of the Higgs boson tensor coupling in $H \to ZZ^* \to 4\ell$ decays with the ATLAS detector - How odd is the Higgs boson?',
Ph.D. Thesis: TU München, 2018, URL: https://cds.cern.ch/record/2624277.

[126] ATLAS Collaboration, *The ATLAS Simulation Infrastructure*,
Eur. Phys. J. C **70** (2010) 823, arXiv: 1005.4568 [physics.ins-det].

[127] J. Alwall et al., *The automated computation of tree-level and next-to-leading order differential cross sections, and their matching to parton shower simulations*,
JHEP **07** (2014) 079, arXiv: 1405.0301 [hep-ph].

[128] Richard D. Ball et al., *Parton distributions with LHC data*,
Nucl. Phys. **B867** (2013) 244, arXiv: 1207.1303 [hep-ph].

[129] Pierre Artoisenet, Rikkert Frederix, Olivier Mattelaer and Robbert Rietkerk,
Automatic spin-entangled decays of heavy resonances in Monte Carlo simulations,
JHEP **03** (2013) 015, arXiv: 1212.3460 [hep-ph].

[130] Johan Alwall et al., *A Standard format for Les Houches event files*,
Comput. Phys. Commun. **176** (2007) 300, arXiv: hep-ph/0609017 [hep-ph].

[131] ATLAS Collaboration, *ATLAS Pythia 8 tunes to* 7 *TeV data*,
ATL-PHYS-PUB-2014-021, 2014, URL: https://cds.cern.ch/record/1966419.

[132] Rikkert Frederix and Stefano Frixione, *Merging meets matching in MC@NLO*,
JHEP **12** (2012) 061, arXiv: 1209.6215 [hep-ph].

[133] ATLAS Collaboration, *A morphing technique for signal modelling in a multidimensional space of coupling parameters*, ATL-PHYS-PUB-2015-047, 2015,
URL: https://cds.cern.ch/record/2066980.

[134] V. Hankele, G. Klamke and D. Zeppenfeld,
'Higgs + 2 jets as a probe for CP properties', *Meeting on CP Violation and Non-standard Higgs Physics Geneva, Switzerland, December 2-3, 2004*, 2006 58,
arXiv: hep-ph/0605117 [hep-ph].

[135] Vittorio Del Duca et al., *Monte Carlo studies of the jet activity in Higgs + 2 jet events*,
JHEP **10** (2006) 016, arXiv: hep-ph/0608158 [hep-ph].

[136] G. Klamke and D. Zeppenfeld,
Higgs plus two jet production via gluon fusion as a signal at the CERN LHC,
JHEP **04** (2007) 052, arXiv: hep-ph/0703202 [HEP-PH].

[137] Francisco Campanario, Michael Kubocz and Dieter Zeppenfeld, *Gluon-fusion contributions to Phi + 2 Jet production*, Phys. Rev. **D84** (2011) 095025, arXiv: 1011.3819 [hep-ph].

[138] Francisco Campanario and Michael Kubocz, *Higgs boson CP-properties of the gluonic contributions in Higgs plus three jet production via gluon fusion at the LHC*, JHEP **10** (2014) 173, arXiv: 1402.1154 [hep-ph].